154

NEUTRAL STRANGE PARTICLE PRODUCTION IN $\pi^- p$ INTERACTIONS AT 147 GeV/c

By TUNGCHING OU

E 154

A thesis submitted to
The Graduate School
of
Rutgers, The State University of New Jersey
in partial fulfillment of the requirements
for the degree of
Doctor of Philosophy
Graduate Program in Physics

Written under the direction of
Professor Terence L. Watts
and approved by

New Brunswick, New Jersey
May, 1979

FERMILAB
LIBRARY

APB7022

Abstract

Neutral Strange Particle Production

in $\pi^- p$ Interactions at 147 GeV/c

By Tungching Ou

Thesis Director: Professor Terence L. Watts

The production of K_S^0, Λ, $\bar{\Lambda}$, and γ in $\pi^- p$ collisions at 147 Gev/c is analyzed. We present neutral single particle distributions, energy dependence of average neutral multiplicities in $\pi^- p$ and pp collisions, neutral-charged correlations in the KNO framework, and two-particle inclusive neutral cross sections.

Acknowledgements

I would like to thank

Terry Watts, for his guidance over the years;

members of the bubble chamber group who have lent me their expertise on almost every phase of the experiment --- Rich Plano, Lenny Koller, By Brucker, Pete Stamer, and Pieter Jacques;

the scanners and PEPR operators at Stevens, Rutgers, and the rest of the consortium, for the difficult job of measuring the film;

Ray Badiak and Annamary McCann, for fixing all kinds of computer troubles;

Shukong, for drawing Fig. 30;

and finally my wife Annie, for her support and encouragement.

Table of Contents

	page
ABSTRACT	ii
ACKNOWLEDGEMENTS	iii
LIST OF FIGURES	vi
LIST OF TABLES	viii
1. WHY NEUTRAL STRANGE PARTICLES?	1
2. DATA ACQUISITION AND PROCESSING	2
2.1 Apparatus and Film	2
2.2 Overview of Data Acquisition	5
2.3 Weights	8
2.4 Scanning	8
2.5 IPD/PEPR/GEOMAT	17
2.6 Wire Chamber Tracks	23
2.6.1 Reconstruction	23
2.6.2 Momentum Determination	24
2.7 Kinematic Fitting	25
2.7.1 The Method	25
2.7.2 Quality of Fitted Data	36
2.8 Decay Volume and Minimum Path Length	38
2.9 Re-measurements and Measuring Weights	44
2.9.1 Factoring out the Event Weight	45
2.9.2 Scan-2 only Neutrals	46
2.9.3 2nd-pass-only Neutrals	46
2.9.4 Consistency with Flux Factor	47

Table of Contents page

3. RESULTS 49

3.1 Single Particle Inclusive Distributions 49

3.2 Beam Particle and Energy Dependence 64

3.3 Neutral-charged Correlations 71

3.4 Neutral-neutral Correlations 85

4. CONCLUSIONS 87

APPENDICES

1. Excerpts from rules for Scan-1A 88

2. The Simplex Approximation 94

NOTES AND REFERENCES 100

VITA 105

List of Figures

		page
1.	A schematic diagram of the apparatus	4
2.	The data processing chain	6
3.	Scanning efficiency variables	12
4.	Multiplicity distributions from scanned events (a) Scan-2 only, 10 rolls (b) common, 10 rolls (c) single-scanned 27 rolls	14
5.	RMS deviation on film	19
6.	Momentum errors quoted by GEOMAT	20
7.	Distribution of track length	21
8.	Pull distributions for 3-C γ fits	28
9.	Pull distributions for 3-C K_s^o fits	29
10.	Pull distributions for 3-C Λ fits	30
11.	Pull distributions for 3-C $\bar{\Lambda}$ fits	31
12.	Chi-squared probability for 3-C fits	32
13.	Difference between measured and fitted angles (a) 3-C fits (b) 1-C fits	33
14.	Decay angular distributions	37
15.	Sum of decay weights vs. ℓ_{min}	43
16.	Transverse momentum distributions for neutrals	50
17.	Transverse momentum distributions for neutrals	51
18.	Neutral $\langle p_t^2 \rangle$ vs. x	53
19.	Neutral $\langle p_t^2 \rangle$ vs. y	54
20.	Charged particle $\langle p_t^2 \rangle$ vs. x	55

List of Figures page

21. Charged particle $\langle p_t^2 \rangle$ vs. y 56

22. Neutral $d\sigma/dx$ 57

23. Neutral $(2E/\pi\sqrt{s})\ d\sigma/dx$ 58

24. Neutral $d\sigma/dy$ 59

25. Charged particle $d\sigma/dx$ 60

26. Charged particle $(2E/\pi\sqrt{s})\ d\sigma/dx$ 61

27. Charged particle $d\sigma/dy$ 62

28. Neutral cross sections vs. energy 65

29. Neutral multiplicity vs. energy 66

30. Beam and energy dependence of $\langle n_c \rangle$, from Ref.[29] 67

31. Fits to the energy dependence of $\langle n_{K_s^o} \rangle$ 69

32. Semi-inclusive charged particle cross sections; curve is $\Phi_s(z)$ 74

33. Semi-inclusive charged particle cross sections; curve is $\Phi_{23}(z)$ 75

34. Semi-inclusive π^o cross sections; curve is $\Phi_{23}(z)$ 77

35. Semi-inclusive K_s^o cross sections; curve is $\Phi_{23}(z)$ 78

36. Semi-inclusive Λ cross sections; curve is $\Phi_{23}(z)$ 79

37. Semi-inclusive $\bar{\Lambda}$ cross sections; curve is $\Phi_{23}(z)$ 80

38. 3-parameter fit to π^o data 82

39. 3-parameter fit to K_s^o data 83

40. 3-parameter fit to Λ data 84

41. The fiducial volume 90

42. A feasible region in 2-dimensions 97

List of Tables

		page
1.	Summary of scan efficiency calculations	15
2.	Measurement losses (PEPR/GEOMAT)	22
3.	Fit losses and misc. unwanted neutrals	38
4.	Constants used in decay weight calculations	40
5.	Decay volume parameters	42
6.	Sum of decay weights vs. box size	45
7.	Neutral weights	47
8.	Total inclusive neutral cross sections	49
9.	Moments of $d\sigma/dx$ distributions	63
10.	3-parameter fits to neutral data	81
11.	Inclusive two-particle neutral cross sections	85

Chapter 1: Why Neutral Strange Particles?

In inelastic high energy πp and pp collisions, charged pions are produced abundantly, and to a lesser extent, protons. Both have been extensively studied. It is obviously of interest to learn the composition and characteristics of the less abundantly produced strange particles. But little has been done on $K^{\pm}$ production in a 4π detector because the identification of medium and high energy $K^{\pm}$'s is difficult. Neutral-strange-particles which decay into charged pairs can be studied more easily in bubble chamber experiments. The unique V^{o} signatures allow for almost un-biased detection and the decay kinematics permit almost un-ambiguous identification.

The purpose of this chapter on data acquisition is to explain how we obtained the various cross sections presented in the next few chapters. We are interested in reactions of the form

$$\pi^- p \longrightarrow (K_S^0 \text{ or } \Lambda \text{ or } \bar{\Lambda} \text{ or } \gamma) + \ldots.$$

Our basic approach is to measure the 4-momenta of as many of the final state particles as possible. The first section describes the apparatus and the film. The second section is an overview of the long data processing chain which "transforms" pictures of bubbles into momentum 4-vectors. Of course we are interested in more than just a set of momentum 4-vectors. We want to calculate cross sections. For each momentum 4-vector, there is a rule, or recipe, which describes how the 4-vector may be used to calculate various cross sections. Each link in the the data processing chain can potentially influence the recipe. To make these recipes more explicit, the idea of weights is introduced in the third section. The rest of the chapter then describes the data processing chain in detail --- how each link transforms the raw data, and the weight each link contributes to the recipe.

2.1 Apparatus and Film

The results presented in this thesis are obtained from an experiment [1] done at Fermilab using a 147 Gev/c π^- beam incident on the 30" bubble chamber filled with hydrogen and

sandwiched by multi-wire proportional chambers (PWC's). A schematic diagram of the apparatus is shown in Fig. 1.

Each upstream chamber located at A, B, and C consists of three planes of 2mm-spaced parallel wires oriented at 120 degrees from each other with a 10 cm x 10 cm active area. Each downstream chamber at D, E, F, G, and H has a 31 cm x 31 cm active area. Chamber G includes two additional planes staggered for greater measurement precision; chambers D and F each have one additional plane. Chamber H, sitting behind 1.27 cm (2.27 radiation length) of lead, with an effective wire spacing of 6 mm, serves as a γ ray detector. Nearly all charged particles with momentum greater than 20 Gev/c were accepted by chambers DEF; the set DEFG had essentially full acceptance at 50 Gev/c [2].

A Cerenkov counter[3] and a muon counter were used to tag the beam. The muon counter, situated down-stream of the entire system, consists of 100 cm of lead followed by a 30 cm x 60 cm x 0.6 cm scintillator which in turn is backed up by 320 cm of concrete and another scintillator.

During the experiment, the bubble chamber magnet was set for a 26.8 kgauss field. The beam contained 94.2% π^- with momentum p= 147.75 Gev/c and dispersion $\Delta p/p$ ~0.9%. 1.9% of the beam were K^-; the rest were $\bar{p}$ and μ^-. Four spills with approximately 6 particles each were delivered to the bubble chamber every accelerator cycle. On each spill, three cameras photographed the bubble chamber on 35 mm film;

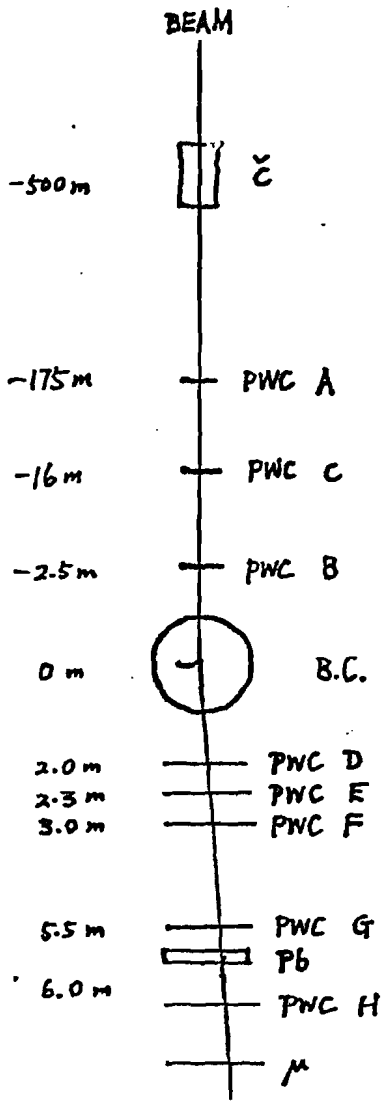

Fig 1. A schematic diagram of the apparatus

signals from the PWC's, Cerenkov counter, and muon counter were read out by an on-line PDP-9 and written onto magnetic tape.

We took 105K pictures in 40 rolls. Two rolls of film were taken with the magnetic field turned off for the purpose of calibrating the PWC's relative to the bubble chamber. One roll was lost at Cincinnati airport. The rest, ~97K pictures in 37 rolls, was used in this analysis.

2.2 Overview of Data Acquisition

Fig. 2 is a schematic diagram for the major links in the data processing chain. We start with bubble chamber film, combine it with the PWC data, and end up, after one or more tries, with a set of momentum 4-vectors which may be used to calculate cross sections. In this section we shall describe only the general features of these links and supply the details later.

The heart of the system is a automatic precision measuring machine called PEPR. It consists of a CRT and photomultipliers to detect the amount of light from the CRT that passes through the film. Under the control of an online computer, one can generate on the CRT either a spot to detect individual bubbles or a line segment at various angles to detect a large number of neighboring bubbles that make up a charged particles's trajectory. With a little help, PEPR "reads" the bubble chamber picture and writes out coordinates of 10 to 20 points on the trajectory of each

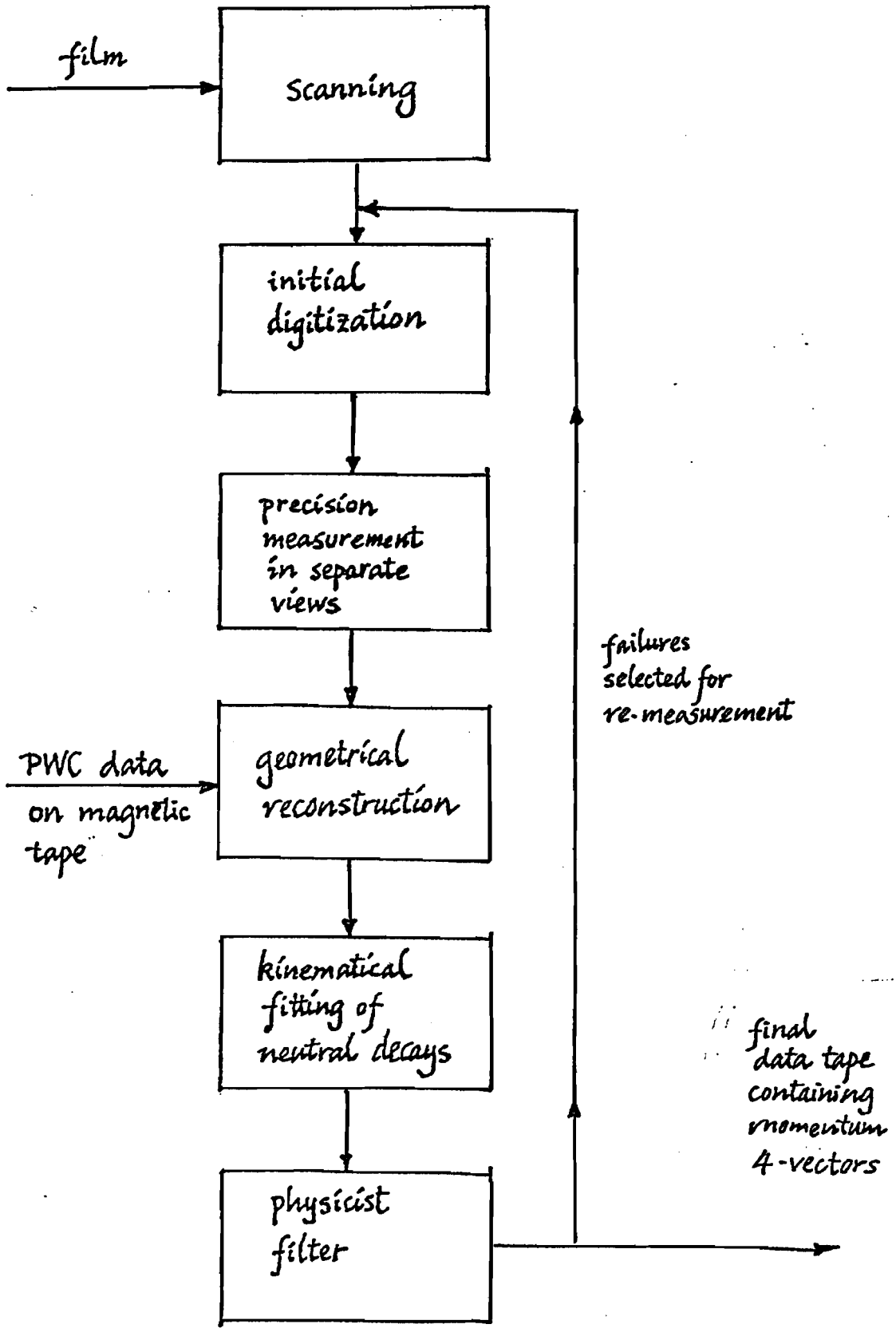

Fig 2. The data processing chain

charged particle accurate to 3μ on film or approximately 60μ in space.

Professional scanners do the scanning and initial digitization on image-plane-digitizing tables (IPD's). Scanning involves a careful examination of every picture to pick out those containing interactions of interest according to a strict set of scan rules. After an interaction is selected, a rough measurement of 2 or 3 points is made on each charged particle trajectory in each of 3 views. In addition to these IPD points which are used to guide PEPR, the event topology, including the number of charged and neutral particles, and miscellaneous book-keeping information are also recorded on magnetic tape.

Geometrical reconstruction is carried out by the program GEOMAT. PEPR output, organized by camera images and consisting of three sets of 2-dimensional particle trajectories, are matched and 3-dimensional trajectories are computed. The magnitude of the momentum vector, p, is determined from curvature; and the angles, from the tangent to the trajectory at the interaction vertex. For the tracks reconstructed from bubble chamber data, $\Delta p/p \sim 0.0069[\mathrm{Gev/c}]^{-1}p$ (i.e. 6.9% at 10 Gev/c).

Straight line trajectories of particles passing through the PWC's are reconstructed by the program PWGP. Another program TRACK ORGANIZER then hooks up trajectories in the bubble chamber and in the PWC's. For tracks passing through

the entire downstream PWC system, $\Delta p/p \sim 0.0006[\text{Gev/c}]^{-1}p$ or 6% at 100 Gev/c.

The program SQUAW obtains the mass and vector momentum of neutral vee particles by applying energy-momentum conservation constraints to the neutral decay vertices.

Finally, physicists look at all of the data. By examining the bubble density, protons and pions with momentum less than ~1.5 Gev/c may be distinguished. Some mistakes are corrected; some data are flagged as unacceptable; and others are selected for another pass through the system.

2.3 Weights

A weight is the inverse of a probability or an efficiency for detecting and processing vees. In this experiment, each neutral is assigned an over-all weight which is the product of weights, one for the losses at each step in the data processing chain. Cross sections are computed from the weighted number of neutrals. For example, suppose the chain consists of two steps, finding a neutral and measuring it. Say the finding efficiency is $\frac{1}{3}$ and the measuring efficiency is $\frac{1}{2}$. Then the over-all weight would be 3x2=6 and for every neutral successfully found and measured, there are 5 others that were either not found or not measured.

2.4 Scanning

Scanning is the process of carefully looking at every bubble chamber picture and recording all neutral particles of interest. All together, we made three passes over the

film looking for neutrals. In each pass, there were slight differences in the scan rules used. But the following general features remained the same: primary interactions had to be inside a well defined fiducial volume; events were rejected as crowded if there were more than 10 incoming beam tracks or more than 10 incoming secondaries; a V^o topology anywhere in the picture was recorded unless the neutral vertex was not visible in all three views or the neutral obviously did not point back to a valid primary vertex; and the multiplicity of the primary vertex was always recorded along with the frame number and other identification tags.

The first pass over all 97K pictures, which we shall call Scan-1A, was a group effort carried out by 8 separate institutions using the scan rules in Appendix 1. In order to determine the scanning efficiency, a second, independent pass over 27K pictures, called Scan-2, was performed using essentially the same rules except that only events containing neutral particles were recorded. Since only about 16% of the events contained V^o topologies, concentrating on the neutral events reduced the work load and improved the scanning efficiency. The quality of Scan-2 was much better than Scan-1A mainly because the scanners were more carefully supervised. The third pass, called Scan-1B, was made to check and correct Scan-1A. In it, only those frames in Scan-1A which contained either V^o topologies or event dependent rejects were covered. The scan rules used in Scan-1B and

Scan-2 contained two improvements. The first was the elimination of the un-measurable event reject. It turned out that the events rejected as un-measurable during Scan-1A contained abnormally large number of neutrals and high multiplicity events. The other improvement called for the scanner to classify a neutral into one of three categories, curly-gamma (zero opening angle and identified e^+/e^-), or straight-gamma (zero opening angle), or V (non-zero opening angle), instead of just two categories before. Scans 1B and 2, as well as all IPD'ing for those scans, were done by the component of the Rutgers-Stevens B.C. Group at Stevens.

The assignment of scan weights is based on a complete scan over all 37 rolls (Scan-1) and a second, independent, partial scan over 10 rolls containing ~28% of the incident beam flux (Scan-2). In the doubly scanned portion of the film, let

$n-m$ be the true number of neutrals,

N_1 be the number of neutrals recorded by Scan-1 only,

N_2 be the number of neutrals recorded by Scan-2 only,

N_{12} be the number of neutrals recorded by both scans.

In the singly scanned portion of the film, let

m be the true number of neutrals,

M_1 be the number of neutrals recorded by Scan-1.

We wish to estimate n, the true number of neutrals in all the film. Assuming that finding a neutral in Scan-1 and Scan-2 are independent Poisson trials with probabilities e_1

and e_2 respectively, then we expect

$$\begin{aligned} N_1 &= (n-m)e_1(1-e_2) \\ N_2 &= (n-m)(1-e_1)e_2 \\ N_{12} &= (n-m)e_1e_2 \\ M_1 &= me_1 \end{aligned} \qquad (1)$$

Equations 1 may be represented geometrically as a set of rectangles shown in Fig. 3. The lower case variables that we wish to calculate, (n,m,e_1,e_2), are denoted by line segments on the horizontal and vertical axes. The capitalized quantities that are experimentally measured, (N_1,N_2,N_{12},M_1), are denoted by areas of rectangles. The shaded regions with total area a+b represent neutrals on the film that were not recorded. The quantity e_{12} defined by

$$\begin{aligned} e_{12} &= e_1(1-e_2) + e_1e_2 + (1-e_1)e_2 \\ &= e_1 + e_2 - e_1e_2 \end{aligned}$$

can be interpreted as the combined scan efficiency on the doubly scanned portion of the film. By solving Fig. 3 geometrically or inverting equations 1 algebraically, we get

$$\begin{aligned} e_1 &= N_{12}/(N_2+N_{12}) \\ e_2 &= N_{12}/(N_1+N_{12}) \\ n-m &= (N_1+N_{12})(N_2+N_{12})/N_{12} \\ m &= M_1(N_2+N_{12})/N_{12} \end{aligned}$$

The estimated true number of neutrals in all of the film is

$$n = (N_1+N_{12}+M_1)(N_2+N_{12})/N_{12} \quad ;$$

the total number of recorded neutrals in all of the film is

$$N = N_1 + N_2 + N_{12} + M_1 \quad .$$

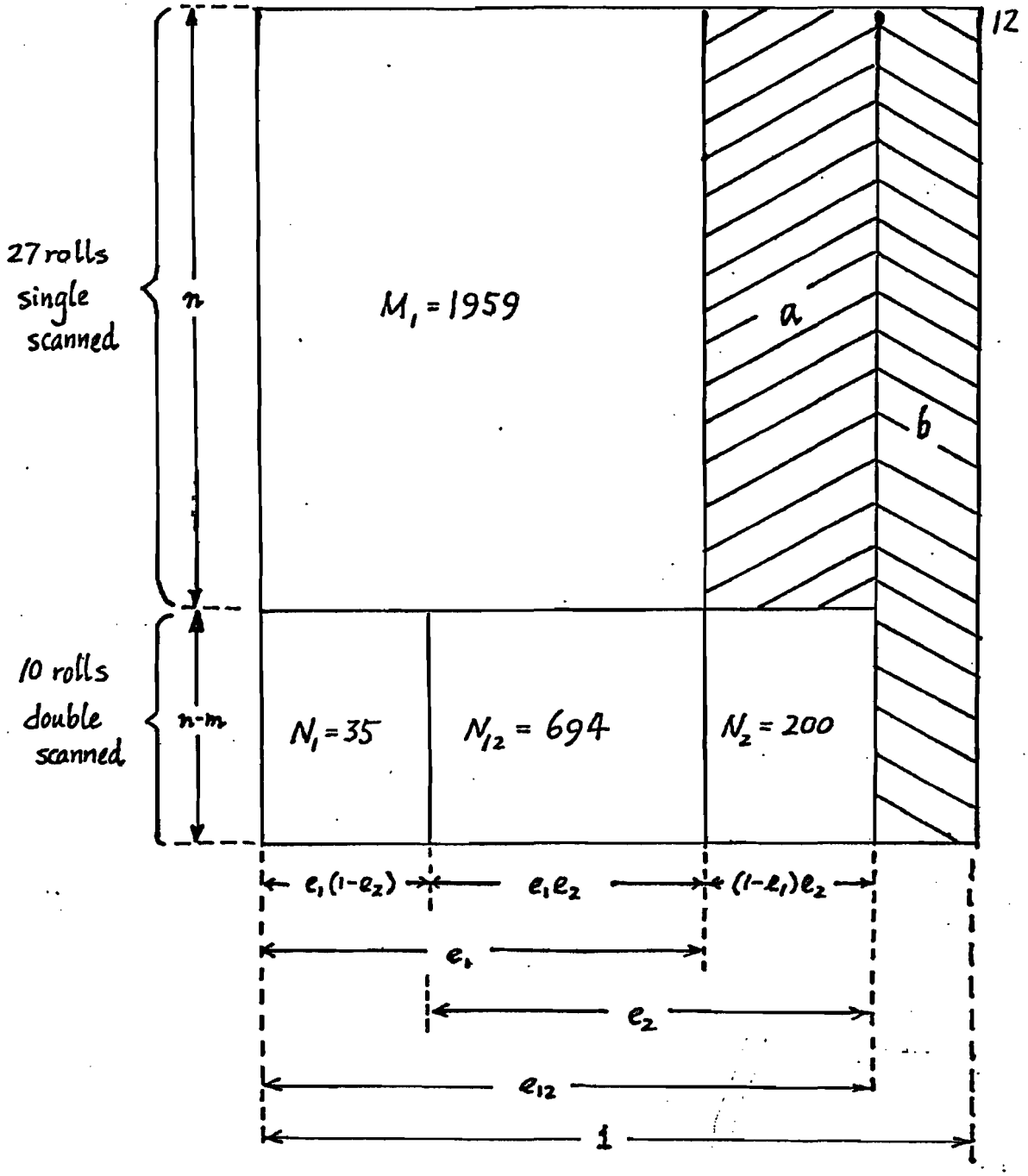

Fig 3. Scanning efficiency variables

Listed in Table 1 are the numerical values of all the important quantities in the scan efficiency calculations.

Remember that equations 1 are based on the assumption that the scanning efficiencies are uniform, i.e. the probability of finding a neutral does not depend on the roll number in which a neutral is found, or the multiplicity of the primary interaction with which a neutral is associated, or the momentum of the neutral, etc. We can make two checks on this assumption of uniform scan efficiency. First note that we should have

$$\frac{n}{n-m} = \frac{1}{1-F}$$

where F is the fraction of the film single-scanned, determined from beam count. Consulting Table 1, we see it is satisfied within the errors. The other test is to make sure that neither Scan-1 nor Scan-2 is biased toward high multiplicity events. This is demonstrated by Fig. 4. The three multiplicity distributions are very similar except for the variation in the 2-prong bin which suggest that the scanning efficiency for neutrals associated with 2 prongs is slightly worse than average during Scan-1.

To support further the idea that the scanning efficiency is uniform, we should show several similar neutral momentum distributions showing no high momentum bias in any one group of neutrals. We will not give such a demonstration for the following reasons. The momentum of a neutral, unlike the multiplicity, is not determined at the scan table; it has to

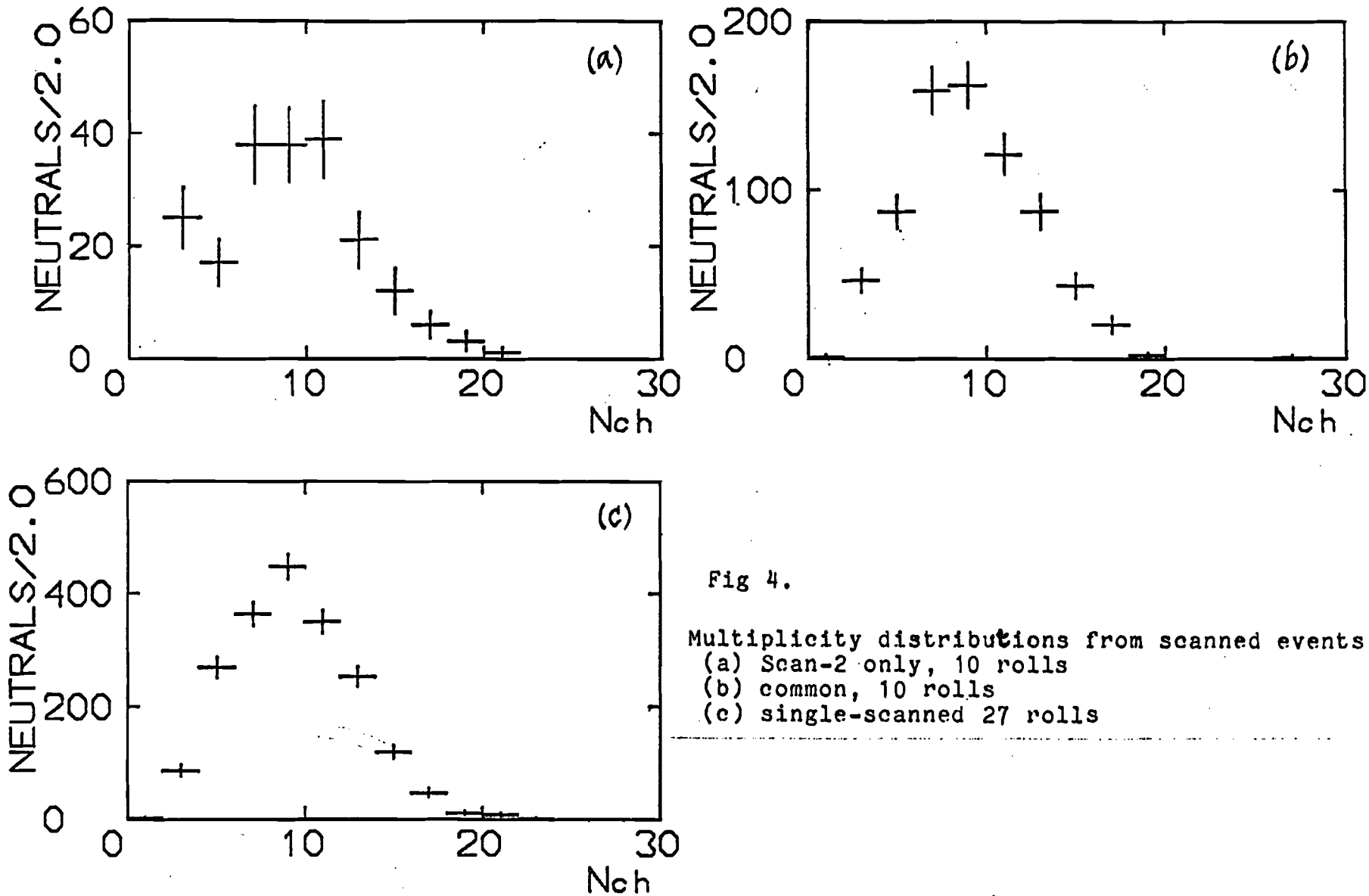

Fig 4.

Multiplicity distributions from scanned events
(a) Scan-2 only, 10 rolls
(b) common, 10 rolls
(c) single-scanned 27 rolls

Table 1 Summary of scan efficiency calculations

N_1	Scan-1 only (10 rolls)	= 35
N_2	Scan-2 only (10 rolls)	= 200
N_{12}	common (10 rolls)	= 694
M_1	Scan-1 (27 rolls)	=1959
F	fraction of film single-scanned	$=0.7213\pm0.0053^a$
e_1	$= N_{12}/(N_2+N_{12})$	$=0.776\pm0.014^b$
e_2	$= N_{12}/(N_1+N_{12})$	$=0.952\pm0.008^b$
e_{12}	$= e_1 + e_2 - e_1e_2$	$=0.989\pm0.002^b$
$\frac{n}{n-m}$	$=(M_1+N_1+N_{12})/(N_1+N_{12})$	$=3.687\pm0.117^b$
$\frac{1}{1-F}$		$=3.588\pm0.010^a$

a: Determined from counting 12210 beam tracks in 10 roll sample and 31600 beam tracks in the 27 roll sample.

b: Errors determined by setting variance(M_1)=M_1, similarly for N_1, N_2, N_{12}.

be measured. But the measurement process was neither 100% efficient nor uniform. Neutrals in the 27 single-scanned rolls were measured only once; for the neutrals in the 10 double-scanned rolls, the ones that failed on the first measurement pass were re-IPD'ed and re-measured on a second pass. Thus if we plotted the momentum distribution of successfully measured neutrals from the Scan-1 27 roll sample compared to those from the Scan-2 only 10 roll sample, the distributions will probably differ because one sample is more carefully scanned <u>and</u> more carefully measured than the other. It is very difficult to separate the

scanning biases from the measuring biases; we will not attempt to do so. And, as we shall see, it is not necessary.

To compensate for the scanning inefficiencies, there are two ways we can assign a total weight of n to N neutrals. In the uniform weighting scheme, we assign an equal weight $w_o = \frac{n}{N}$ to all the neutrals. The other scheme singles out the N_2 Scan-2 only neutrals for special treatment; we assign the weight $w_1 = 1/e_{12}$ to the Scan-1, Scan-1 only, and common neutrals, and assign the weight

$$w_2 = w_1 \left(\frac{n}{n-m}\right) = w_1 \left(\frac{1}{1-F}\right) \qquad (2)$$

to the Scan-2 only neutrals. That both schemes yield the same total weight n can be verified from the identity

$$n = Nw_o = (N_1+N_{12}+M_1)w_1 + N_2w_2$$

but the uniform weighting scheme gives a smaller error since

$$Nw_o^2 \leq (N_1+N_{12}+M_1)w_1^2 + N_2w_2^2$$

If everything else were equal, the uniform weighting scheme is preferable. However, if there are biases in scanning or measuring or both, then the non-uniform scheme is better. This can be most clearly seen by considering Fig. 3. Suppose the neutrals in region N_2+a have momenta larger than the rest of the neutrals, then giving every neutral an equal weight will suppress the high momentum end of the momentum distribution; but the momentum distribution will not be biased if the Scan-2 only neutrals are given a weight larger by the flux factor $\frac{1}{1-F}$. The disadvantage of using the non-uniform weighting scheme is that the large weights reduce

the statistical significance of the results. But that is the penalty we have to pay for not re-scanning and re-measuring all of the film.

2.5 IPD/PEPR/GEOMAT

The first part of the measurement process consists of measuring momenta of charged particles on bubble chamber film. The trajectory of each charged particle, called a track, is measured one at a time. In IPD and PEPR, each view is also measured separately.

Tracks of the decay products of neutrals were IPD'ed in all of the film as well as secondary tracks in 2, 4, and 6 prong events. But secondary tracks in ≥ 8 prong events were IPD'ed only in 10 of the 37 rolls, and only if a neutral strange particle (K_S^0, Λ, or $\bar{\Lambda}$) was present. This was done at a time before we were confident of our ability to measure events with many secondaries.

In the first measurement pass, the PEPR operator was allowed to reject a track if the program failed to find it after several tries. Such a reject does not necessarily mean the track is lost since reconstruction from two views is possible. However, in the re-measurement pass over 10 rolls, the PEPR operator was instructed to measure a track manually if the program could not find it automatically. For this purpose, the Rutgers PEPR was equipped with a high resolution analog display with independently adjustable x and y magnifications [4]. Measuring tracks manually was a

time consuming procedure but it made sure there is always some data in every view for the reconstruction program to work with. And it improved the measuring efficiency considerably.

The momentum accuracy of reconstructed tracks may be simply estimated as follows. Suppose the track of momentum p and length L is in a plane perpendicular to the magnetic field H, then

$$p = 3\times10^{-4}\left[\frac{\text{Gev/c}}{\text{kgauss-cm}}\right] H\ R$$

where R is the radius of curvature. In addition, suppose the turning angle $=\frac{L}{R} \ll 1$ then the sagitta can be written $s = L^2/8R$ and

$$\frac{\Delta p}{p}=\frac{\Delta R}{R}=\frac{\Delta s}{s} = \frac{8}{3}\times10^{4}\left[\frac{\text{kgauss-cm}}{\text{Gev/c}}\right]\frac{\Delta s}{H}\ p/L^2$$

Δs is given by the accuracy of PEPR measurements. Fig. 5 shows the RMS deviation of measured track points from the fitted trajectory for GEOMAT reconstructed tracks. It is of the order of 3μ on the film or 60μ in space. Setting $\Delta s=60\mu$ and H=26.8 kgauss , we expect

$$\frac{\Delta p}{p} \sim 6.0\left[\frac{\text{cm-cm}}{\text{Gev/c}}\right]\ p/L^2 \qquad (3)$$

This is drawn as a straight line in Fig. 6; the error calculation algorithm in GEOMAT gives results very close to the simple calculation above. Using eq. 3 and $\langle L\rangle$ = 29.5cm obtained from Fig. 7, we get

$$\frac{\Delta p}{p} = 0.0069\ [\text{Gev/c}]^{-1}\ p$$

The measurement losses are listed in table 2. In the top half of the table, out of a total of 795+1644=2439 events

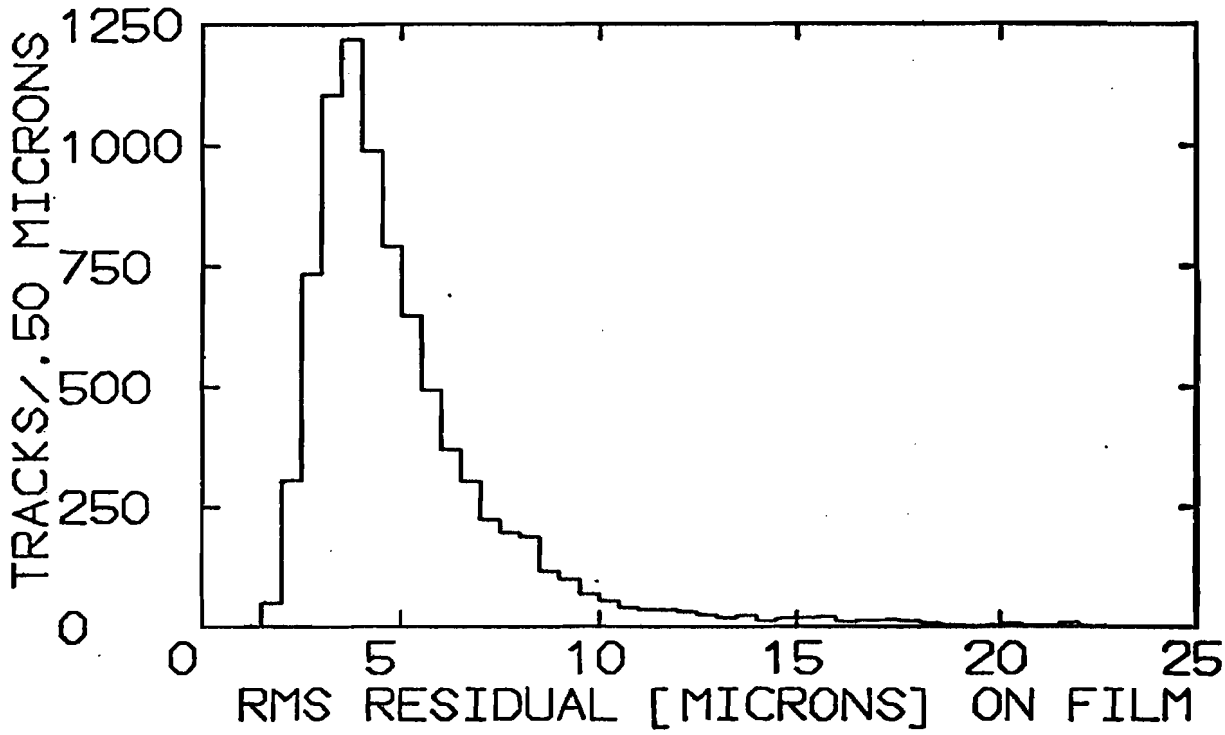

Fig 5. RMS deviation on film

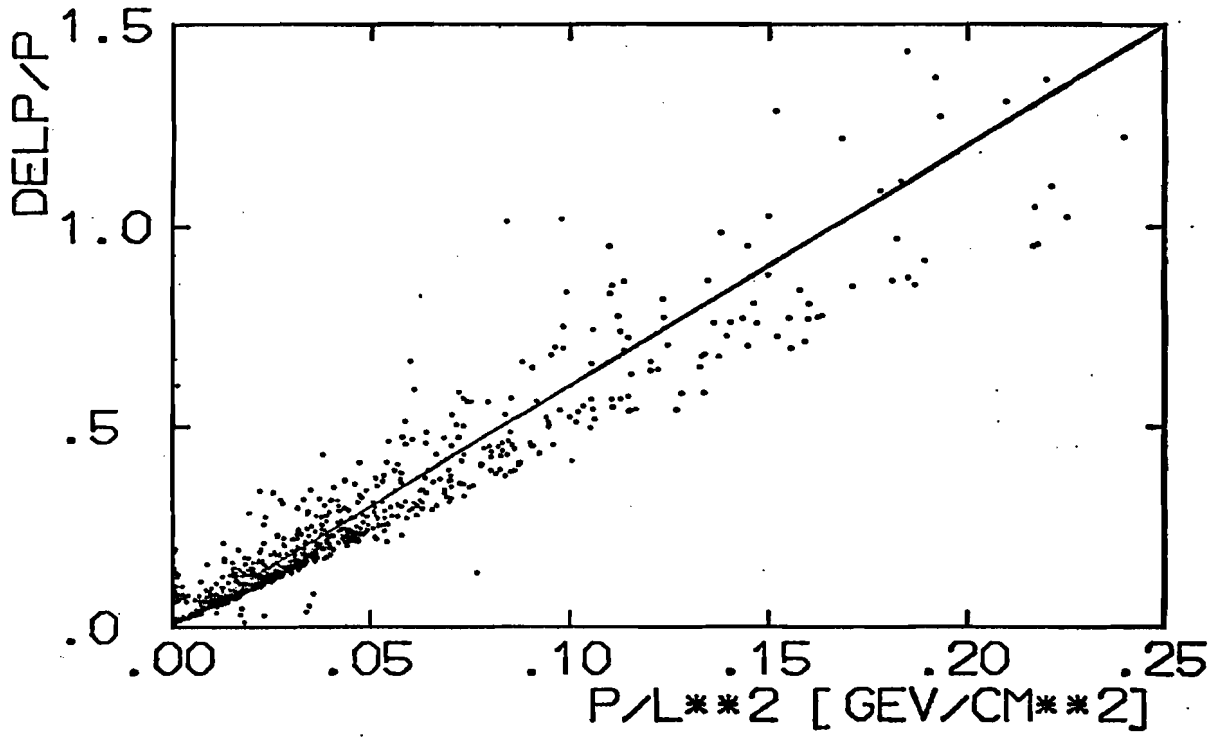

Fig 6. Momentum errors quoted by GEOMAT

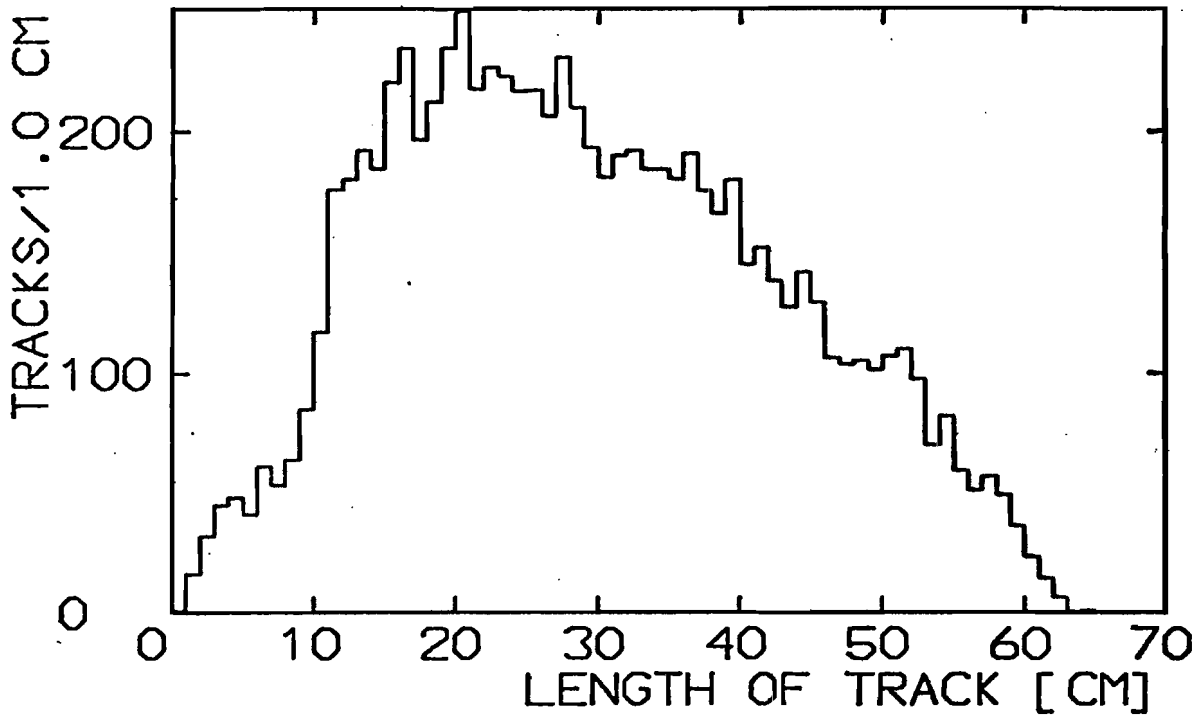

Fig 7. Distribution of track length

Table 2 Measurement losses (PEPR/GEOMAT)

	10 roll sample # lost	10 roll sample # remaining	27 roll sample # lost	27 roll sample # remaining
scanned	--	795 events	--	1644 events
tape errors	2	793	28	1616
rejects	13	780	86	1530
non-rejects	---	939 vrtcs	---	1824 vrtcs
no vertex	1	938	9	1815
outside	116	822	248	1567
no tracks	29	793	79	1488

scanned and IPD'ed, 30 events were lost due to magnetic tape read and write errors, and 99 events were GEOMAT rejects. These rejects correspond to catastrophic failures in which all of the information in the event is unusable, e.g. no PEPR data in two views, or no beam track reconstructed, or no primary vertex reconstructed. These two types of losses are enumerated in terms of events; the corresponding weights are applied to charged secondary tracks as well as neutrals.

In the bottom half of the table, we have tabulated the losses for neutrals in terms of neutral vertices. "No vertex" means a neutral vertex was not reconstructed. "Outside" means the reconstructed neutral vertex is located at the down stream end of the bubble chamber (x>25cm) and outside the decay volume. These neutrals are excluded to make sure that the tracks of the decay products are long

enough to be reasonably measured; they do not contribute to the measuring weight of neutrals. "No tracks" means either one or both tracks originating from the neutral vertex was not reconstructed.

Except for the tape errors which are random and unbiased, the measurement losses tend to be concentrated in events with fast neutrals or high multiplicity or both. High multiplicity events are more difficult to measure because the tracks of decay products of neutrals are more often obscured by charged particles from the primary vertex. In events with high momentum neutrals, the decay tracks have small opening angles and obscure each other. We have tried to assign neutral measurement weights in such a way to minimize the biases. This will be presented later in the section on re-measurements after a discussion of the kinematic fitting procedure and decay volume.

2.6 Wire Chamber Tracks

2.6.1 Reconstruction

Reconstructing particle trajectories in the PWC's is a simple task. It is much simpler than reconstructing tracks from the bubble chamber film because the data is already digitized and because the trajectories are just straight lines in a magnetic field free region.

All the wire planes are oriented perpendicular to the x-axis which is approximately along the beam direction. If the wires in the kth plane are placed a distance C apart and

make an angle W_k with respect to the z-axis, then the equation for the nth wire in the kth plane is

$$u \equiv y \cos W_k + z \sin W_k = \text{constant} = R_k + nC$$

A straight line track trajectory may be parametrized by

$$y = y_o + a(x-X_o)$$

$$z = z_o + b(x-X_o)$$

where y_o, z_o is the point at which the line intersects an arbitrarily chosen reference plane $x=X_o$ and a,b are the slopes. This line should intersect the kth plane at

$$y_k = y_o + a(X_k-X_o)$$

$$z_k = z_o + b(X_k-X_o)$$

and should fire the wire closest to

$$u = u_k \equiv y_k \cos W_k + z_k \sin W_k$$

The probability it will fire a wire at $u=v_k$ is proportional to $\exp[\ -(u_k-v_k)^2/2\sigma_k^2\ ]$ where $\sigma_k = (12)^{-1/2}C$ [5]. Since u_k is linear and homogeneous in the track parameters a, b, y_o, z_o, this is the well known linear least squares fit problem, it's straightforward to pick a wire in each plane, build a 4x4 matrix, and invert it to obtain the track trajectory.

For non-interacting beam tracks, the technique outlined above is all that is needed to separately reconstruct them in the upstream and downstream PWC's. The beam momentum, measured from the bending angle in the known magnetic field, is 146.75 ± 0.76 Gev/c [6].

2.6.2 <u>Momentum Determination</u>

For tracks originating from a vertex inside the bubble

chamber and traversing part or all of the downstream PWC's, measuring their momenta is done in two steps. First, straight line trajectories are reconstructed using the z coordinate of the primary vertex as an additional constraint since there is little bending in the x-z plane containing the $\hat{B}$ vector. In the x-y plane perpendicular to $\hat{B}$, the distance from the vertex to the trajectory, the impact parameter, is inversely proportional to the momentum. This step is carried out by the program PWGP.

The second step is carried out by the program TRACK ORGANIZER. Each trajectory reconstructed by PWGP is extrapolated through the known magnetic field back to the vertex and matched up with trajectories measured on the film. Tracks not matched up with some bubble chamber data are considered spurious and rejected. The momentum is then determined from the bending angle using both bubble chamber data and PWC data.

Only tracks from the primary vertex are measured this way. We did not attempt to reconstruct trajectories of the decay products of neutral decays in the PWC's.

2.7 Kinematic Fitting

2.7.1 The Method

The program SQUAW was used to classify the neutral decays into one of the following four categories:

$$K_S^0 \rightarrow \pi^+ \pi^-$$

$$\Lambda \rightarrow p \pi^-$$

$$\bar{\Lambda} \rightarrow \bar{p}\ \pi^+$$

$$\gamma\ p \rightarrow e^+\ e^-\ p$$

If a neutral were classified as a curly gamma on the scan table (i.e. contains an identified e^+ or e^-), then only the γ category was tried; otherwise, all four categories were tried. In each category, both 3-C and 1-C fits were attempted. The input to the 3-C fits consists of the 3-momenta of the charged decay products and the direction of the neutral (2 angles) obtained from the position of primary and secondary vertices. For 1-C fits, the direction of the neutral was not used. The momentum of the spectator proton in the γ fit was set to zero with a fixed error $\Delta p_x = \Delta p_y = 1.0$ MeV/c, $\Delta p_z = 1.3$ MeV/c ($\hat{z}$ is parallel to the camera axes, the direction with the worst stereo angle). The minimum probability was set to 10^{-4} corresponding to a chi-square of 21 for 3 degrees of freedom and 15 for 1 degree of freedom [7].

Using the errors calculated by GEOMAT, our initial fits gave pull distributions [8] which were too wide and X^2 distributions with excess of events at large X^2, indicating that the errors quoted by the reconstruction program were too small. The fact that a large fraction of neutrals failed 3C fits but fitted 1C hypotheses suggests the errors on the vertices were especially troublesome. Ideally we should take the time to understand why the errors are under-estimated and try to incorporate into the error calculations, effects

due to plural scattering, turbulence in the chamber, and uncertainties in the optical constants. But that is a difficult task. We shall be content with the more usual procedure of imposing artificial lower bounds on errors which seem unreasonably small and enlarging the errors in all the measured quantities, warranted or not, in an attempt to hide the problem.

In order to obtain satisfactory pull distributions after the 3-C fits, we had to adjust the errors on the momenta and vertex coordinates assigned by GEOMAT. We multiplied all momenta error matrices by 2. We also multiplied all vertex position error matrices by 2 after adding to them the constants $\Delta y=100\mu$, $\Delta z=500\mu$. (Δx did not contribute much to the error on the neutral angles since most of the neutrals were approximately parallel to $\hat{x}$, the beam direction). The resulting pull distributions are shown in Figs. 8-11 [9]; all are approximately Gaussians centered at zero with unit standard deviation.

The chi-squared probability distribution for 3-C fits are shown in Fig. 12. The excess of events at low probability indicate that even the adjusted errors are too small. In fact, about 13% of the neutrals in our final sample did not make any 3C fits and were classified according to the 1C fit results. We have examined these 1C fit neutrals on the scan table and believe the majority of them do point back to the primary vertex. Fig. 13 shows the 3C and 1C fitted angles

Fig 8. Pull distributions for 3-C γ fits

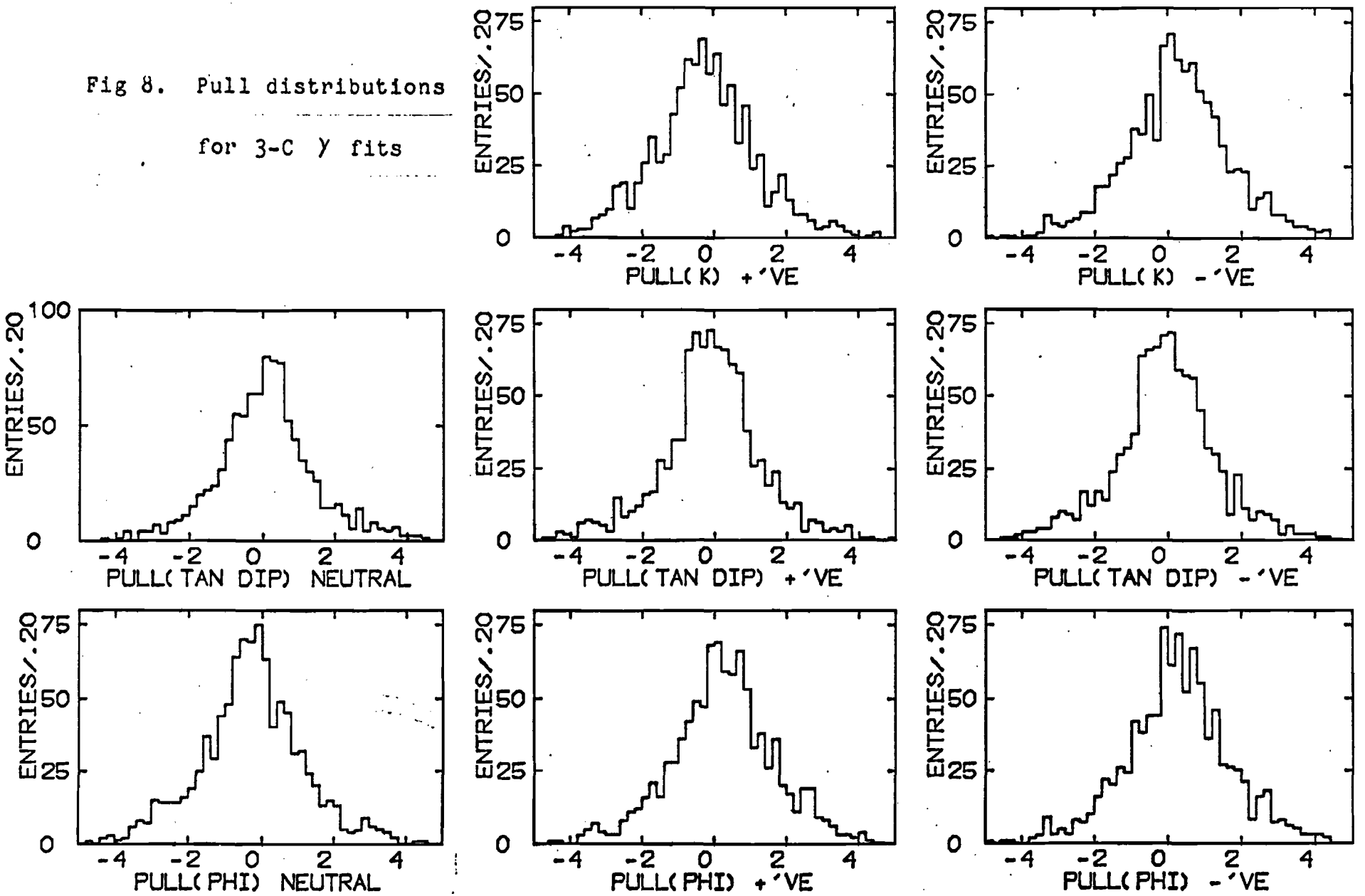

Fig 9. Pull distributions for 3-C K_S^0 fits

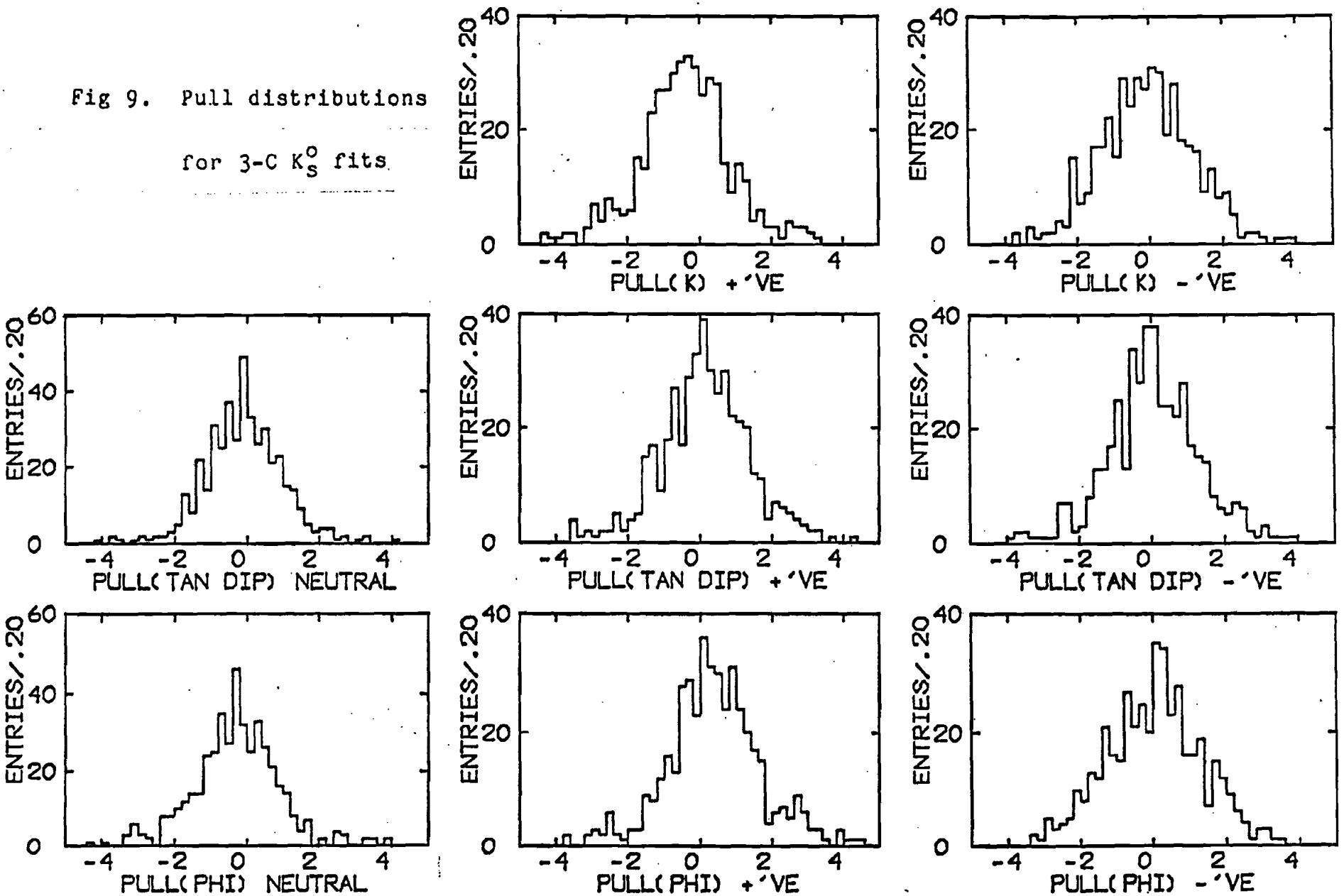

Fig 10. Pull distributions

for 3-C Λ fits

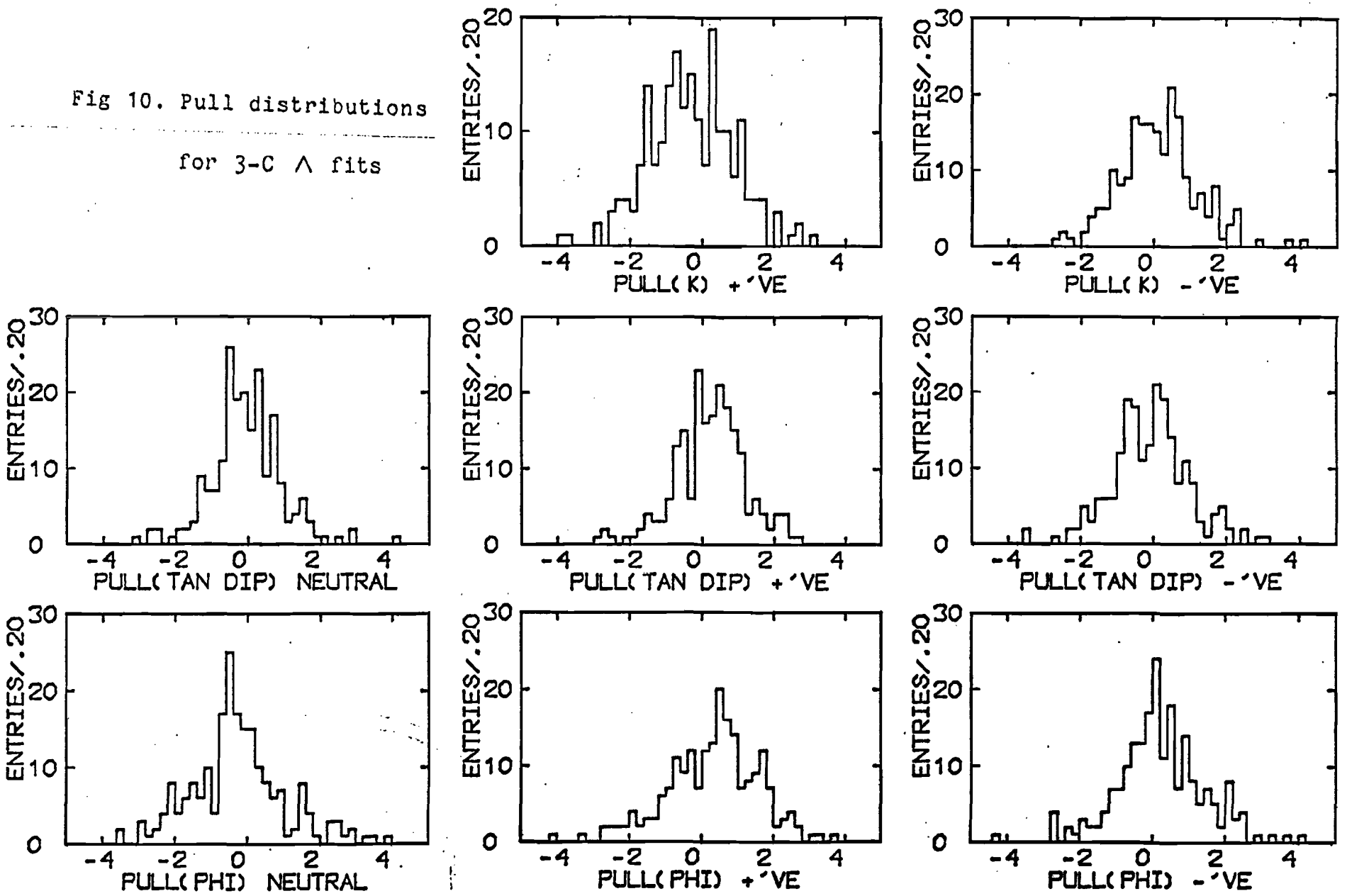

Fig 11. Pull distributions

for 3-C $\overline{\Lambda}$ fits

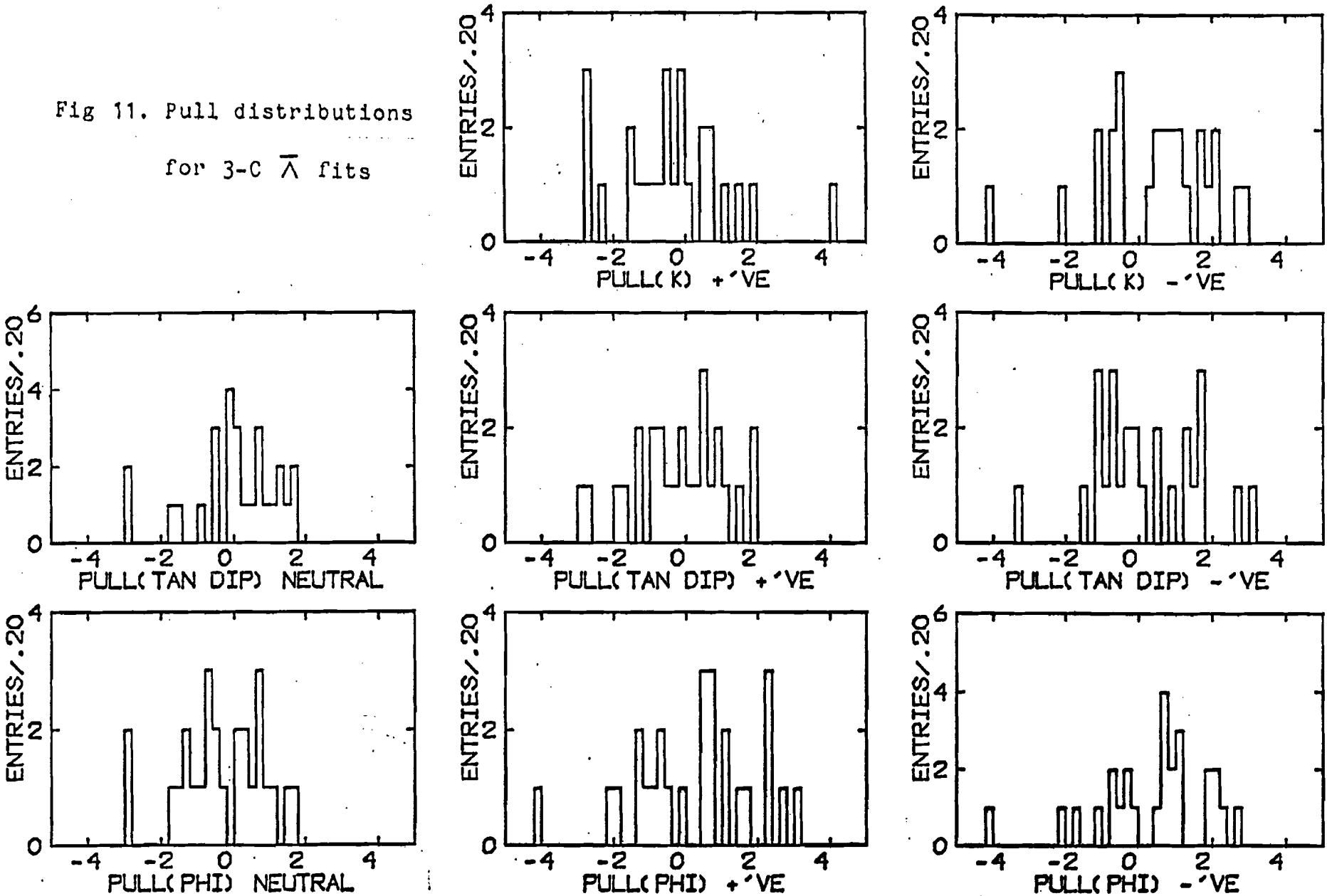

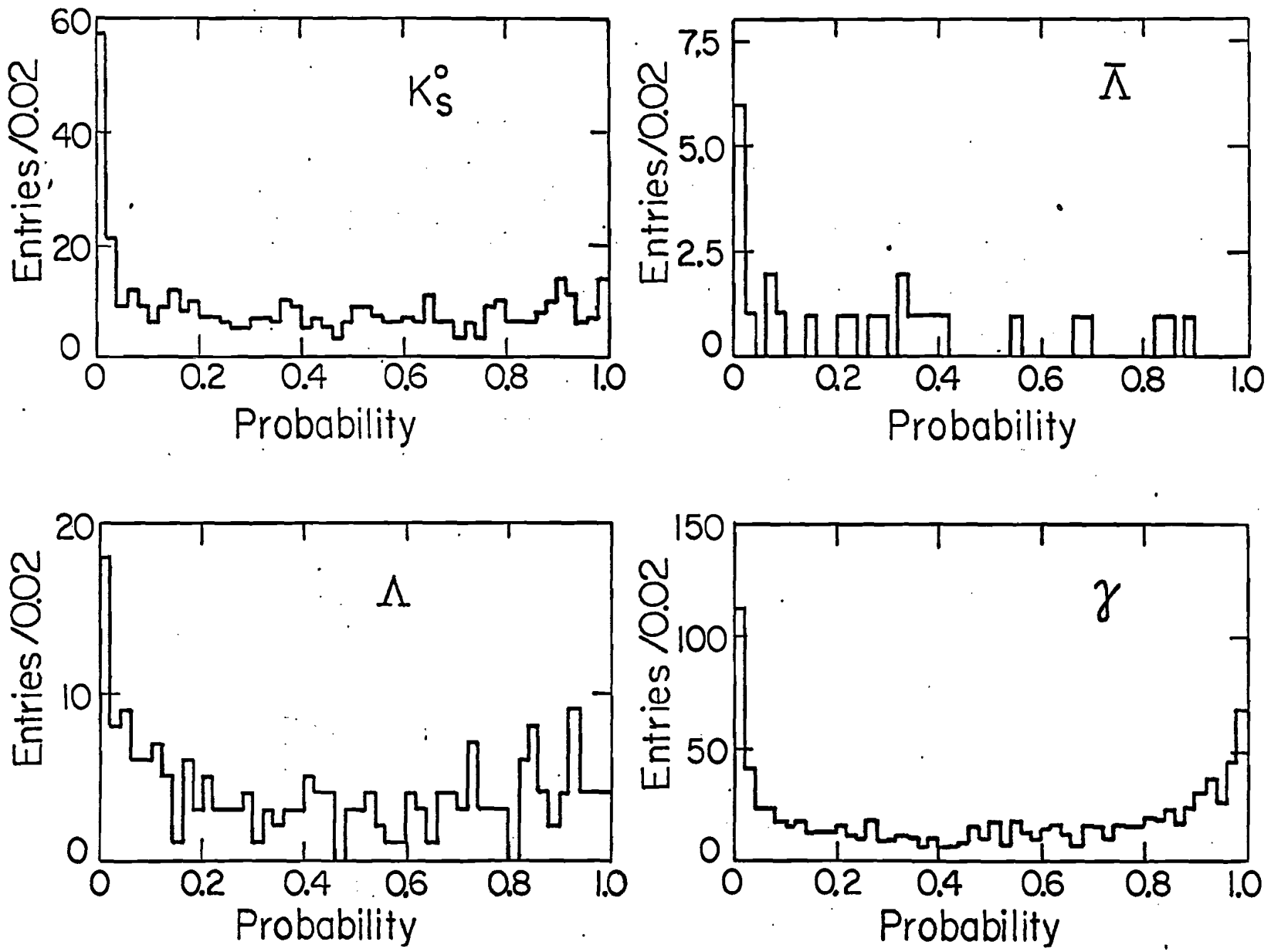

Fig 12. Chi-squared probability for 3-C fits

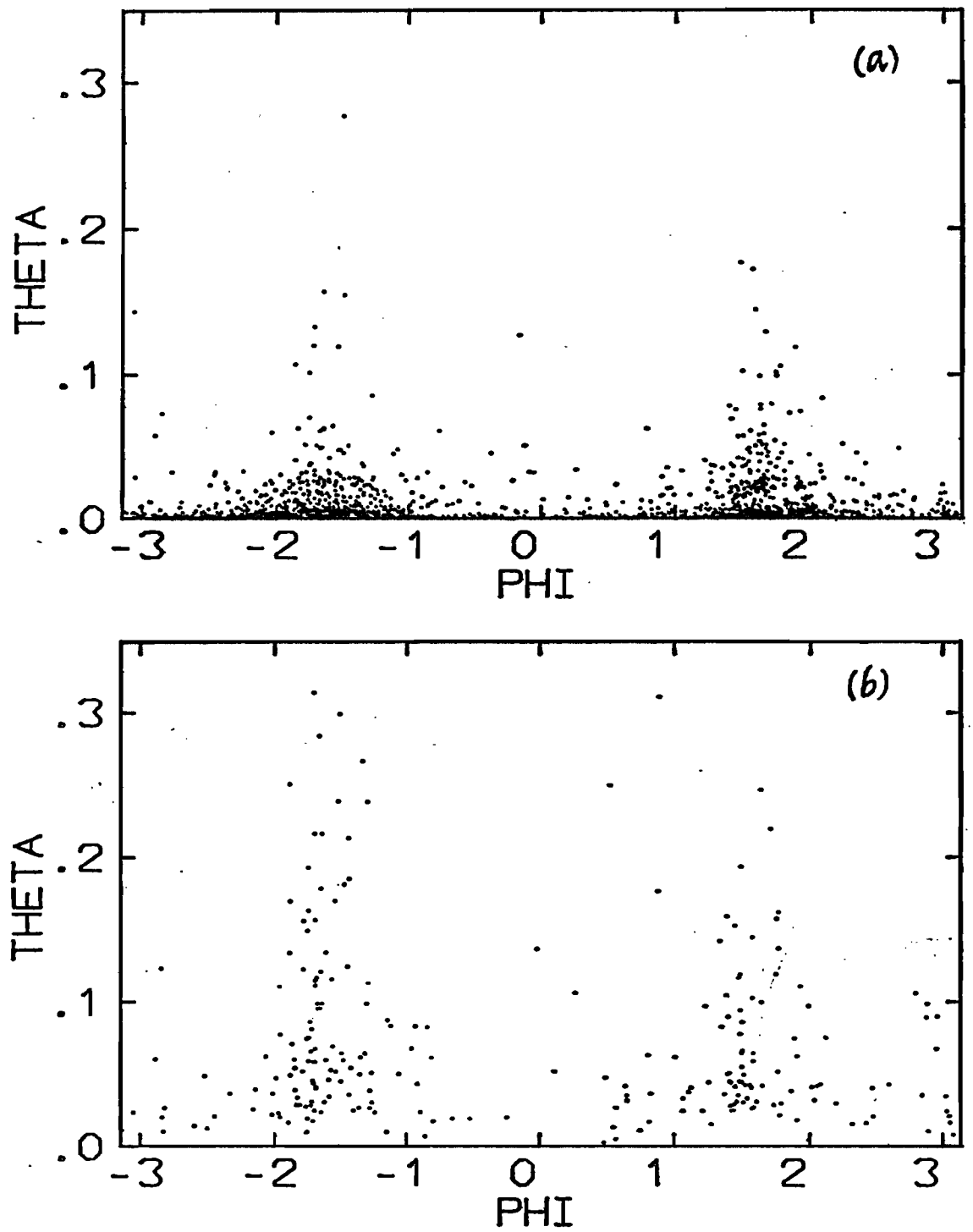

Fig 13. Difference between measured and fitted angles
(a) 3-C fits
(b) 1-C fits

relative to the measured neutral direction. θ is the angle between the fitted and measured neutral directions. ϕ is the azimuthal angle about the measured direction; $\phi=+\pi/2$ and $-\pi/2$ corresponds to directions toward and away from the camera respectively. For the 3C fits, events with small θ occur at all values of ϕ. But as θ increases, events tend to cluster around $\phi=\pm\pi/2$. This simply reflects the relatively poor measurement accuracy along the camera axis. In the 1C fits, the same correlation between large θ and $\phi=\pm\pi/2$ confirms what was found at the scan table -- that the neutrals do indeed point back to the primary vertex. If the 1C neutrals did not point back, we would expect them to be distributed at large θ and all values of ϕ. We have included all the 1C fits in our sample because we believe that their momenta and angles are accurate enough for the studies presented here.

All neutrals that made either a 3C or a 1C fit were examined on the scan table by physicists for quality of data. Events with poorly measured data or marginal fits were tagged and treated like measurement failures. If either one of the decay products could be identified as not an electron or positron, then the γ fit was rejected; e.g. large opening angle, larger than minimum ionization, or a secondary interaction. Whenever one of the decay products was very slow, the fits that were inconsistent with the ionization were rejected. Some neutrals were IPD'ed and measured twice

because there were two primary interactions in the same frame; if a neutral has already been associated with one primary vertex, then the other occurrence was tagged as a non-pointer to prevent counting it twice.

In our final sample of 1896 neutrals, the 270 that still fitted more than one decay process after the physicist inspection were resolved by the following ordered tests:

(i) A γ fit, if present, was selected if the transverse momentum of the negative track with respect to the direction of the neutral was less than 25 MeV/c. Otherwise, the γ fit was rejected.

(ii) A K_S^0 fit was selected if the transverse momentum of the negative track was greater than 105 MeV/c. 118 of the ambiguous fits were called γ, 45 K_S^0, 16 Λ, and 14 $\bar{\Lambda}$ by criteria (i) and (ii).

(iii) A $\bar{\Lambda}$ fit was selected only if its chi-square probability was at least three times that of the competing fits. This criterion was chosen to keep the ratio of unambiguous $\bar{\Lambda}$ fits to unambiguous K_S^0 and Λ fits approximately the same as the overall numbers of $\bar{\Lambda}$, K_S^0, and Λ fits in order to avoid too large a ratio of ambiguous to un-ambiguous $\bar{\Lambda}$ fits. 19 K_S^0, 1 Λ, and 1 $\bar{\Lambda}$ were assigned by this criterion.

(iv) The remaining K_S^0-Λ ambiguities were resolved by considering following two conditions: For the spinless K_S^0 decay, 14% of the decay products will have

transverse momentum below 105 MeV/c; secondly, a K_S^0 should simulate a $\bar{\Lambda}$ decay as often as a Λ decay. Both conditions could not be satisfied simultaneously so we have resolved the K_S^0-Λ ambiguities so that neither condition was badly violated. The criterion for a K_S^0 decay, then, is that the probability of the K_S^0 fit is 1.43 times that of the Λ fit. This resolved the last 56 ambiguous neutrals into 10 K_S^0 and 46 Λ.

2.7.2 Quality of Fitted Data

After kinematic fitting and miscellaneous other selection criteria, 1896 neutrals, consisting of 505 K_S^0, 238 Λ, 32 $\bar{\Lambda}$, and 1121 γ remained in the final sample. The losses are listed in Table 3. The "OCQD" category includes neutrals that made no fits at all as well as those that have been explicitly rejected by the physicist inspection. "Non-events" are events that should not have been IPD'ed and measured. "Non-pointers" are neutrals that definitely do not point back to the primary vertex. "K^- beam" are events containing beam tracks that have K^- Cerenkov tags [10]. "Min.p.l." refers to a 2 cm cut on the path length of the neutral which is discussed in the next section.

For strange particle decays, the angular distribution of the negative particle in the rest frame of the neutral are shown in Fig. 14. The coordinate system is chosen so $\hat{z}$ is along $\hat{p}$, $\hat{x}$ is along $\hat{p} \times \hat{c}$, and $\hat{y}$ is in the $\hat{p}$-$\hat{c}$ plane, where $\hat{p}$, $\hat{c}$ are respectively the direction of the neutral and the

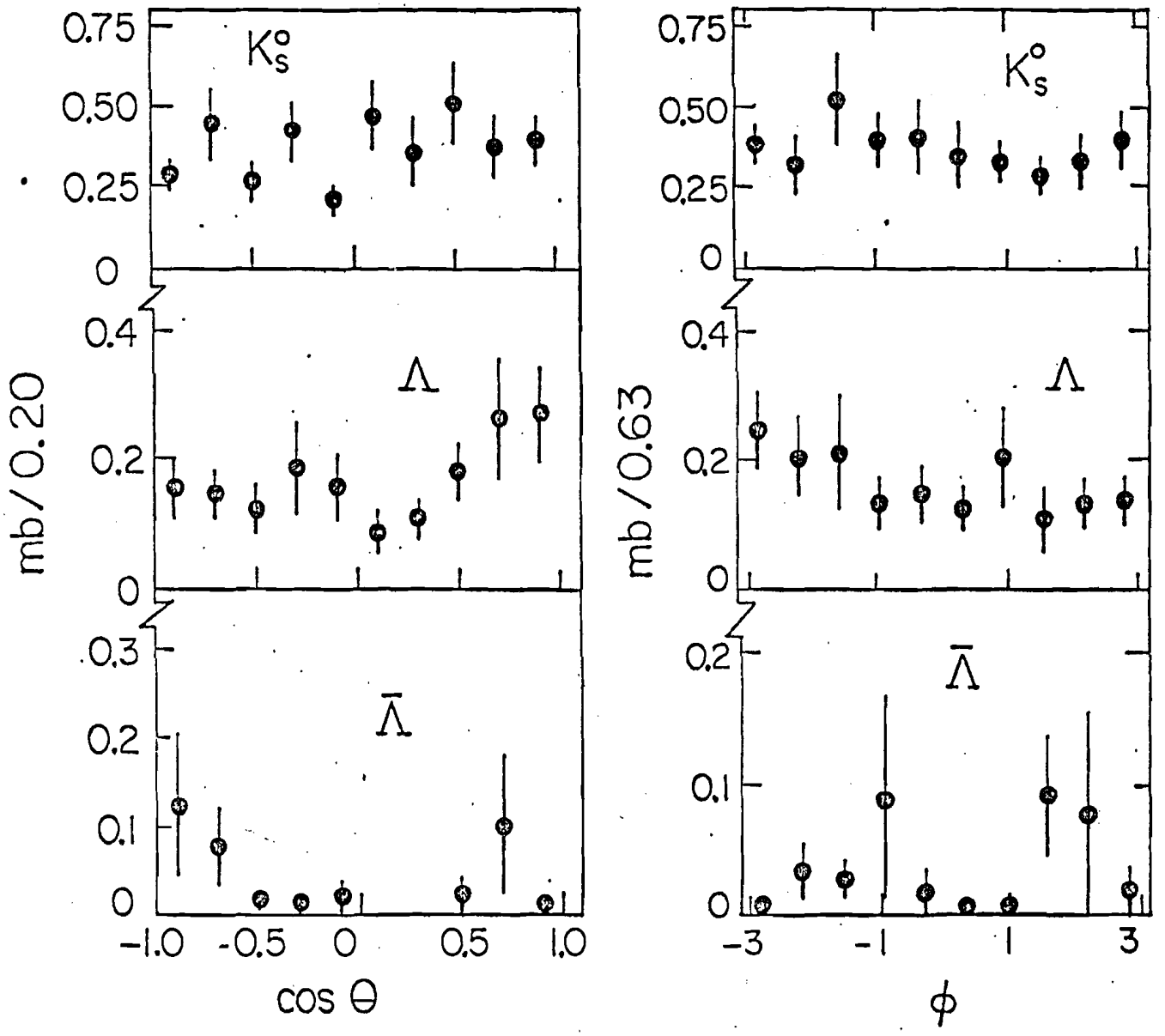

Fig 14. Decay angular distributions

Table 3 Fit losses and misc. unwanted neutrals

	10 roll sample # lost	10 roll sample # remaining	27 roll sample # lost	27 roll sample # remaining
thru GEOMAT	--	793 vrtcs	---	1488 vrtcs
OCQD	37	756	125	1363
non-event[a]	28	728	2	1361
non-pointer[a]	11	717	24	1337
K^- beam[a]	21	696	26	1311
min.p.l.	30	666	81	1230

a: These represent unwanted events, not real losses. They have been excluded without assigning larger weights to the remaining events.

camera axis in the lab. In this coordinate system, all the angular distributions are isotropic; there is no dip at $\phi=\pm\pi/2$ usually associated with scanning losses.

2.8 Decay Volume and Minimum Path Length

If a neutral strange particle decays inside the bubble chamber, all is well and good, we can count it and measure it. But what if it decays outside the chamber? Fortunately, the known statistical nature of the decay process lets us account for the unseen neutral particles.

Suppose at time t=0, a neutral strange particle is produced at $\ell=0$ with mass m and speed v. According to Poisson statistics, the probability that it will decay in the time interval (t,t+dt) is $\frac{1}{T} e^{-t/T} dt$ where T is its lifetime. Therefore the probability that it will decay

within a finite time t or a distance $\ell = vt$ is

$$P(t) = \int_0^t dt' \, \frac{1}{T} \, e^{-t'/T} = 1 - \exp(-t/T)$$

or

$$P(\ell) = 1 - \exp\left(\frac{-m\ell}{p\tau}\right) \qquad (4)$$

where $\tau = T\,(1 - v^2/c^2)^{1/2}$ is its proper lifetime and $p = mv\,(1 - v^2/c^2)^{-1/2}$ is its momentum. We can think of eq 4 as the bubble chamber's efficiency for detecting the decay of a neutral particle with path length up to ℓ. Like all efficiencies, it contributes a weight equal to the inverse of the efficiency.

For the conversion of a gamma ray into an electron-positron pair, we can write down a probability analogous to eq 4: $P(\ell) = 1 - \exp(-\ell\rho\sigma)$ where ρ is the density of nuclei in liquid hydrogen, and σ is the empirically measured cross section for pair production. This expression is like eq 4 except the characteristic decay length $p\tau/m$ is replaced by the radiation length $1/\rho\sigma$. All the constants used in the decay weight calculation are listed in Table 4.

What value of ℓ should we plug into eq 4 to calculate the decay weight? For each neutral particle, we may draw a straight line from the primary vertex, where the neutral is produced, through the secondary vertex, where it decays, until the line intersects the edge of the chamber. The length of this line is the potential path length of the neutral, ℓ; and the actual path length of the neutral, let us call d.

Now $1/P(\ell)$ is <u>not quite</u> the right weight for two reasons.

Table 4 Constants used in decay weight calculations

K_S^o:	$c\tau = 2.66$ cm
$\Lambda, \bar{\Lambda}$:	$c\tau = 7.73$ cm
γ:	$\rho = 4.415 \times 10^{18}$ protons/cm^3 of LH_2
	$\sigma(p \leq 0.01$ Gev/c$) = 2.1$ mb [(a)]
	$\sigma(0.01 < p \leq 0.02) = 5.3$
	$\sigma(0.02 < p \leq 0.03) = 7.1$
	$\sigma(0.03 < p \leq 0.04) = 8.2$
	$\sigma(0.04 < p \leq 0.05) = 9.0$
	$\sigma(0.05 < p \leq 0.06) = 9.6$
	$\sigma(0.06 < p \leq 0.07) = 10.1$
	$\sigma(0.07 < p \leq 0.08) = 10.6$
	$\sigma(0.08 < p \leq 0.09) = 11.0$
	$\sigma(0.09 < p \leq 0.10) = 11.5$
	$\sigma(0.10 < p \leq 0.15) = 12.3$
	$\sigma(0.15 < p \leq 0.20) = 13.7$
	$\sigma(0.20 < p \leq 0.25) = 14.5$
	$\sigma(0.25 < p \leq 0.30) = 15.1$
	$\sigma(0.30 < p \leq 0.35) = 15.7$
	$\sigma(0.35 < p \leq 0.40) = 16.1$
	$\sigma(0.4 < p \leq 0.5) = 16.6$
	$\sigma(0.5 < p \leq 0.6) = 17.1$
	$\sigma(0.6 < p \leq 0.7) = 17.5$
	$\sigma(0.7 < p \leq 0.8) = 17.8$
	$\sigma(0.8 < p \leq 0.9) = 18.0$
	$\sigma(0.9 < p \leq 1.0) = 18.2$
	$\sigma(1.0 < p \leq 1.2) = 18.4$
	$\sigma(1.2 < p \leq 1.4) = 18.7$
	$\sigma(1.4 < p \leq 1.6) = 18.9$
	$\sigma(1.6 < p \leq 1.8) = 19.1$
	$\sigma(1.8 < p \leq 2.0) = 19.3$
	$\sigma(2.0 < p \leq 3.0) = 19.5$
	$\sigma(3.0 < p \leq 4.0) = 19.8$
	$\sigma(4.0 < p \leq 5.0) = 20.0$
	$\sigma(5.0 < p \leq 6.0) = 20.1$
	$\sigma(6.0 < p \leq 7.0) = 20.2$
	$\sigma(7.0 < p \leq 8.0) = 20.2$
	$\sigma(8.0 < p \leq 9.0) = 20.3$
	$\sigma(9.0 < p) = 20.33$

(a): γ conversion cross-sections taken from ref. [11].

First, when d is near ℓ, i.e. when the neutral decays near the edge of the chamber, the length of the tracks of its decay products are very short and consequently difficult to measure, reconstruct, and fit. Second, when d is near zero, i.e. when the neutral decays near the production vertex, the V^o signature is hard to pick up during scanning because the decay products look like charged particles produced at the primary vertex. In other word, eq 4 is accurate only for intermediate values of d. For d near zero or ℓ the actual probability of detecting a neutral decay is less than $P(\ell)$.

Therefore we define a decay volume with the intention of throwing away (assigning zero weight to) those neutrals whose decay vertices do not lie within the volume. the specification of the decay volume, given in Table 5, has two parts. First, the neutral decay vertex must be inside a rectangular box. This box is sufficiently inside the physical edges of the chamber so that for the majority of the neutral decays inside the box, more than 10 cm of tracks of the decay products are visible in all three views. In addition, the decay vertex must be at least a distance ℓ_{min} away from the primary vertex. The probability then of observing a neutral decay whose vertex lies inside the decay volume is

$$P(\ell_{min},\ell_{pot}) = \exp(-m\ell_{min}/p\tau) - \exp(-m\ell_{pot}/p\tau) \qquad (5)$$

where ℓ_{pot} is the length of the portion of the potential path of the neutral that is inside the box. A neutral that

Table 5 Decay volume parameters

surfaces of box are:	x = -28.0 cm
	x = 25.0 cm
	y = -21.0 cm
	y = 21.0 cm
	z = -37.0 cm
	z = 0.0 cm
ℓ_{min} = 2.0 cm	

decays inside the decay volume has a weight $1/P(\ell_{min},\ell_{pot})$. A neutral that decays outside the decay volume has a weight of zero.

We want to keep the decay volume as large as possible to maximize the total number of neutrals in the sample. Starting with a small decay volume, as we gradually increase the decay volume, either by decreasing ℓ_{min} or by enlarging the size of the box which has the effect of increasing ℓ_{pot}, the sum of the decay weights should remain constant. We add more neutrals to our sample but the weight of each neutral is smaller. Figure 15 shows how the sum of the decay weights vary as a function of ℓ_{min} with the box fixed as given in Table 5. There are substantial losses for $\ell_{min} < 2$ mm; we chose $\ell_{min} = 2$ cm.

For the box, the situation is slightly more complicated. Among the six surfaces of the box, the front surface defined by x = 25 cm, whose outward normal is parallel to the beam direction, is the most important. For more than 90% of the neutrals, the potential path intersects this front surface,

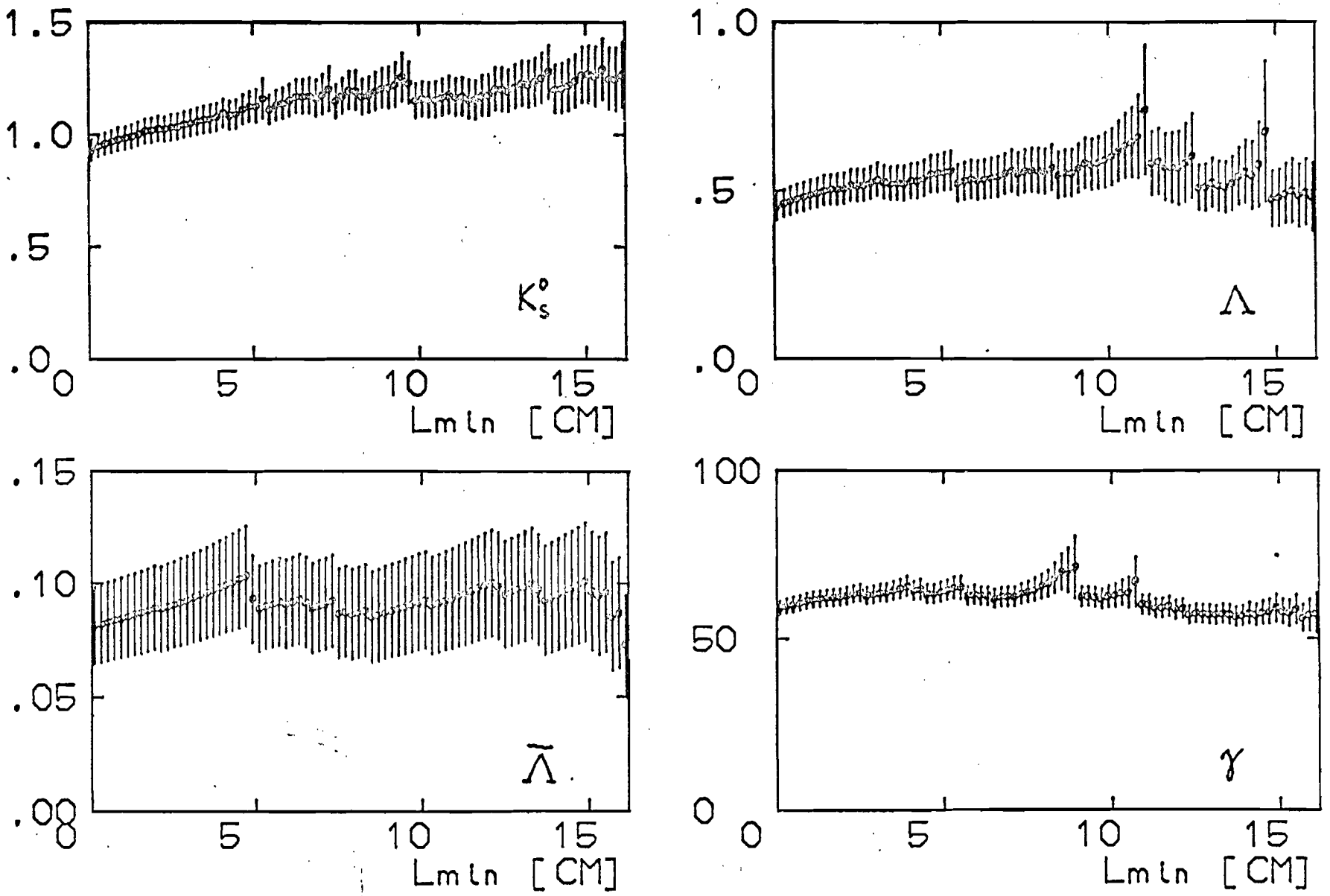

Fig 15. Sum of decay weights vs ℓ_{min}

and the decay products have a minimum track length of 10 cm. However, for a few neutrals whose potential path intersects the box at the five other surfaces, no such minimum track length is guaranteed because z = 0 and z = -37 cm actually are the physical edges of the chamber. In fact, some corners of the box are not visible in all three views.

In Table 6, the sums of the decay weights are given for two different choices of box-size with ℓ_{min} fixed at 2 cm. All surfaces of the smaller box are visible in all three views. Since the values in the two columns are equal within errors, we conclude that even though there are some neutrals produced at large angles whose decay weights are underestimated by our choice of box-dimensions, the losses are not significant.

2.9 Re-measurements and Measuring Weights

We define a neutral as successfully measured if it yields at least one fit that passes physicist inspection. In the 10 roll sample, events containing one or more neutrals in the region $x \leq 25$ cm that were not successfully measured on the first pass were re-IPD'ed and re-PEPR'ed for a second time. From the entries in Tables 2 and 3, the overall measuring efficiency for neutrals is 90.1% on the 10 rolls and 80.4% on the 27 rolls.

We now want to assign measuring weights to account for the measuring inefficiencies. The situation here is very similar to the one encountered in secton 2.4. There are two

Table 6 Sum of decay weights as a function of box size

	big box $-28 \leq x \leq 25$ cm $-21 \leq y \leq 21$ cm $-37 \leq z \leq 0$ cm	small box $-28 \leq x \leq 20$ cm $-12 \leq y \leq 15$ cm $-32 \leq z \leq -5$ cm
K_s^o	1024.7±54.1	982.8±62.6
Λ	504.8±45.9	486.3±50.6
$\bar{\Lambda}$	88.70±18.67	108.2±26.6
γ	62664±2363	59556±2759

samples of events. The singly-measured portion of the film corresponds to a fraction F of the total incident beam flux; the doubly-measured portion of the film contains 1-F of the total beam flux. The procedure used to assign the measuring weights is roughly as follows: We first tag those successfully measured events in the 10 roll sample that failed on the first pass as 2nd-pass-only. In order to minimize the biases in the re-measured events, we do not use a uniform weight. Instead, events that are not 2nd-pass-only receive a weight of 1.0; 2nd-pass-only events receive a weight $\frac{1}{1-F}$ divided by the measuring efficiency of the 2nd pass. Note that the technique of using the beam flux factor $\frac{1}{1-F}$ in the weights is identical to the weighting scheme for scan losses. The details are given below.

2.9.1 Factoring out the Event Weight

Instead of regarding the measuring weight for neutrals as a single number which is the inverse of the probability of successfully measuring a neutral, we like to think of it as

a product of two weights, the event weight, which is the inverse of the probability of successfully measuring an event whether it contained neutrals or not, and the neutral weight, which is the inverse of the probability of successfully measuring a neutral given the event was measured successfully. Thus in Tables 2 and 3, the categories "tape errors" and "rejects" would contribute to the event weight, "no vertex", "no tracks", and "OCQD" would contribute to the neutral weight. If we were interested only in processes that include a single neutral, then the separation is not a very useful one since the event weight and the neutral weight must always be multiplied together in pairs. However, factoring out the event weight is essential for calculating cross-sections involving two neutrals or one neutral and a charged particle.

2.9.2 Scan-2 only Neutrals

The neutral weight for Scan-2 only neutrals is tabulated directly by counting the number of successfully measured neutrals in this category regardless of how they got there (on the first measurement pass or on the re-measurement pass). It is listed in Table 7. These Scan-2 only neutrals already have a factor of $\frac{1}{1-F}$ in their scan weights. By treating them separately, we make sure no neutral is ever weighted by two factors of $\frac{1}{1-F}$.

2.9.3 2nd-pass-only Neutrals

After the Scan-2 only neutrals have been removed from the

Table 7 Neutral weights

Scan-2 only 10 rolls	V:	1.100	$\frac{1}{1-F}$
	straight γ:	1.051	
	curly γ:	1.131	
2nd-pass-only 10 rolls	V:	1.109	$\frac{1}{1-F}$
	straight γ:	1.109	
	curly γ:	1.274	
not 2nd-pass-only not Scan-2 only 10 rolls		1.000	
27 rolls		0.8249	

10 roll sample, the remaining events were separated into two groups. Events that failed on the first measurement pass were tagged as 2nd-pass-only. They are weighted by the measuring efficiency on the 2nd pass and also the beam flux factor $\frac{1}{1-F}$. These neutral weights are also given in Table 7.

2.9.4 Consistency with Flux Factor

The rest of the events, consisting of 437 neutrals from the 10 roll sample that were not tagged 2nd-pass-only, and 1363 neutrals from the 27 roll sample, should be given a neutral weight of 1. And, as a consistency check, the ratio of the number of neutrals in the two samples should agree with the ratio of beam fluxes. But

$$\frac{1363}{437} = 3.119 \neq \frac{F}{1-F} = 2.588$$

The source of the discrepancy was the result of a mistake in the re-measurement effort. After the re-measurement list was created, i.e. after the 2nd-pass-only events were tagged, we fixed a problem in GEOMAT (point match ambiguity) which was an important reason for events failing. All the events were

then re-processed but it was impossible to adjust the 2nd-pass-only tags accordingly. We did not want to throw away the extra neutrals in the 27 roll sample; to avoid double counting, we assigned a neutral weight of 0.8249 to all 1363 neutrals in the 27 roll sample. The 437 neutrals in the 10 roll sample were given a neutral weight of 1.

The reduced weight 0.8249 may be derived in two equivalent ways. Given 437 neutrals in the 10 roll sample, from beam flux ratios, we expect 437 ($\frac{F}{1-F}$) = 1130.9 neutrals in the 27 roll sample instead of 1363. Therefore they should be weighted by $\frac{1130.9}{1363}$ =0.8298. The second technique, which is the one we actually used, is to calculate the inclusive K_S^o cross-section from the 10 roll sample alone, and then adjust the weights of the neutrals in the 27 roll sample until the 37-roll cross-section agrees with the 10-roll cross section.

3.1 Single Particle Inclusive Distributions

The total inclusive neutral cross sections are listed below.

Table 8. Total Inclusive Neutral Cross Sections

	# of neutrals	cross section in mb
K_s^o	505	3.67 ± 0.38
Λ	238	1.65 ± 0.21
$\bar{\Lambda}$	32	0.38 ± 0.13
γ	1121	129. ± 10.6

Assuming all the γ's orginate from π^o decay, $\sigma(\pi^o)=\sigma(\gamma)/2$. In calculating these cross sections, we have corrected for the neutral decay modes of the strange particles in addition to the corrections due to detection, scanning, measuring, and fitting losses mentioned in Chap. 2. The μb/event values used for these cross sections have been previously determined [12]. Systematic errors, which have been included, are estimated to be 6% for K_s^o, Λ, γ, and 16% for $\bar{\Lambda}$ [13].

The inclusive π^o cross section is roughly half the inclusive charged particle cross section ($\langle n_{ch}\rangle\sigma_{inel}$ = 7.40 x 21.0 mb = 155.4 mb); the strange particle cross sections are one to two orders of magnitude smaller.

The transverse momentum squared distributions $d\sigma/dp_t^2$ for the neutrals, shown in Figs. 16 and 17, are sharply cut off

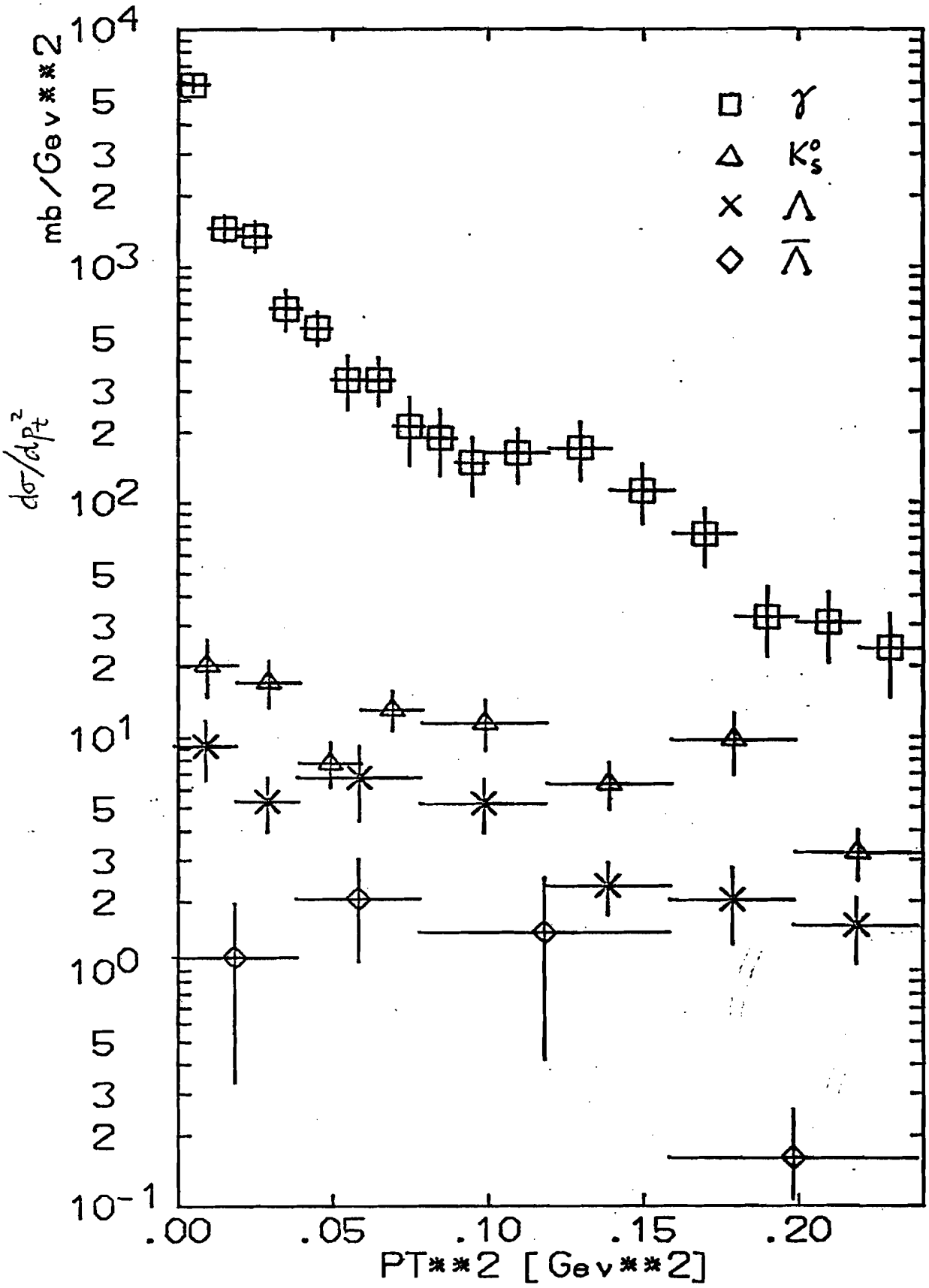

Fig 16. Transverse momentum distributions for neutrals

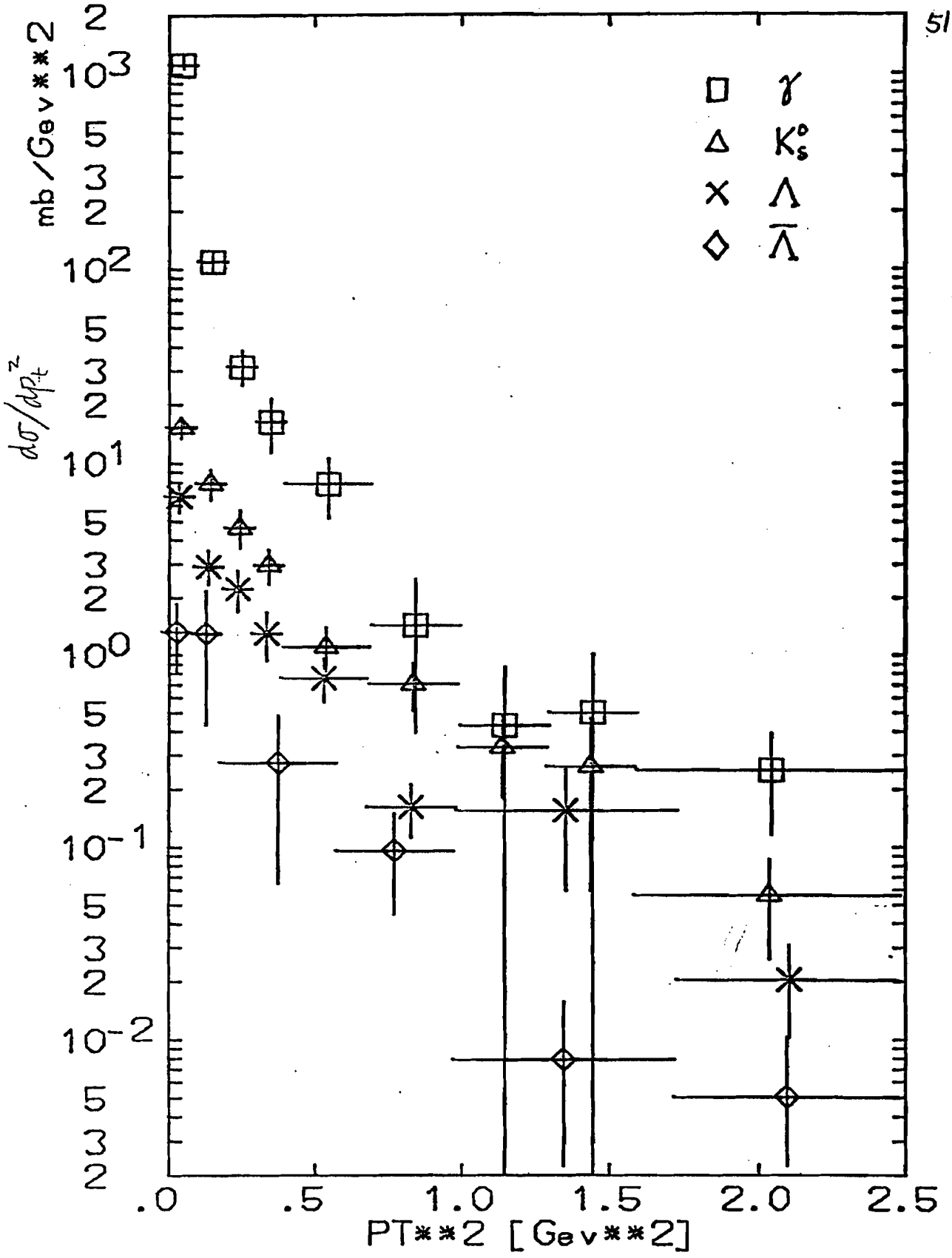

Fig 17. Transverse momentum distributions for neutrals

just as the charged particles are. At small p_t^2, the γ distribution falls faster than the strange-particles which are not noticeably different from each other. At large p_t^2, all the distributions level off and are decreasing at about the same rate from 0.5 to 2.5 Gev^2.

The profiles of $\langle p_t^2 \rangle$ vs. the longitudinal variables

$$x = 2p_L^*/\sqrt{s} \text{ and}$$

$$y = \frac{1}{2}\log((E^*+p_L^*)/(E^*-p_L^*))$$

are shown in Figs. 18 and 19. The distributions for γ and K_s^o are very similar to that of the π^+ distribution shown in Figs. 20 and 21 which show a dip at x=0 and constant $\langle p_t^2 \rangle$ vs. y except for y near y_{min} and y_{max}. These features are not apparent in the Λ and $\bar{\Lambda}$ distributions probably because of the limited statistics.

The longitudinal distributions for charged particle production show a variety of behavior depending on the incident beam and the type of particle produced. The neutral distributions $\frac{d\sigma}{dx}$, $\frac{2E}{\pi\sqrt{s}}\frac{d\sigma}{dx}$, and $\frac{d\sigma}{dy}$, shown in Figs. 22, 23, and 24 may be divided in two groups -- γ, K_s^o, $\bar{\Lambda}$ which are centrally produced, and Λ which are produced predominantly in the backward hemisphere. The $\frac{d\sigma}{dx}$ distributions for γ, K_s^o, and $\bar{\Lambda}$ show a large peak at x=0 with approximate forward-backward symmetry which is also characteristic of π^+ production shown in Figs. 25-27 [14]. However, the widths of the peaks are not all identical. From Table 9, we see that $x_{RMS}^2 = \langle (x - x_{min})^2 \rangle$ for γ's is smaller than the $\pi^\pm$ values

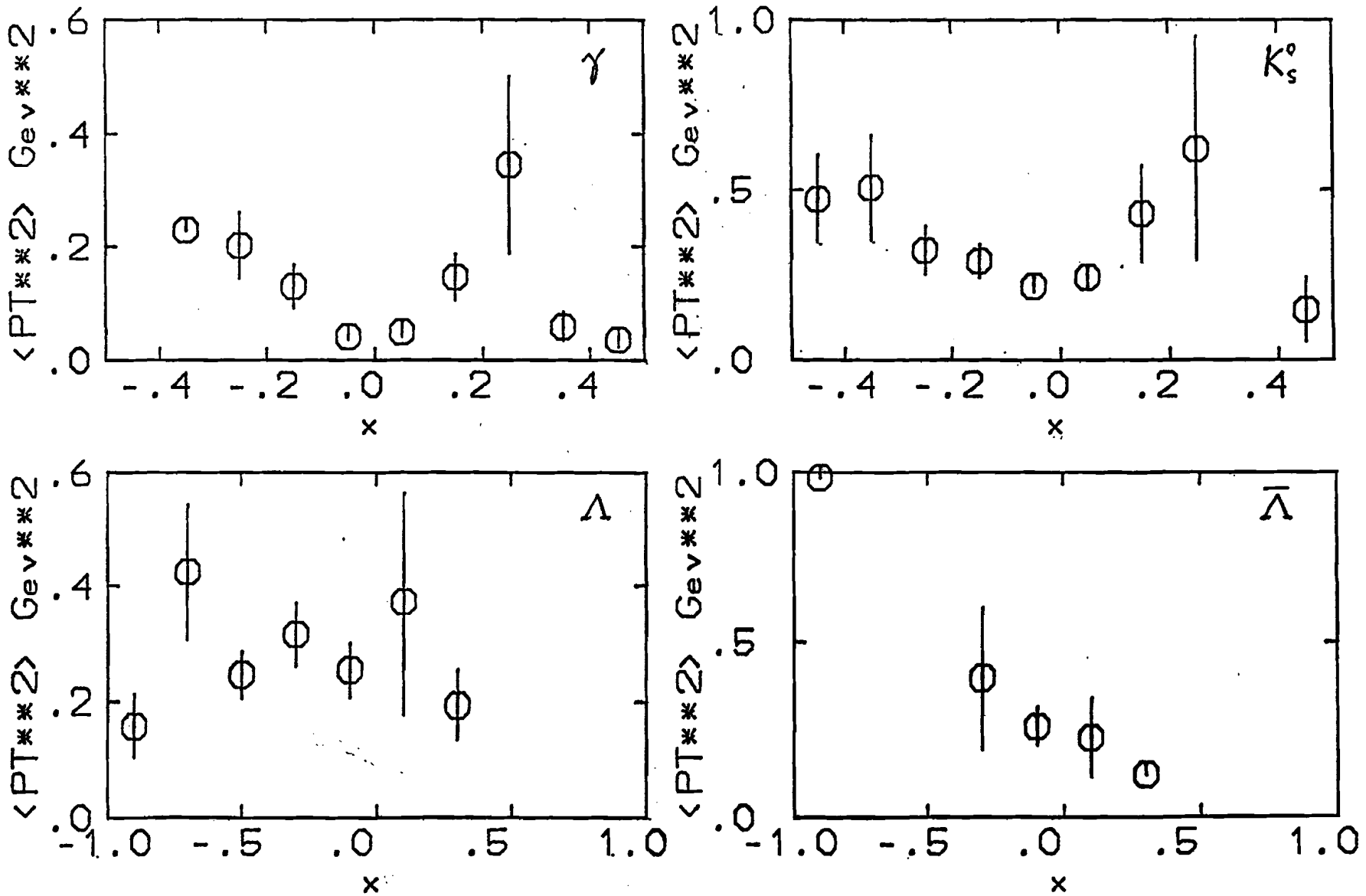

Fig 18. Neutral $\langle p_t^2 \rangle$ vs x

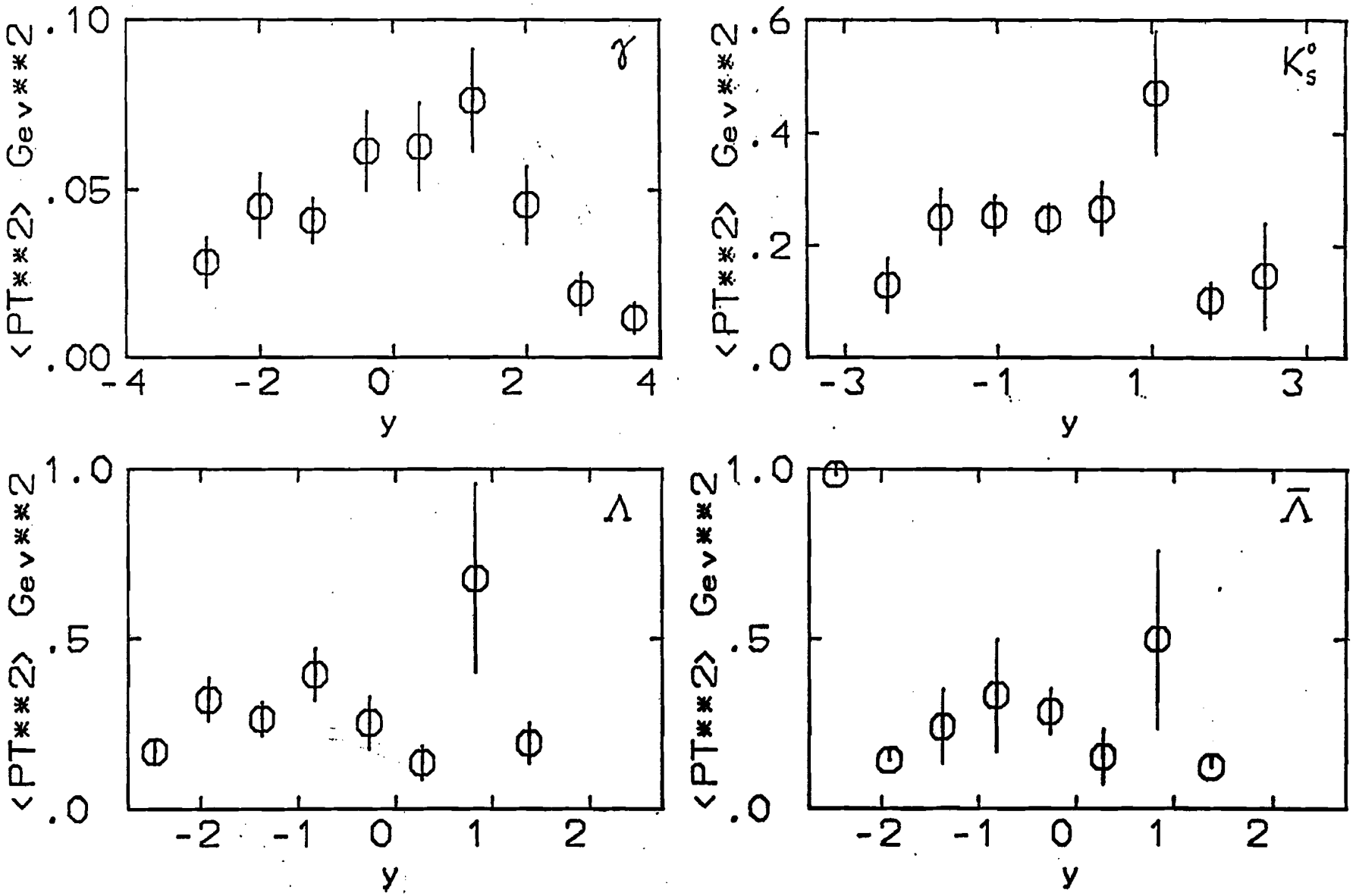

Fig 19. Neutral $\langle p_t^2 \rangle$ vs y

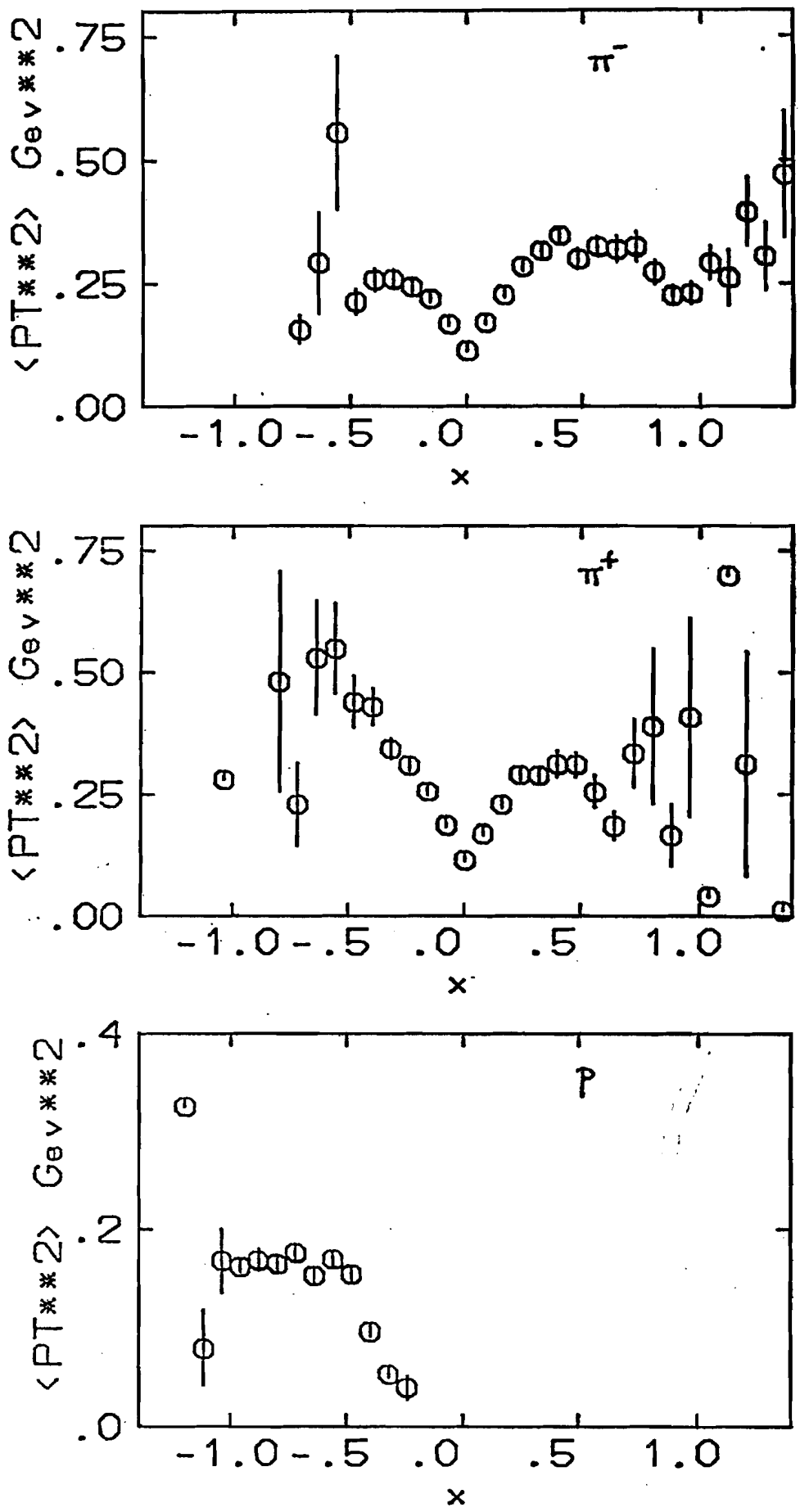

Fig 20. Charged particle $\langle p_t^2 \rangle$ vs x

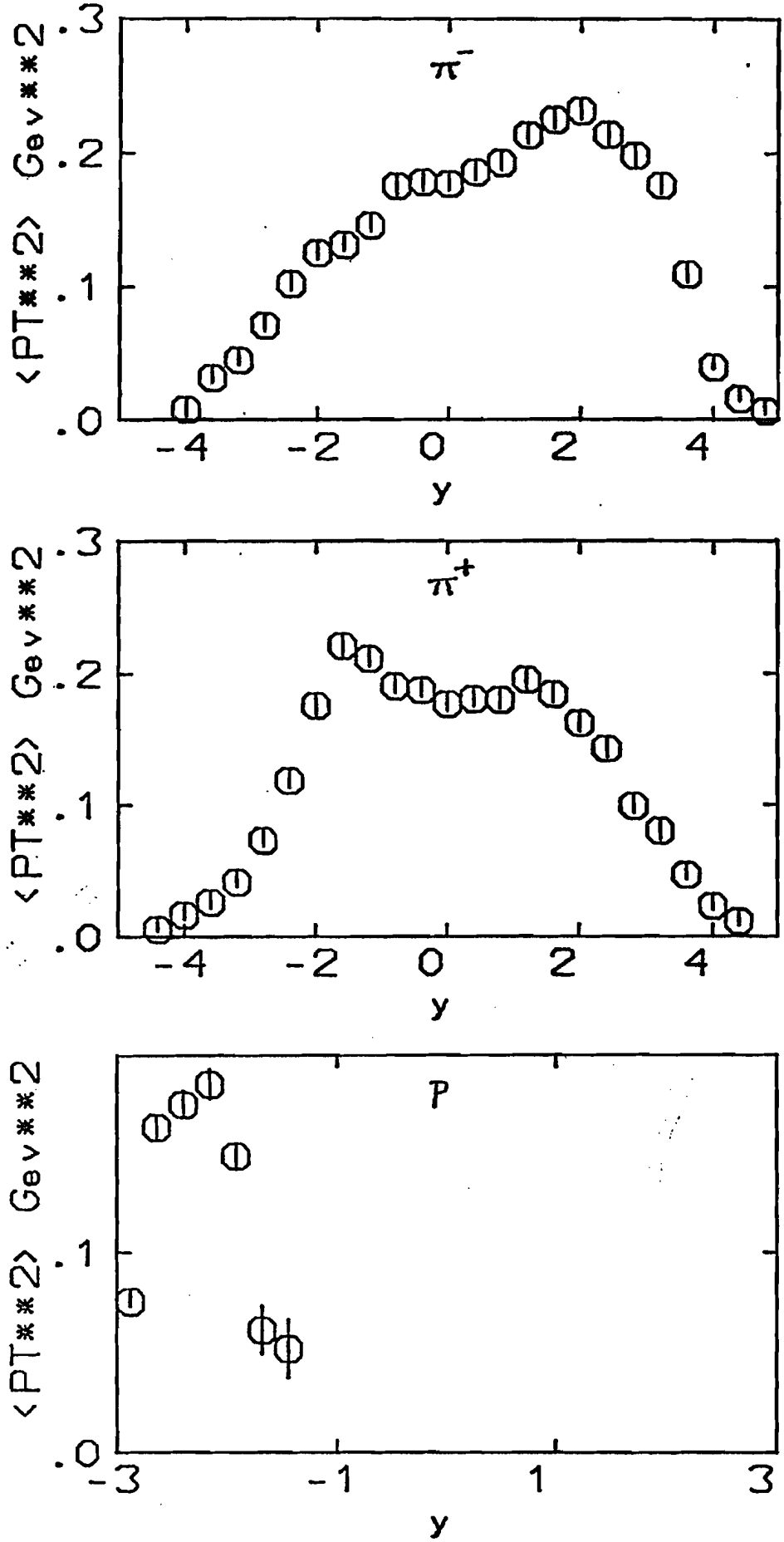

Fig 21. Charged particle $\langle p_t^2 \rangle$ vs y

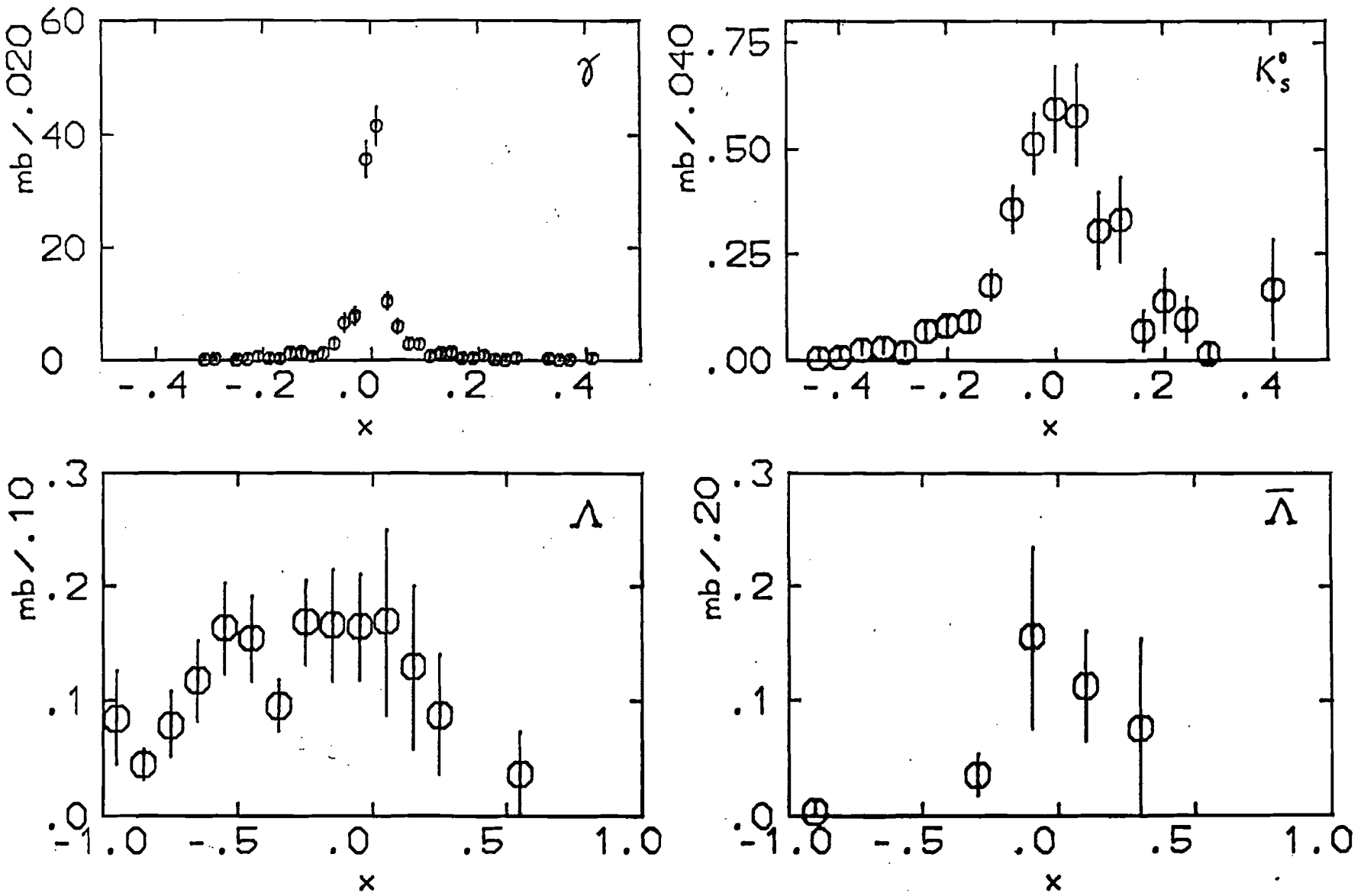

Fig 22. Neutral $d\sigma/dx$

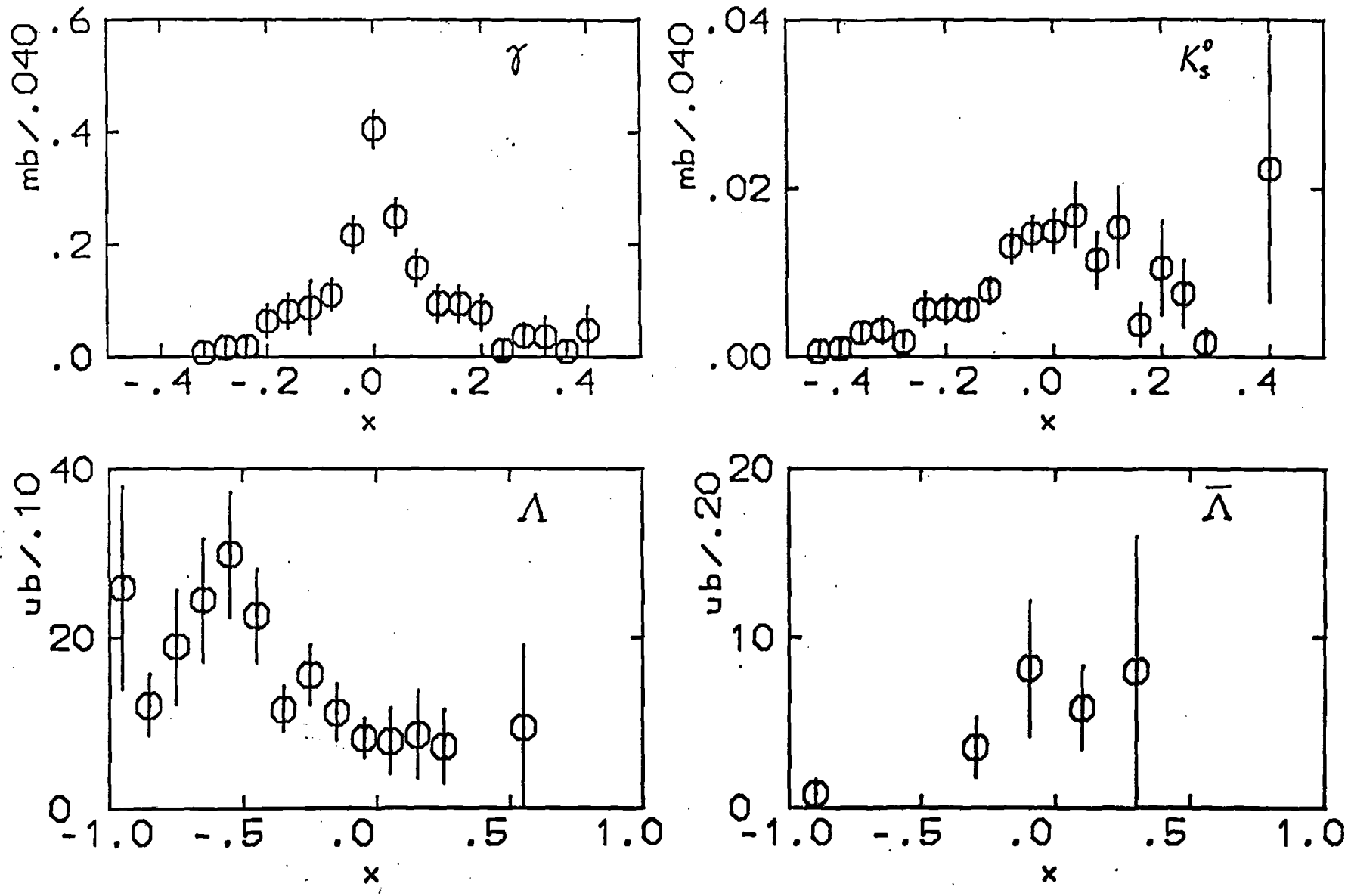

Fig 23. Neutral $(2E/\pi\sqrt{s})\ d\sigma/dx$

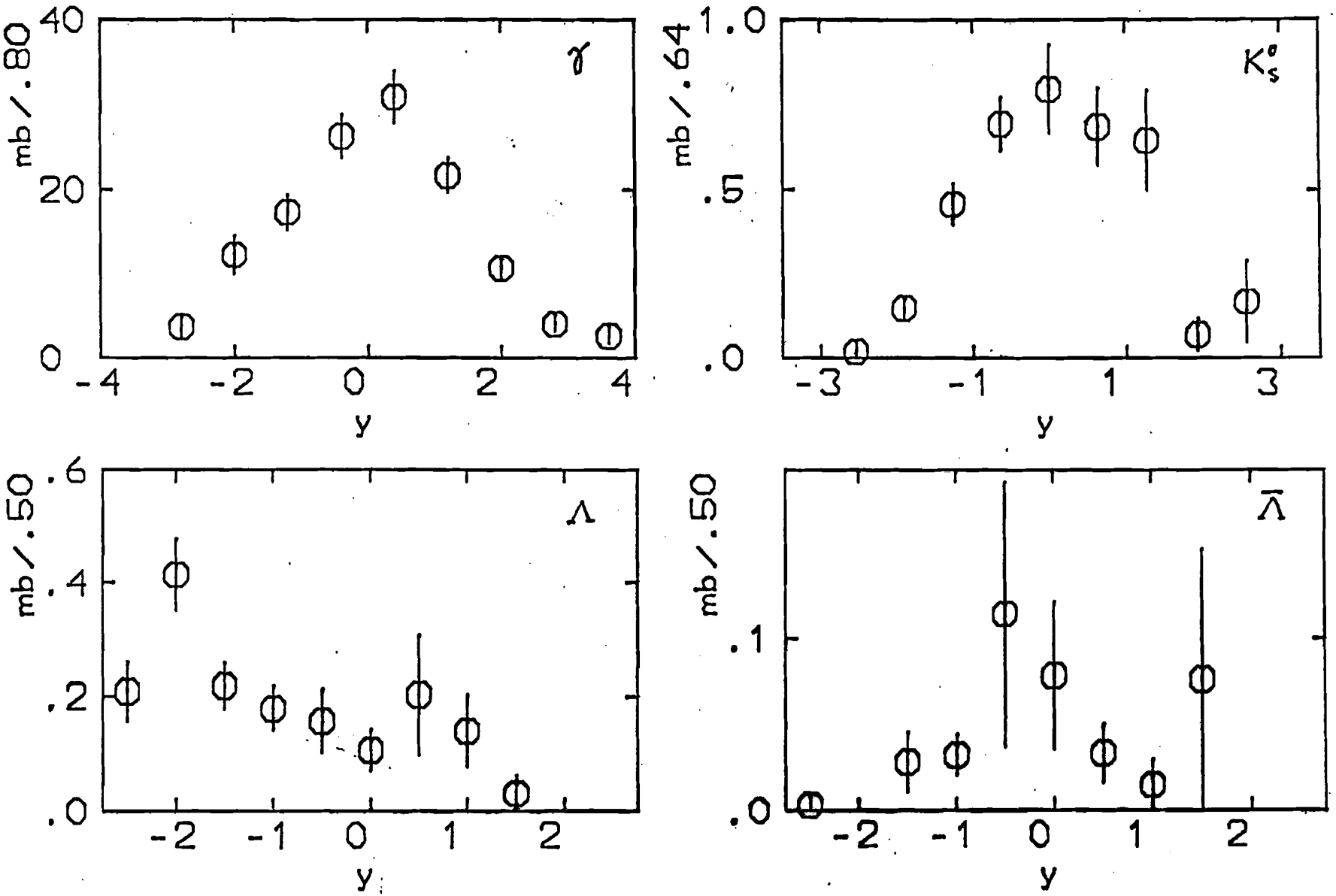

Fig 24. Neutral $d\sigma/dy$

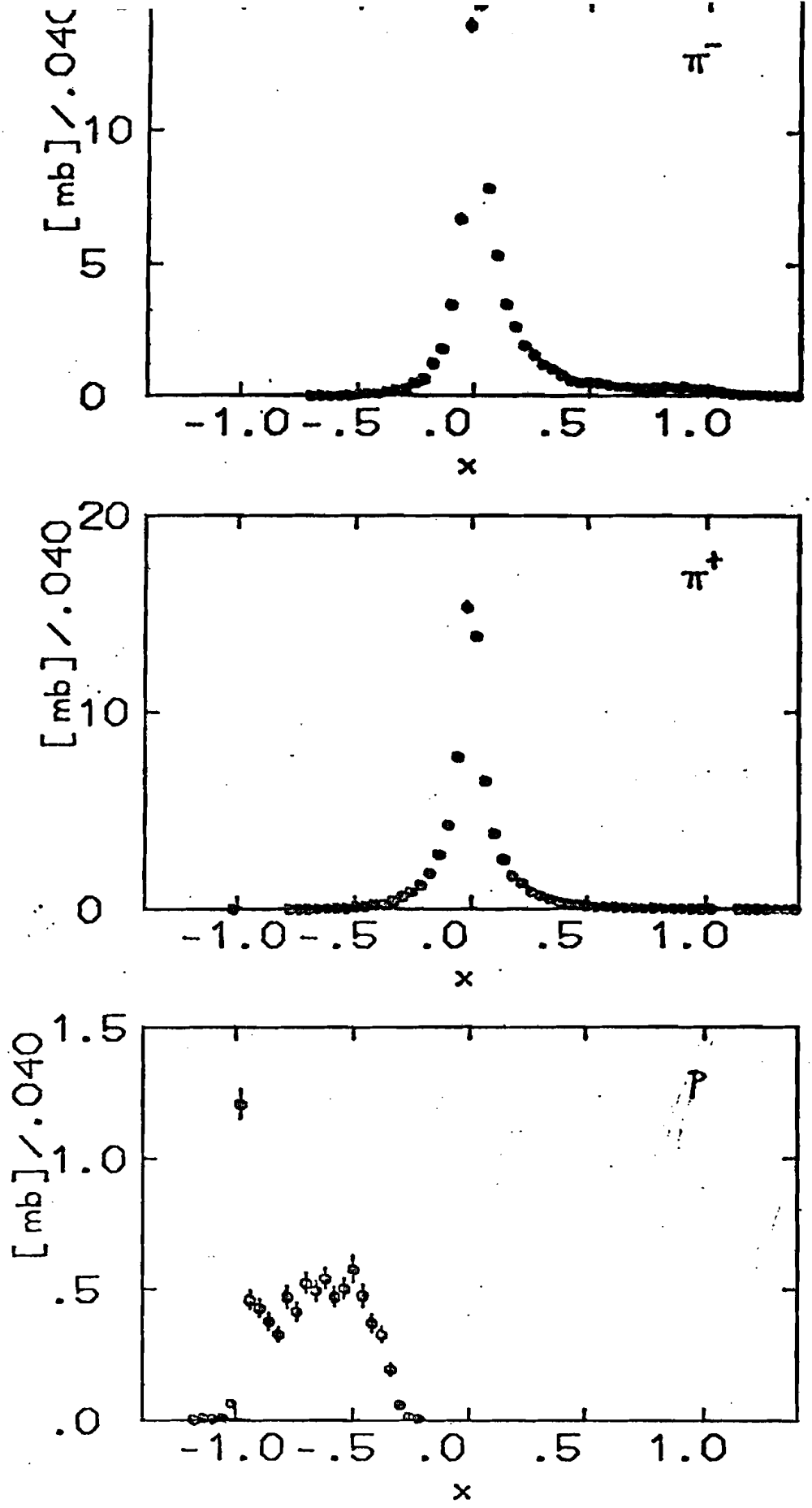

Fig 25. Charged particle $d\sigma/dx$

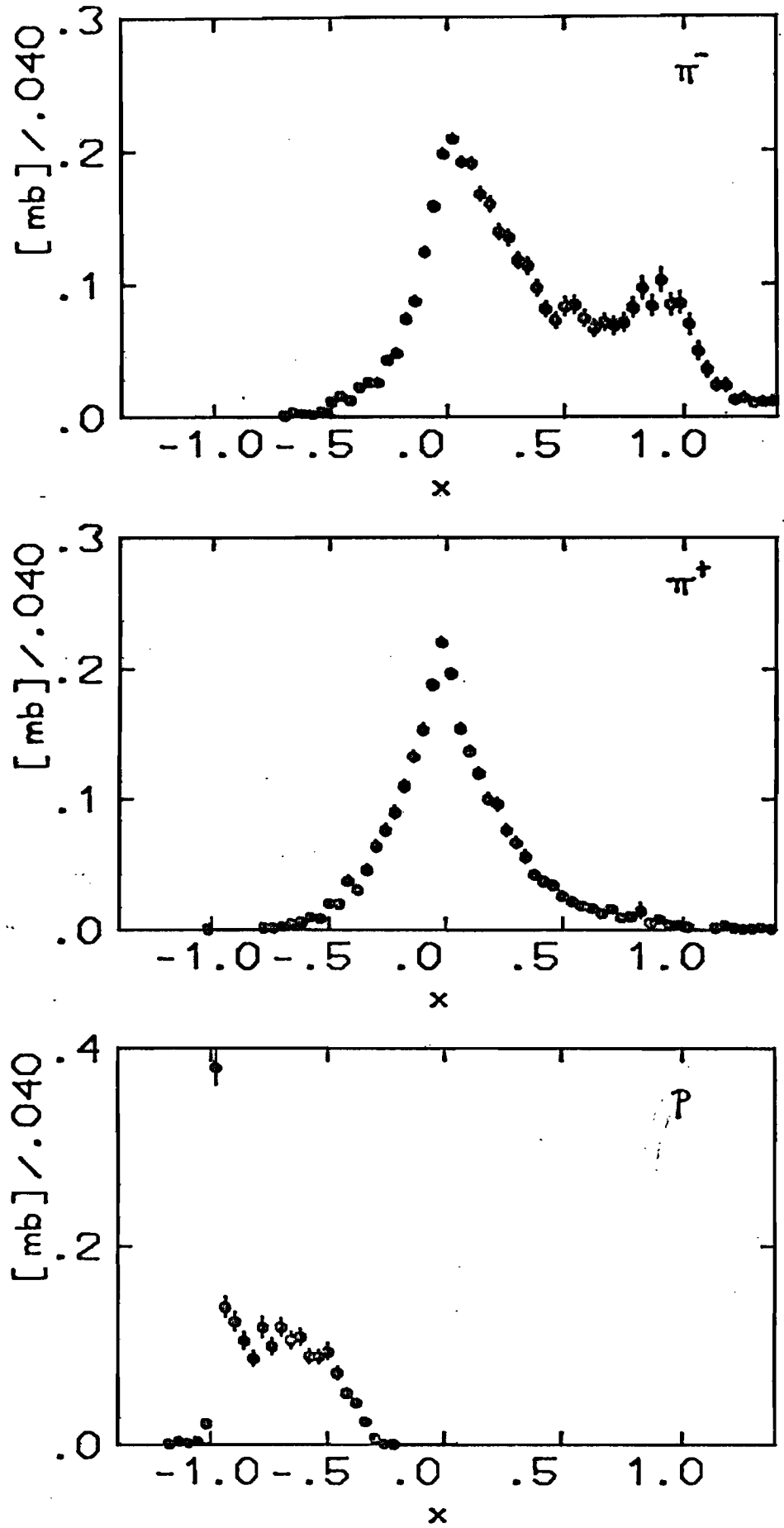

Fig 26. Charged particle $(2E/\pi\sqrt{s})\ d\sigma/dx$

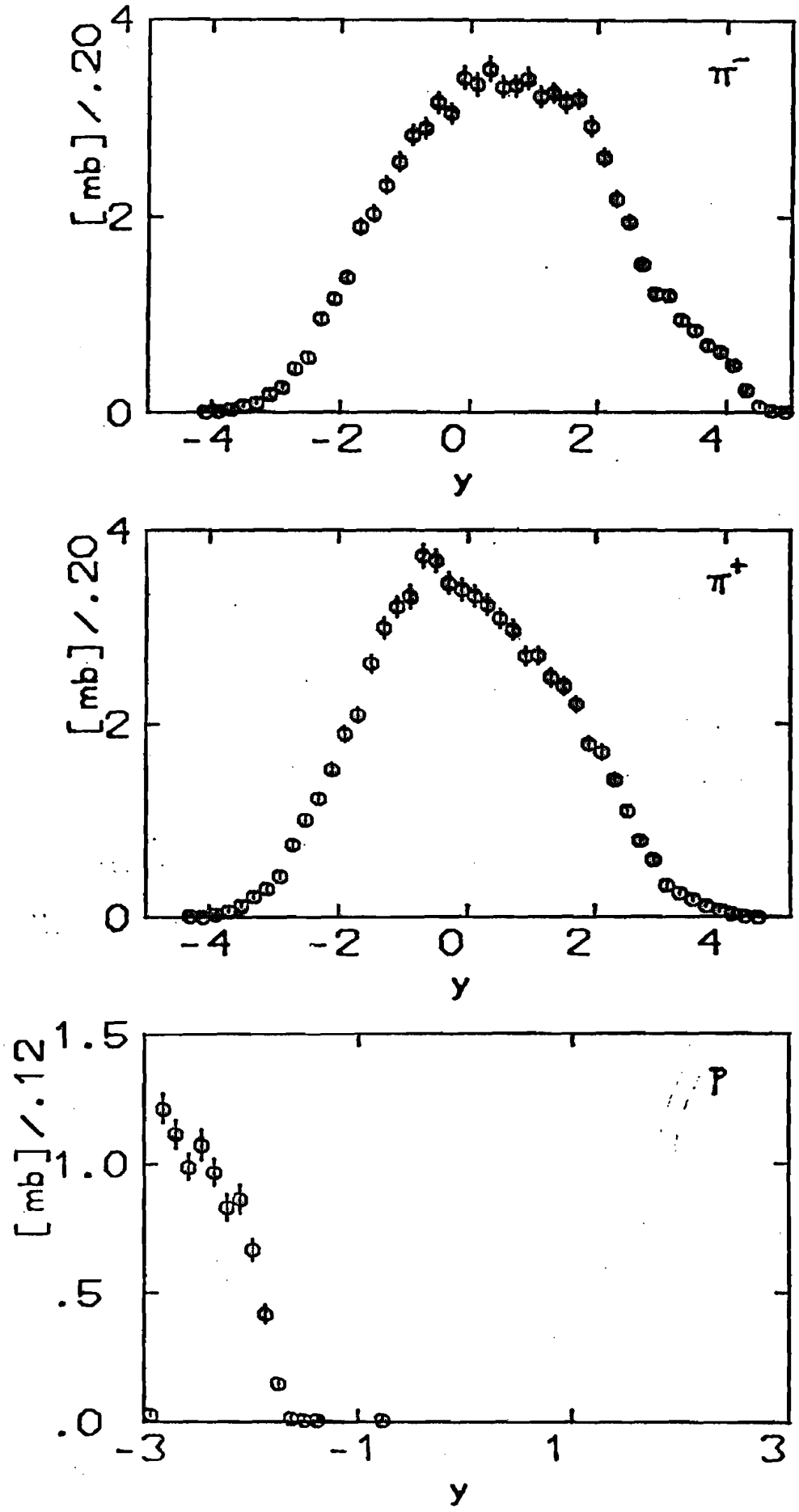

Fig 27. Charged particle $d\sigma/dy$

Table 9 Moments of $d\sigma/dx$ distributions

particle	x_{mean}	x_{RMS}
γ	.004	.064
K_s^o	.021	.141
$\bar{\Lambda}$	.018	.187
π^+	.004	.151
π^-	.085	.234

and the width of the K_s^o, $\bar{\Lambda}$ distributions are comparable to that of the π^+.

The height of the central peak, measured by $\frac{d\sigma}{dy}$ at y=0 is (1.36±0.23) mb for K_s^o and (33.5±1.4) mb for the charged particles. ∴ the K_s^o/charged ratio is $\frac{1.36}{33.5}$ = (4.06±0.71)%. This value is somewhat larger than the overall K_s^o/charged ratio

$$\frac{\sigma(K_s^o)}{\sigma(\text{charged})} = \frac{3.672}{155.4} = (2.36\pm0.18)\%$$

because the $d\sigma/dy$ distributions for charged particles and K_s^o do not have the same shape. At 147 Gev/c, a sizable fraction of the charged particles comes from the fragmentation regions. However, as the c.m. energy increases, we would expect the overall K_s^o/charged ratio to increase and asymptotically approach the K_s^o/charged ratio in the central region.

Λ production resembles proton production. A significant fraction of the Λ's come from the region $-1 \leq x \leq -0.4$; there

is no peak at x=0.

3.2 Beam Particle and Energy Dependence

The total inclusive neutral cross sections for a number of experiments [15-28] are shown in Fig. 28 and the average number of neutrals per inelastic collision, defined by

$$\langle n_o \rangle = \frac{\sigma(0)}{\sigma_{inel}}$$

where $\sigma(0)$ is the inclusive neutral cross section, are plotted in Fig. 29. For the centrally produced neutrals π^o, K_s^o, and $\bar{\Lambda}$, the inclusive cross sections from pp data are larger than cross sections from $\pi^- p$ data by just the ratio of the total inelastic cross sections so that $\langle n_o \rangle$ for $\pi^- p$ and pp experiments more or less fall on the same curves which are rising slowly with energy.

For charged particles, which are not solely produced in the central region, it is well known that dividing the inclusive cross sections by the inelastic cross sections does not completely take out the beam dependence. Fig. 30, from a compilation by Stix and Ferbel [29], shows $\langle n_c \rangle_{\pi p}$ is systematically larger than $\langle n_c \rangle_{pp}$, but the difference decreases as s increases. In π^o, K_s^o, and $\bar{\Lambda}$ production, although the experiments are less accurate, there is no difference between $\langle n_o \rangle$ in πp and pp collisions.

For Λ's, if we average the cross sections from 4 pp and 5 $\pi^- p$ experiments above 50 Gev/c (see Fig. 28), the beam dependence is most simply described by

$$\frac{\sigma(pp \rightarrow \Lambda)}{\sigma(\pi p \rightarrow \Lambda)} \sim \frac{3.44 \pm 0.20}{1.59 \pm 0.11} = 2.17 \pm 0.19 \qquad (6)$$

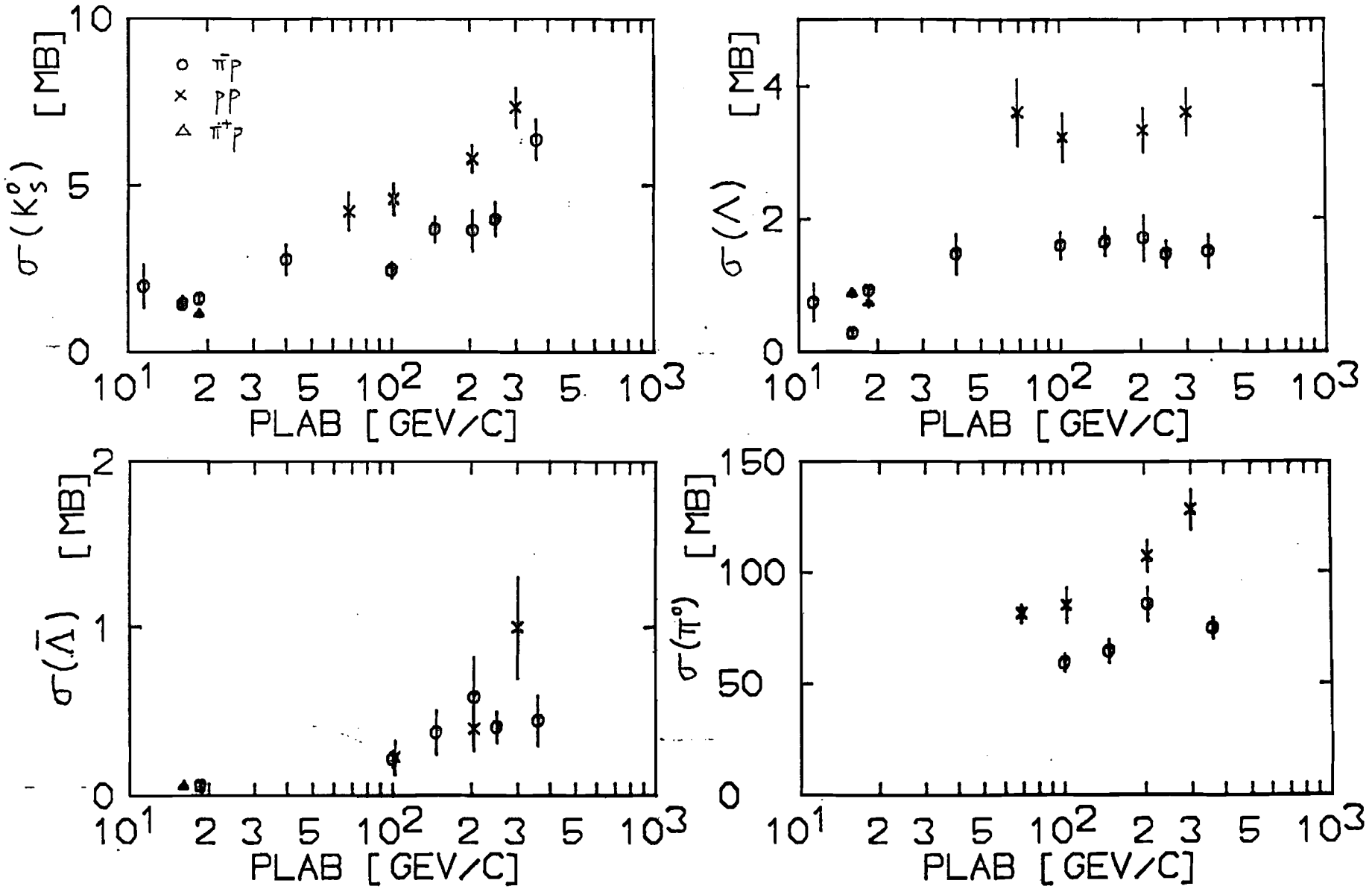

Fig 28. Neutral cross sections vs energy

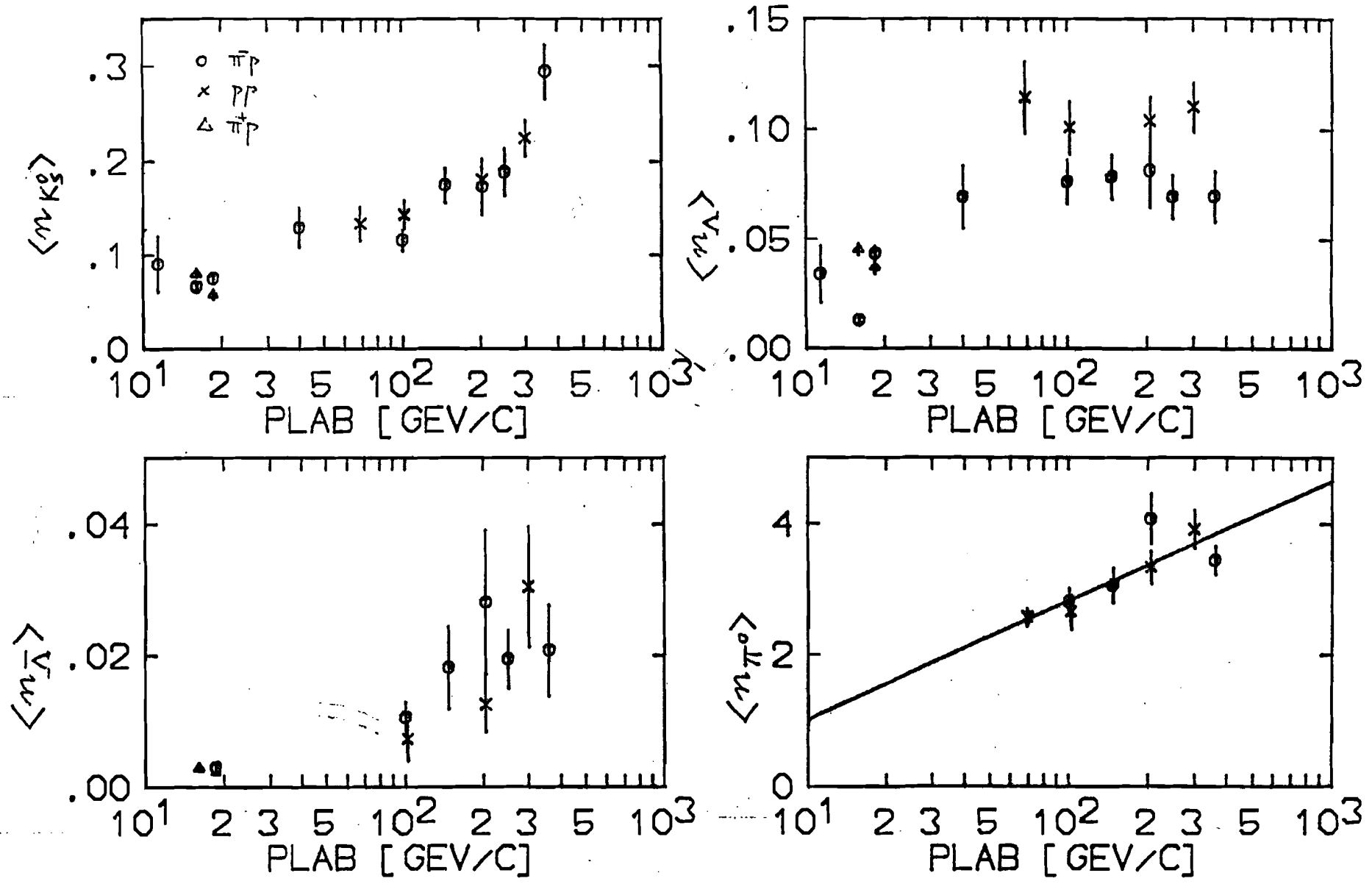

Fig 29. Neutral multiplicity vs energy

Fig 30. Beam and energy dependence of $\langle n_c \rangle$, from Ref.[29]

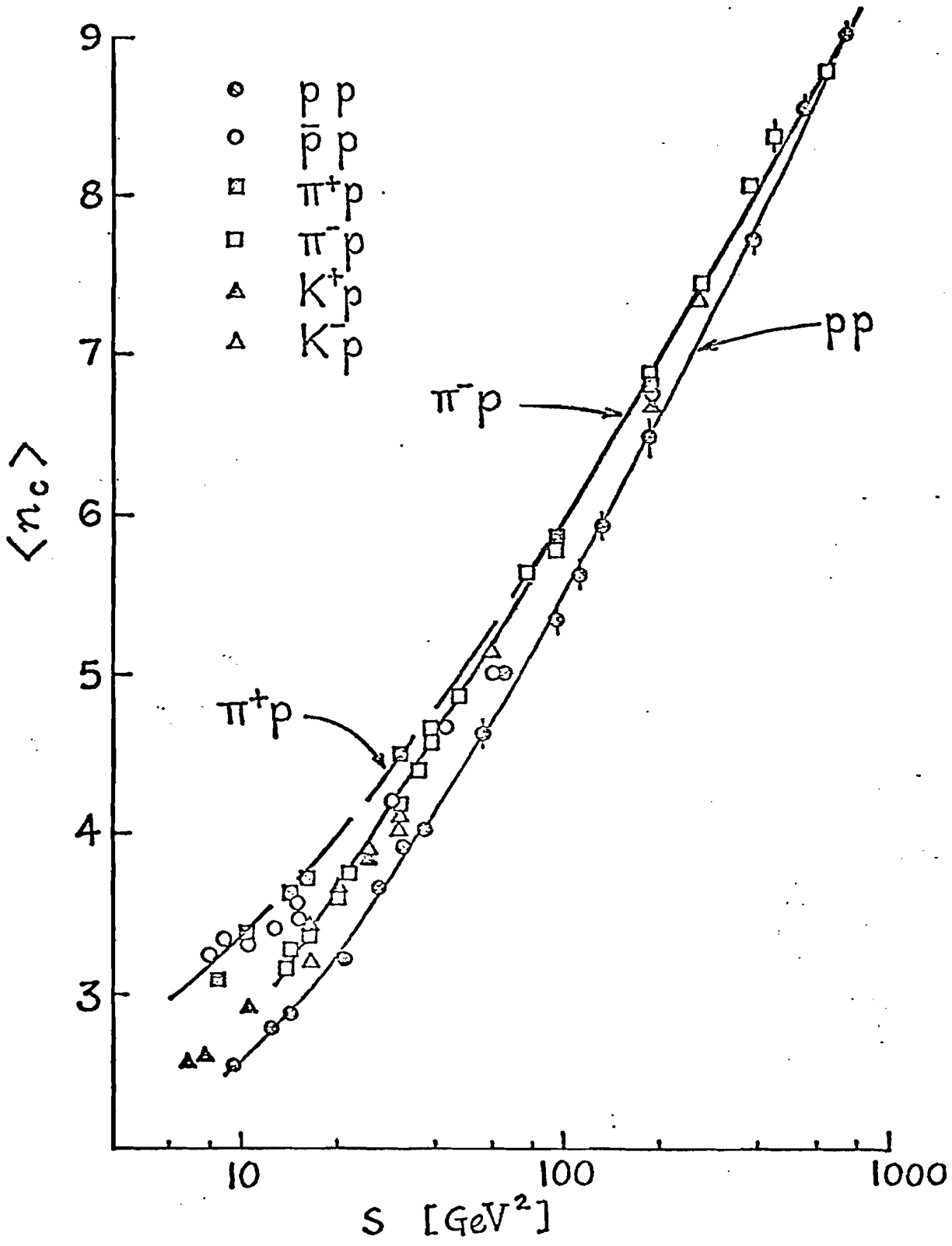

Since the ratio of pp to πp inelastic cross sections is more like $\frac{3}{2}$, $\langle n_\Lambda \rangle$ is <u>not</u> beam independent.

At very large s, the allowed range of rapidity y grows like log (s/m^2). If the invariant single particle inclusive density $\frac{1}{\sigma_{inel}} \frac{d\sigma}{dy}$ develops a plateau in the center and the extreme ends remain unchanged in shape, then the average particle multiplicity will have the simple energy dependence

$$\langle n_i \rangle = A_i + B_i \log s \qquad (7)$$

where B_i is just the height of the central plateau. This trend is roughly observed in the charged multiplicity $\langle n_c \rangle$ for $s \geq 150$ Gev^2 and also in $\langle n_{\pi^o} \rangle$ for $s \geq 30$ Gev^2. Although $\langle n_{K_s^o} \rangle$ is also rising with log s, it probably will not reach the asymptotic form given by eq 7 until very much larger s values, as discussed below.

A comparison of the energy dependence of $\langle n_{K_s^o} \rangle$ with the energy dependence of charged particle multiplicities is shown in Fig. 31. There are 3 curves that fit the K_s^o data fairly well up to about 250 Gev/c. Curve (a) is a 2-parameter fit to 15 data points of the form

$$\langle n_{K_s^o} \rangle = A + B \log s \qquad [30].$$

Curve (b) is

$$\langle n_{K_s^o} \rangle = R\,(C + D \log s + E\, s^{-1/4} \log s)$$

where R is the overall K_s^o/charged ratio at 147 Gev/c, and C,D,E are taken from Stix & Ferbel's fit to $\langle n_c \rangle$ from $\pi^- p$ collisions [29]. Curve (c) is

$$\langle n_{K_s^o} \rangle = R\,(F + G \log s + H\, s^{-1/2})$$

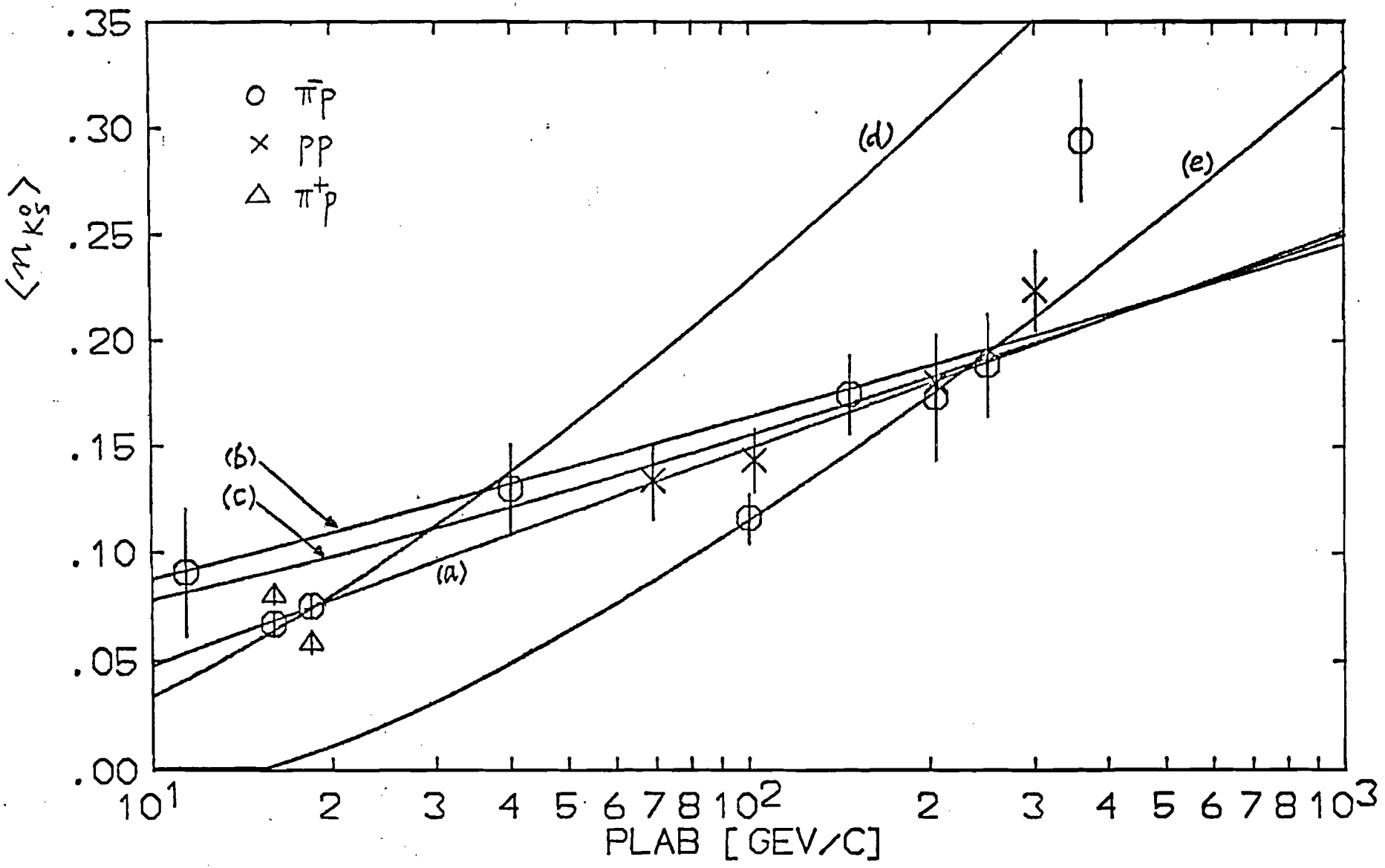

Fig 31. Fits to the energy dependence of $\langle n_{K^0_S} \rangle$

where F,G,H are taken from Antinucci's fit to $\langle n_c \rangle$ from pp collisions [31]. Although these curves represent the data quite well over most of the energy range, we do not expect them to hold at larger s values because eq 7 should hold only after the appearance of a rapidity plateau, but there is no sign of a plateau at 147 Gev/c. The fact that the K_s^o/charged ratio in the central region is larger than the over-all K_s^o/charged ratio suggests that asymptotically, $\langle n_{K_s^o} \rangle$ will rise more steeply with log s, in keeping with the trend of the 360 Gev/c data and curves (d) and (e) in Fig. 31 which are Antinucci's fits to $\langle n_{K^\pm} \rangle$ in pp collisions[31].

$\langle n_\Lambda \rangle$ in pp collisions is larger than $\langle n_\Lambda \rangle$ in $\pi^- p$ collisions. Both are varying very slowly with energy. This lack of energy dependence is characteristic of particles produced in the fragmentation regions. It is observed in inclusive proton production in pp collisions [31] and is probably also true in $\pi^- p$ collisions. There are indications that Λ's are produced mainly in the fragmentation region of the proton, as can be seen in Fig.24. However, the Λ/p ratio is not identical. Using $\sigma_{inel}(pp)$=33mb, and $\langle n_p \rangle_{pp}$ =1.3 at 147 Gev/c (from Ref.[31]), we estimate

$$\frac{\sigma(pp \rightarrow p)}{\sigma(\pi p \rightarrow p)} \sim \frac{(33mb)(1.3)}{8.3mb} \sim 5.2 \pm 0.1 \qquad (8)$$

Combining eqs. 6 and 8,

$$\frac{\sigma(pp \rightarrow \Lambda)}{\sigma(pp \rightarrow p)} \leq \frac{\sigma(\pi p \rightarrow \Lambda)}{\sigma(\pi p \rightarrow p)}$$

One should keep in mind that $\sigma(\pi^- p \rightarrow p)$ = (8.3±.16)mb at 147 Gev/c is based on a sample of slow protons identified by

ionization only and not corrected up for unidentified protons at medium and high lab momenta. Our tentative conclusion is that the Λ/p ratio is not the same in $\pi^- p$ and pp collisions, but it should be checked when more accurate data on inclusive proton production in $\pi^- p$ interactions become available.

3.3 Neutral-charged Correlations

One of the most remarkable regularities in multi-particle production at high energies is the phenomenum of KNO scaling first suggested by Koba, Nielsen, & Olesen [32] ("KNO") and later applied to neutral particle production by Dao & Whitmore [33] and Cohen [34]. In this section, after establishing the notation, we'll first digress a little to show it's easy to fit the charged multiplicity distribution using only a few parameters. Then we'll display the semi-inclusive neutral cross sections and attempt a simple parametrization.

Let $\sigma(n,n_o,\sqrt{s})$ be the cross section for producing n charged particles and n_o neutrals of some type, say K^o_s, at CM energy $\sqrt{s}$ in the following reaction

$$a + b \longrightarrow n \text{ charged} + n_o \text{ neutral} + \ldots$$

At asymptotic energies, KNO predict that the multiplicity distribution should reach a limiting form

$$\frac{\sigma(n,n_o,\sqrt{s})}{\sigma_{inel}} = \frac{1}{\langle n\rangle}\frac{1}{\langle n_o\rangle} U\left(\frac{n}{\langle n\rangle},\frac{n_o}{\langle n_o\rangle}\right)$$

where

$$\sigma_{inel} = \sum_n\sum_{n_o}\sigma(n,n_o,\sqrt{s}) \ ,$$

$$\langle n\rangle = \sum_n\sum_{n_o} n\ \sigma(n,n_o,\sqrt{s})/\sigma_{inel}$$

$$\langle n_o\rangle = \sum_n\sum_{n_o} n_o\ \sigma(n,n_o,\sqrt{s})/\sigma_{inel}$$

are respectively the average number of charged and neutral particles defined in the usual way over the normalized probability density $\sigma(n,n_o,\sqrt{s})/\sigma_{inel}$, and U is a function of $\frac{n}{\langle n\rangle}$ and $\frac{n_o}{\langle n_o\rangle}$ alone, with no explicit dependence on $\sqrt{s}$. It's convenient to think of U as a function of two continuous variables $z=\frac{n}{\langle n\rangle}$ and $z_o=\frac{n_o}{\langle n_o\rangle}$. With the correspondence

$$\sum_{n=0,2,4,\ldots} \leftrightarrow \frac{\langle n\rangle}{2}\int_0^\infty dz$$

$$\sum_{n_o=0,1,2,\ldots} \leftrightarrow \langle n_o\rangle \int_0^\infty dz_o$$

it is easy to verify that

$$\frac{n\ \sigma_n}{\sigma_{inel}} \equiv n \sum_{n_o} \sigma(n,n_o,\sqrt{s})/\sigma_{inel}$$

$$= \int dz_o\ z\ U(z,z_o) \equiv \Phi(z)$$

$$\frac{\langle n\rangle\ \sigma_n(0)}{\langle n_o\rangle\sigma_{inel}} \equiv \frac{\langle n\rangle}{\langle n_o\rangle} \sum_{n_o} n_o\ \sigma(n,n_o,\sqrt{s})/\sigma_{inel}$$

$$= \int dz_o\ z_o\ U(z,z_o) \equiv \Phi_o(z)$$

$$\frac{1}{2}\int dz\ \Phi(z) = \frac{1}{2}\int dz\ \frac{1}{z}\ \Phi(z) = 1 \qquad (9)$$

$$\frac{1}{2}\int dz\ \Phi_o(z) = 1 \qquad (10)$$

$$\frac{1}{2}\int dz\ \frac{1}{z}\ \Phi_o(z) = \frac{\langle n\rangle}{\langle n_o\rangle}\langle\frac{n_o}{n}\rangle$$

$$d_q \equiv \frac{1}{2}\int dz\ z^q\ \Phi(z) = \frac{\langle n^{q+1}\rangle}{\langle n\rangle^{q+1}}$$

$$c_{1,q} \equiv \frac{1}{2}\int dz\, z^q\, \Phi_o(z) = \frac{\langle n_o n^q\rangle}{\langle n_o\rangle\langle n\rangle^q}$$

The prediction that U and hence Φ and Φ_o should be energy independent is equivalent to the statement that the moments d_q and $c_{1,q}$ should be energy independent.

Note that Φ and Φ_o are two quite different beasts. $\Phi(z)$ depends only on the multiplicity distribution of the charged particles. Φ_o, on the other hand, depends on the joint multiplicity distribution of neutral and charged particles.

The charged particle cross sections for a selection of 6 π^-p and pp experiments [24-28] from 147 to 360 Gev/c are shown in Fig. 32 and again in Fig. 33. The curve in Fig.32 is $\Phi_s(z)=(a_1z^2+a_2z^4-a_3z^6+a_4z^8)\exp -a_oz$
the coefficients a_i were determined by Slattery in a fit to some pp data from 50 to 303 Gev/c in the range $0.2\leq z\leq 3$ [35]. The curve in Fig.33 is

$$\Phi_{23}(z) = \alpha\,\Phi_2(z) + (1-\alpha)\,\Phi_3(z) \qquad (11)$$

where $\Phi_2(z) = A\, z^2 \exp -(Bz)^2$

$\Phi_3(z) = C\, z^2 \exp -(Dz)^3$

The coefficients A,B,C,D were determined by requiring Φ_2 and Φ_3 separately satisfy the normalization conditions eq. 9 [36]. $\alpha = 0.632 \pm 0.026$ was determined by a 1-parameter fit ($X^2 = 126$ for 81 data points). With this value of α,

$$d_1 = \frac{\langle n^2\rangle}{\langle n\rangle^2} = \alpha/\Gamma^2(\tfrac{3}{2}) + (1-\alpha)\Gamma(\tfrac{4}{3})\Gamma(\tfrac{2}{3})$$

$$= \langle n_+n_-\rangle / \langle n_+\rangle\langle n_-\rangle \quad \text{for } \pi^-p$$

$$= 1.25 \pm .002$$

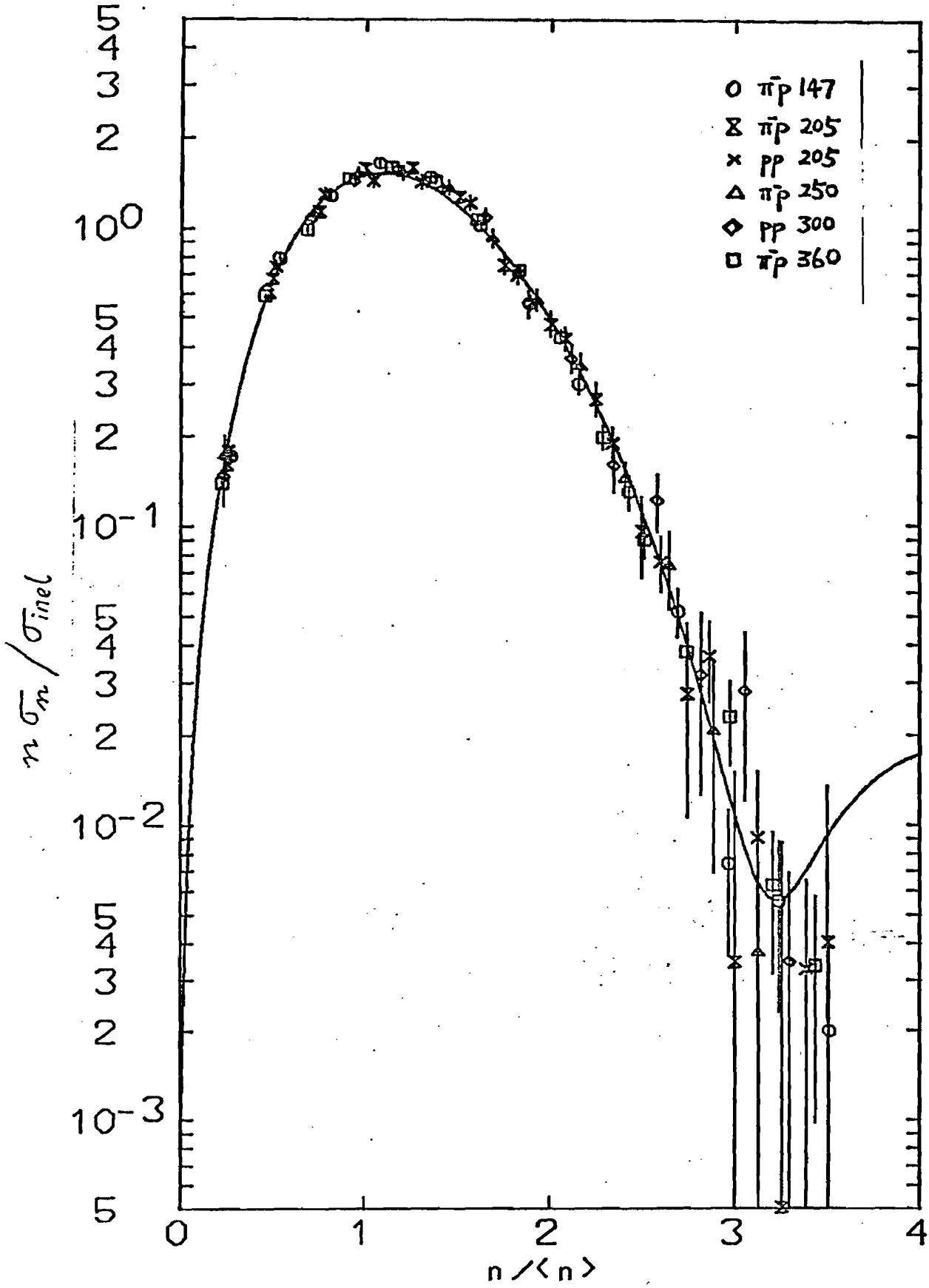

Fig 32. Semi-inclusive charged particle cross sections curve is $\Phi_s(z)$

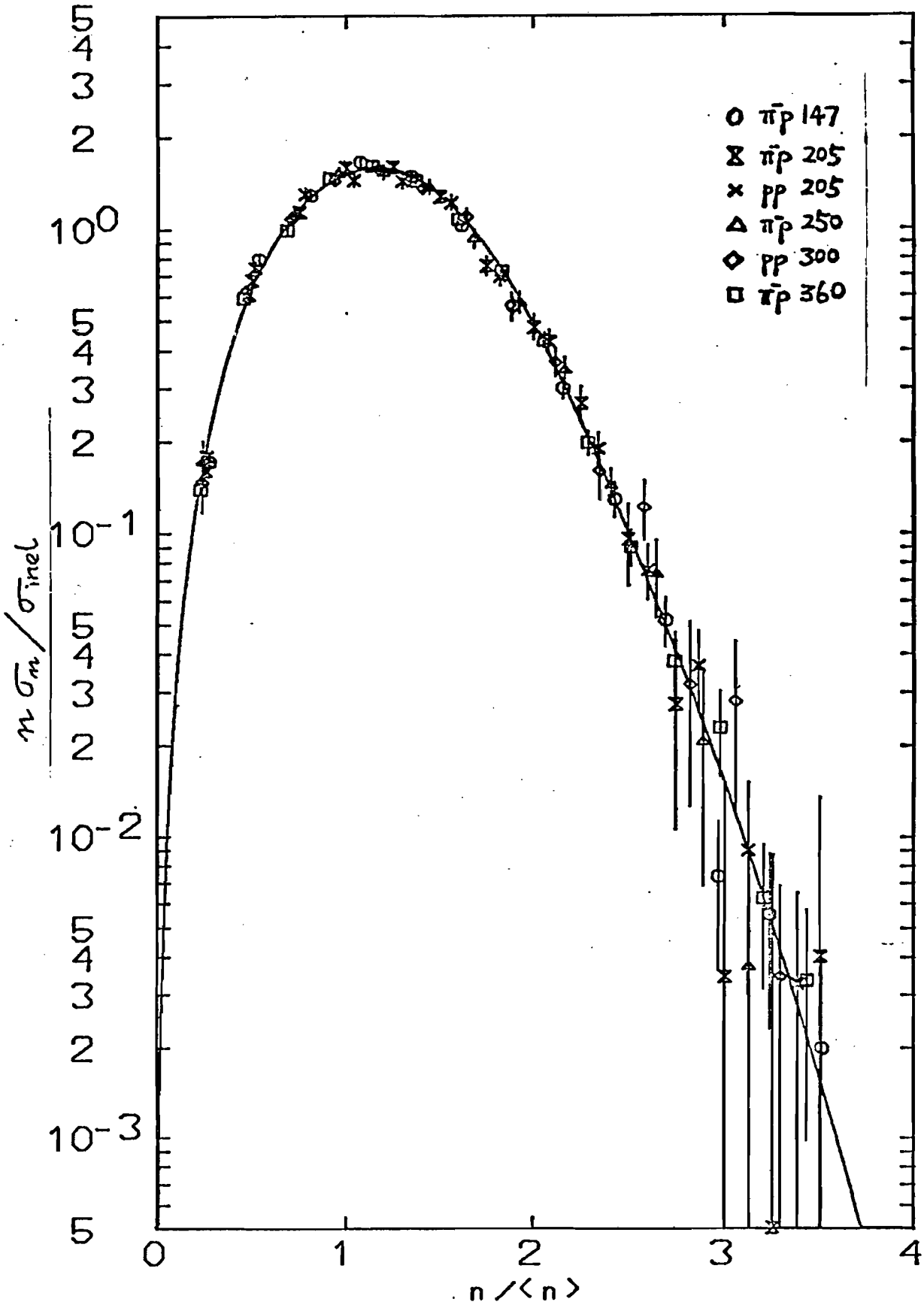

Fig 33. Semi-inclusive charged particle cross sections curve is $\varrho_{23}(z)$

We don't know of any theoretical justification for eq 11.

The semi-inclusive neutral cross section, suitably normalized, are shown in Figs. 34-37. There are several features worth noting:

(1) With these relatively large error bars, all the neutral data are quite consistent with the KNO prediction of an asymptotic form $\Phi_o(z)$ for both π^- and proton induced reactions.

(2) Compared to the curve $\Phi_{23}(z)$ representing the charged particle data, the data points tend to lie above the curve for $z<1$ and below the curve for $z>1$, i.e. the neutral/charged ratio of semi-inclusive cross sections $\frac{\sigma_n(0)}{n\sigma_n}$ decreases as z increases. It is unlikely that the effect is due to experimental difficulties with the high multiplicity events.

(3) As a corollary to (2), the average value of $\Phi_o(z)$ is smaller than the average value of $\Phi(z)$, or

$$c_{1,1} = \frac{\langle n_o n\rangle}{\langle n_o\rangle\langle n\rangle} < d_1 = \frac{\langle n^2\rangle}{\langle n\rangle^2} .$$

To obtain a quantitative parametrization of the neutral data, we tried a form similar to Φ_{23} because that gave a reasonable fit to the charged particle data.

$$\Phi_o(z) = \alpha\, \Phi_{02}(\beta_2,z) + (1-\alpha)\, \Phi_{o3}(\beta_3,z) \qquad (12)$$

where
$$\Phi_{o2}(\beta,z) = \frac{4\beta^3 B^3}{\Gamma(3/2)}\, z^2 \exp -(\beta Bz)^2$$

$$\Phi_{o3}(\beta,z) = \frac{6\beta^3 D^3}{\Gamma(1)}\, z^2 \exp -(\beta Dz)^3$$

Both Φ_{o2} and Φ_{o3} satisfy the normalization equation 10 and

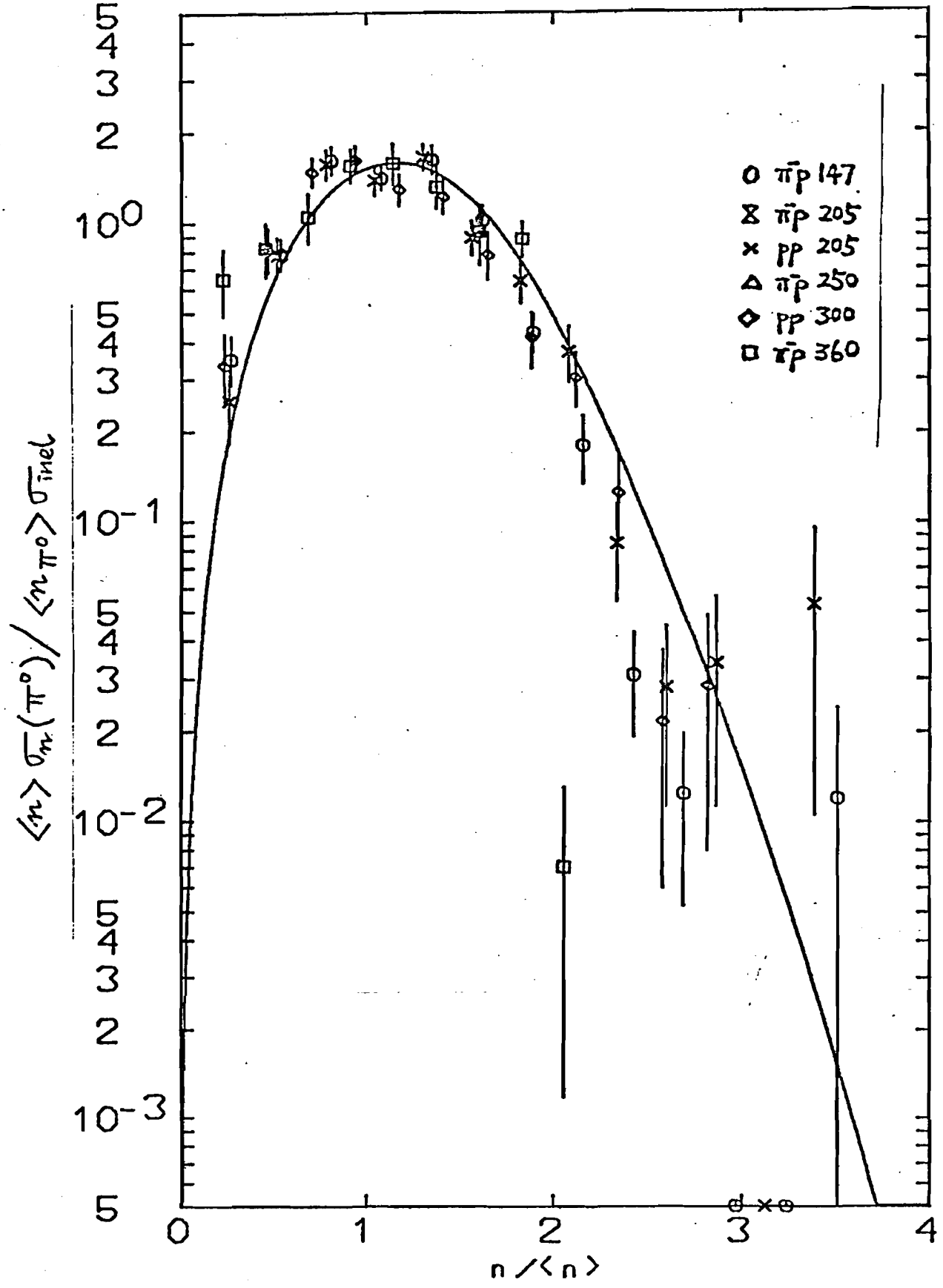

Fig 34. Semi-inclusive π^0 cross sections, curve is $\Omega_{23}(z)$

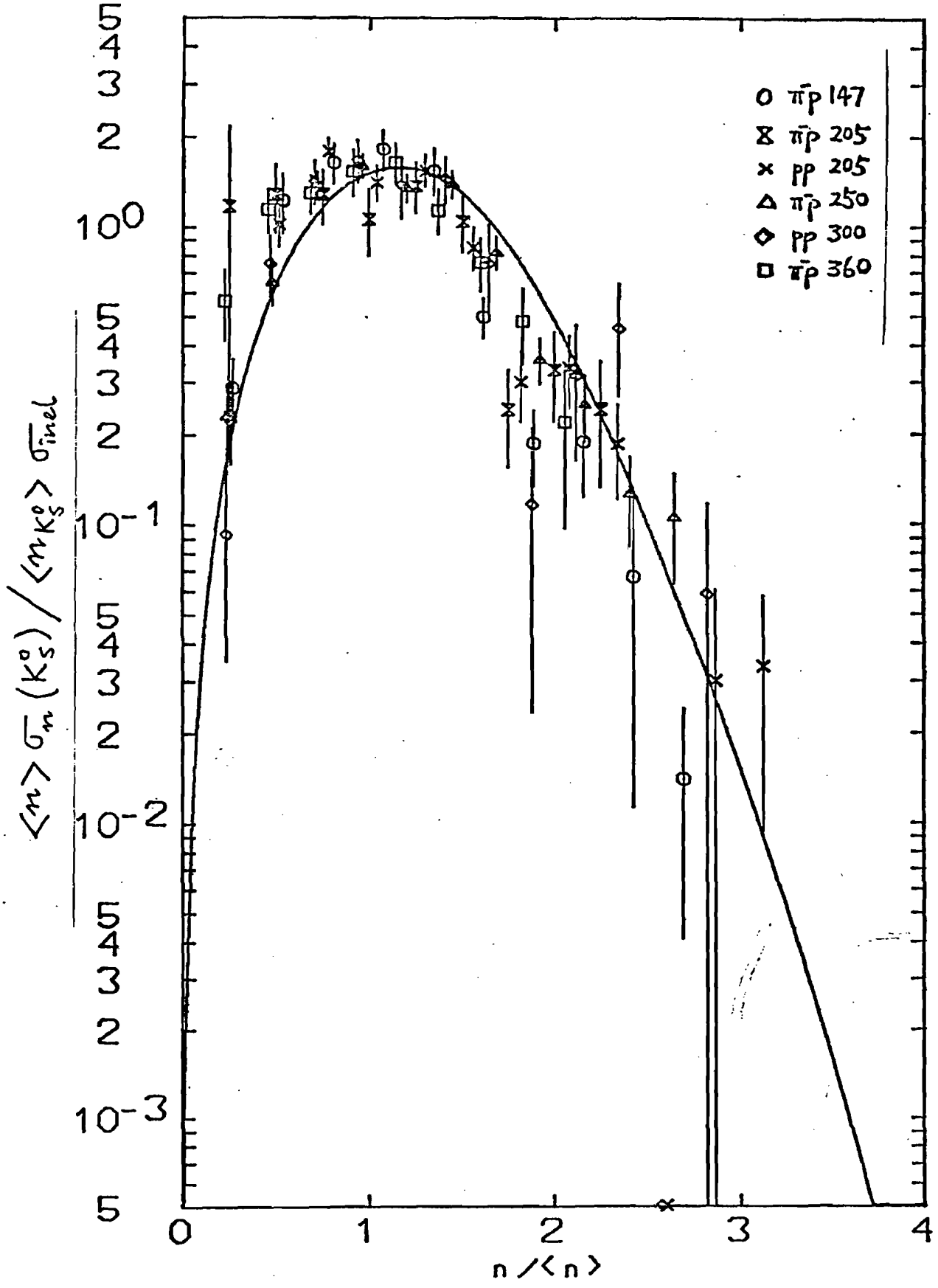

Fig 35. Semi-inclusive K^o_s cross sections, curve is $\Phi_{23}(z)$

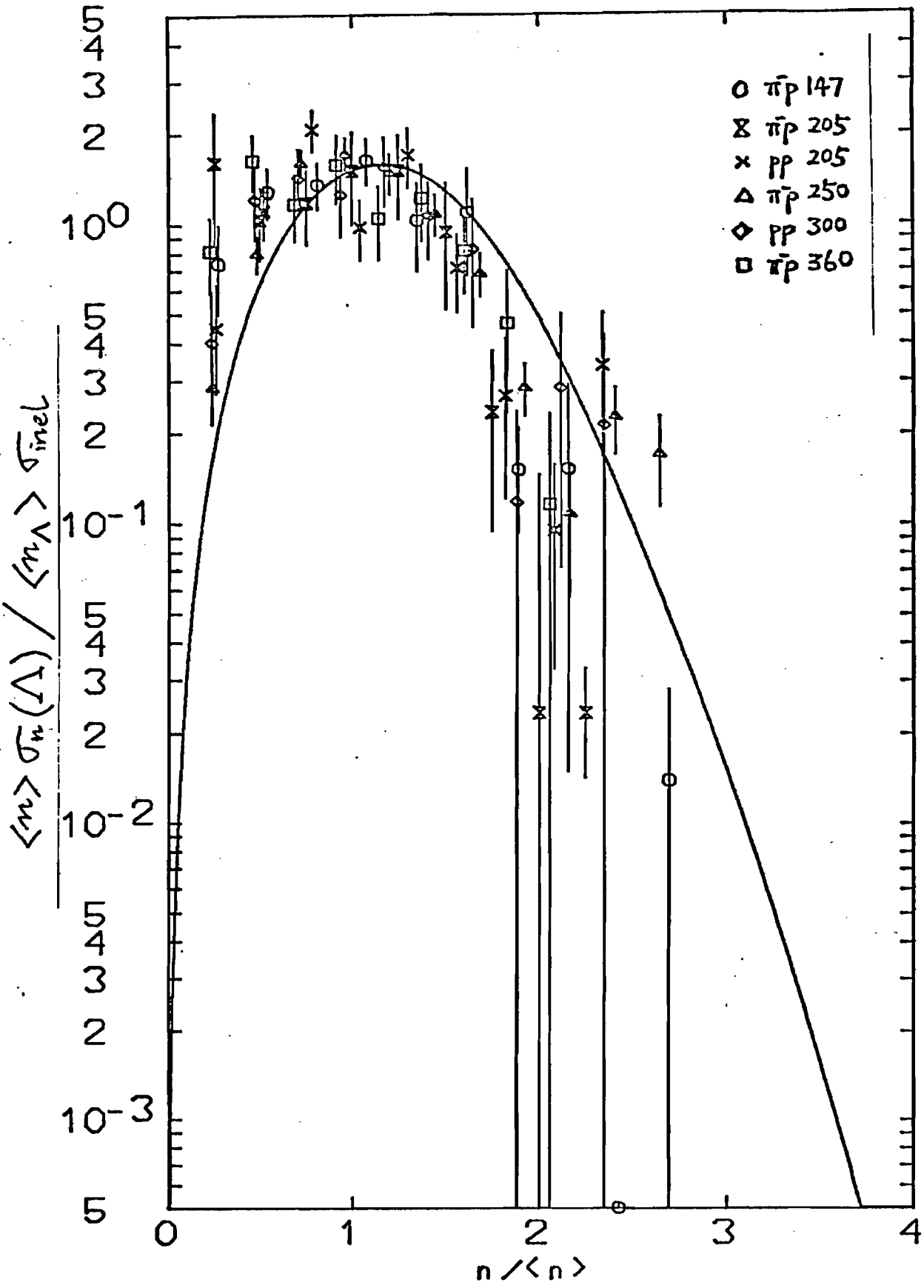

Fig 36. Semi-inclusive Λ cross sections, curve is $\Omega_{23}(z)$

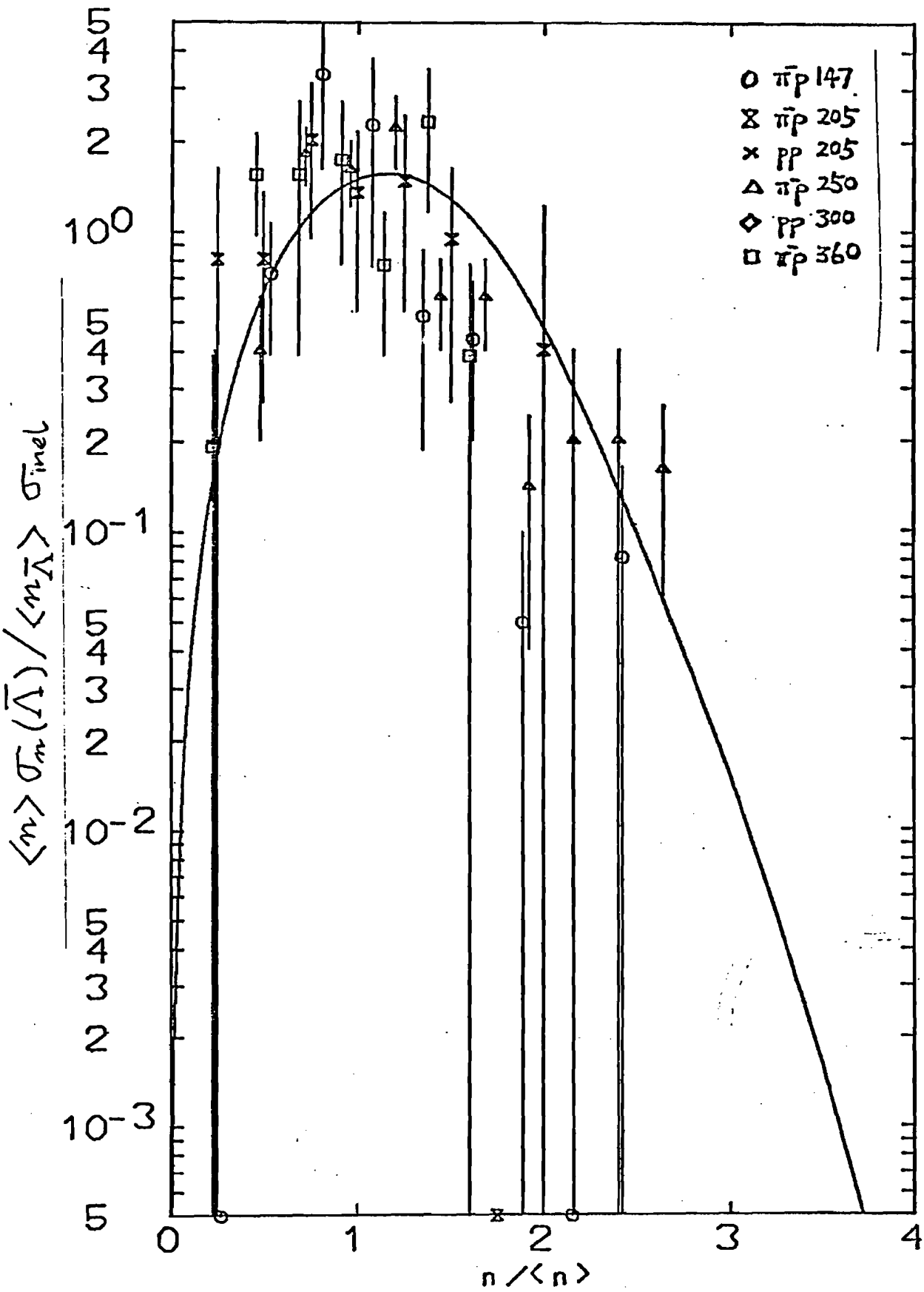

Fig 37. Semi-inclusive $\bar{\Lambda}$ cross sections, curve is $\Phi_{23}(z)$

reduce to Φ_2 and Φ_3 when $\beta=1$.

The results of 3-parameter fits to the π^o, K_s^o, and Λ data are listed in Table 10 and shown in Figs. 38-40. [37].

Table 10. 3-parameter Fits to Neutral Data

	π^o	K_s^o	Λ
α	0.6142 ±.1291	0.3938 ±.0874	0.5604 ±.1371
β_2	1.2016 ±.0569	0.9721 ±.0483	1.3548 ±.0594
β_3	0.9456 ±.0479	1.2472 ±.0298	1.0576 ±.0457
X^2/DF	57/40	112/58	99/54
$\frac{\langle n_o n\rangle}{\langle n_o\rangle\langle n\rangle}$	1.1441 ±.0198	1.1036 ±.0120	1.0292 ±.0215
$\frac{\langle n_o/n\rangle}{\langle n_o\rangle/\langle n\rangle}$	1.1029 ±.0192	1.1388 ±.0131	1.2242 ±.0287

Since we don't have any particular motivation for the form of eq. 12, it is difficult to attach meaning to the individual parameters α, β_2, and β_3. Therefore we have also tabulated in Table 10 two more easily interpreted quantities:

$$c_{1,1} = \frac{\langle n_o n\rangle}{\langle n_o\rangle\langle n\rangle} = \alpha/\beta_2\Gamma^2(\tfrac{3}{2}) + (1-\alpha)\Gamma(\tfrac{4}{3})\Gamma(\tfrac{2}{3})/\beta_3$$

$$c_{1,-1} = \frac{\langle n_o/n\rangle}{\langle n_o\rangle/\langle n\rangle} = \alpha\beta_2 + (1-\alpha)\beta_3$$

The trend in Table 10 is clear. The stronger the correlation with charged particles, the smaller the departure from a constant neutral/charged ratio. π^o's are most strongly correlated with charged particles; Λ's, least correlated.

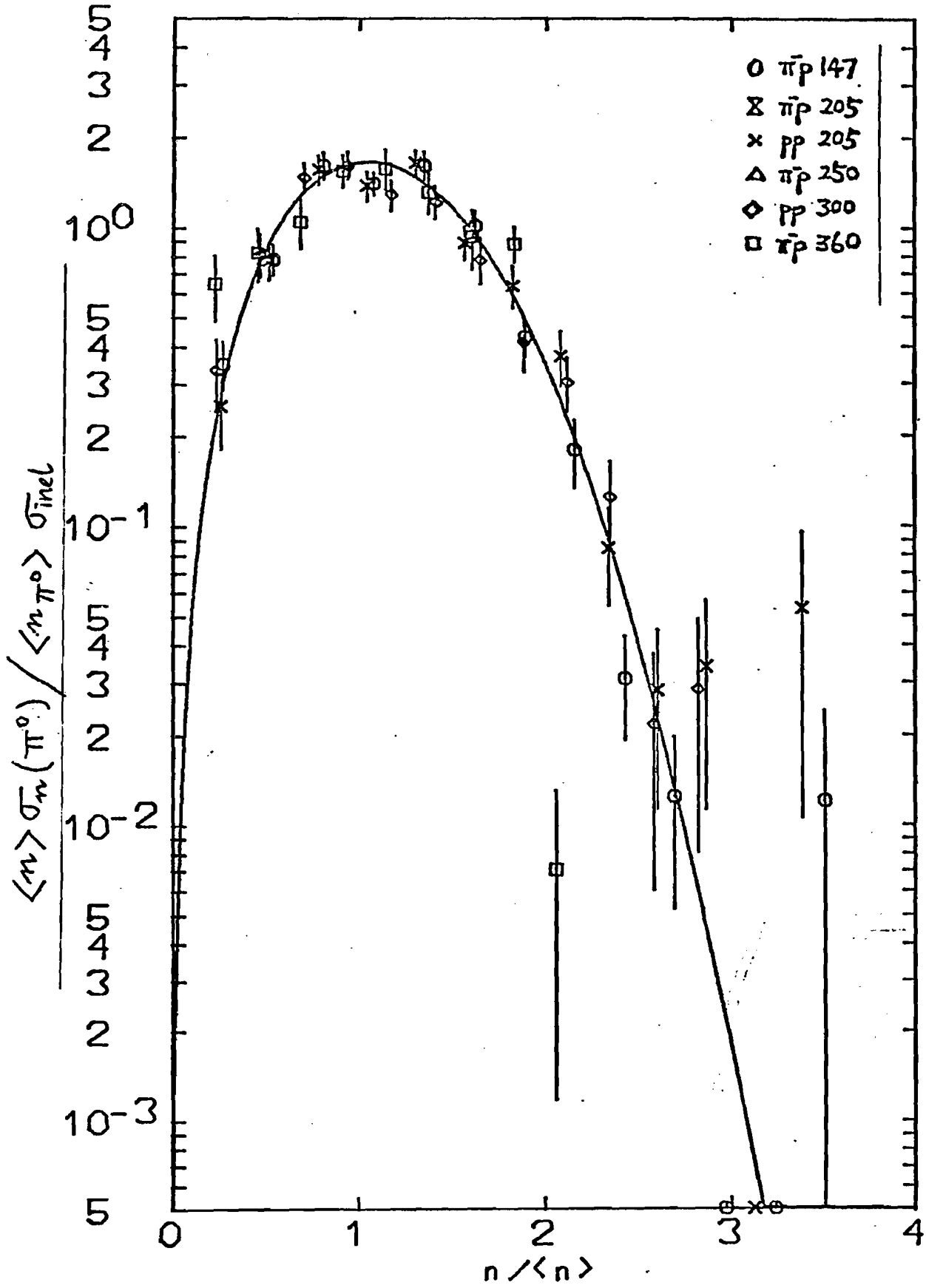

Fig 38. 3-parameter fit to π^0 data

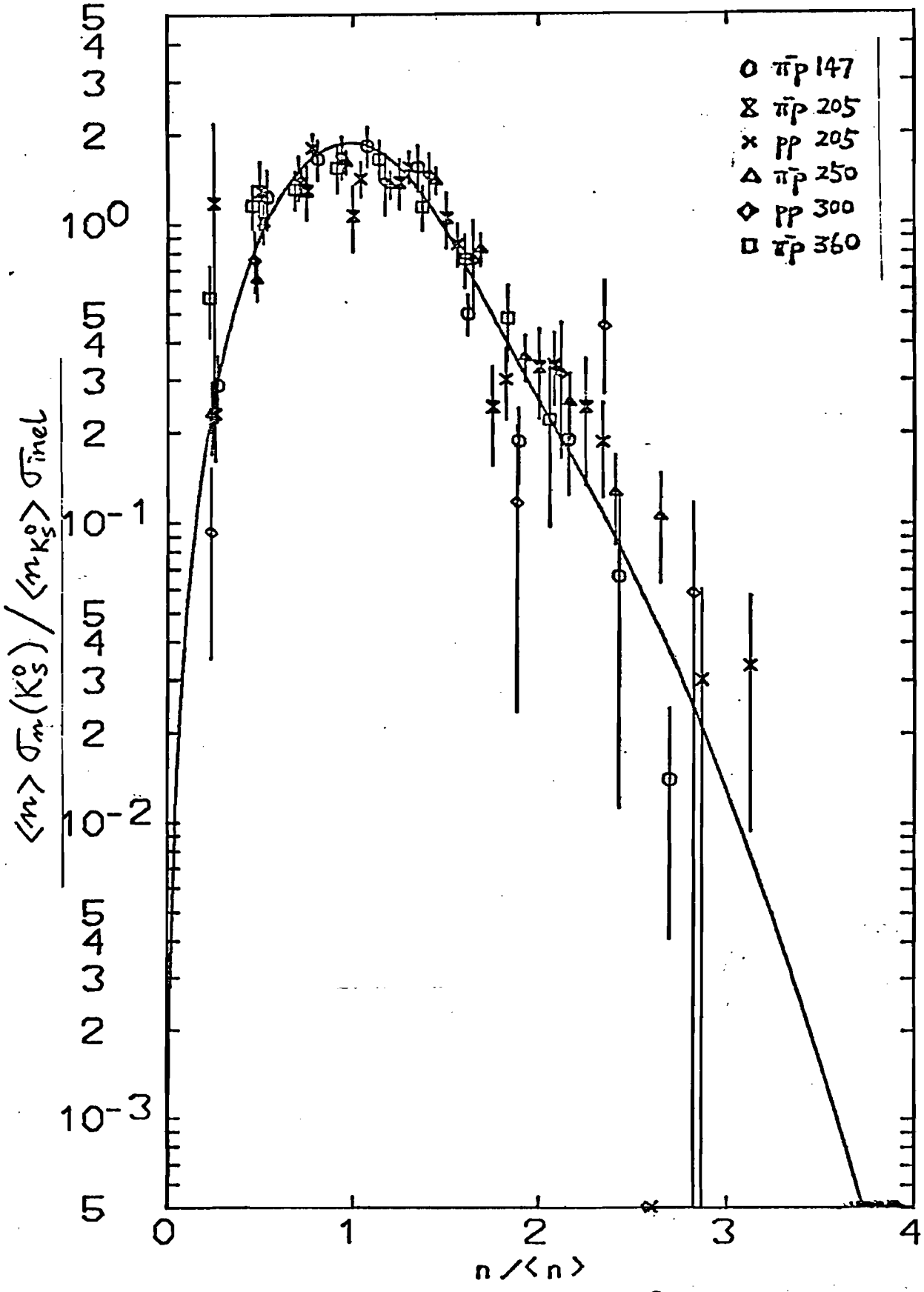

Fig 39. 3-parameter fit to K_s^o data

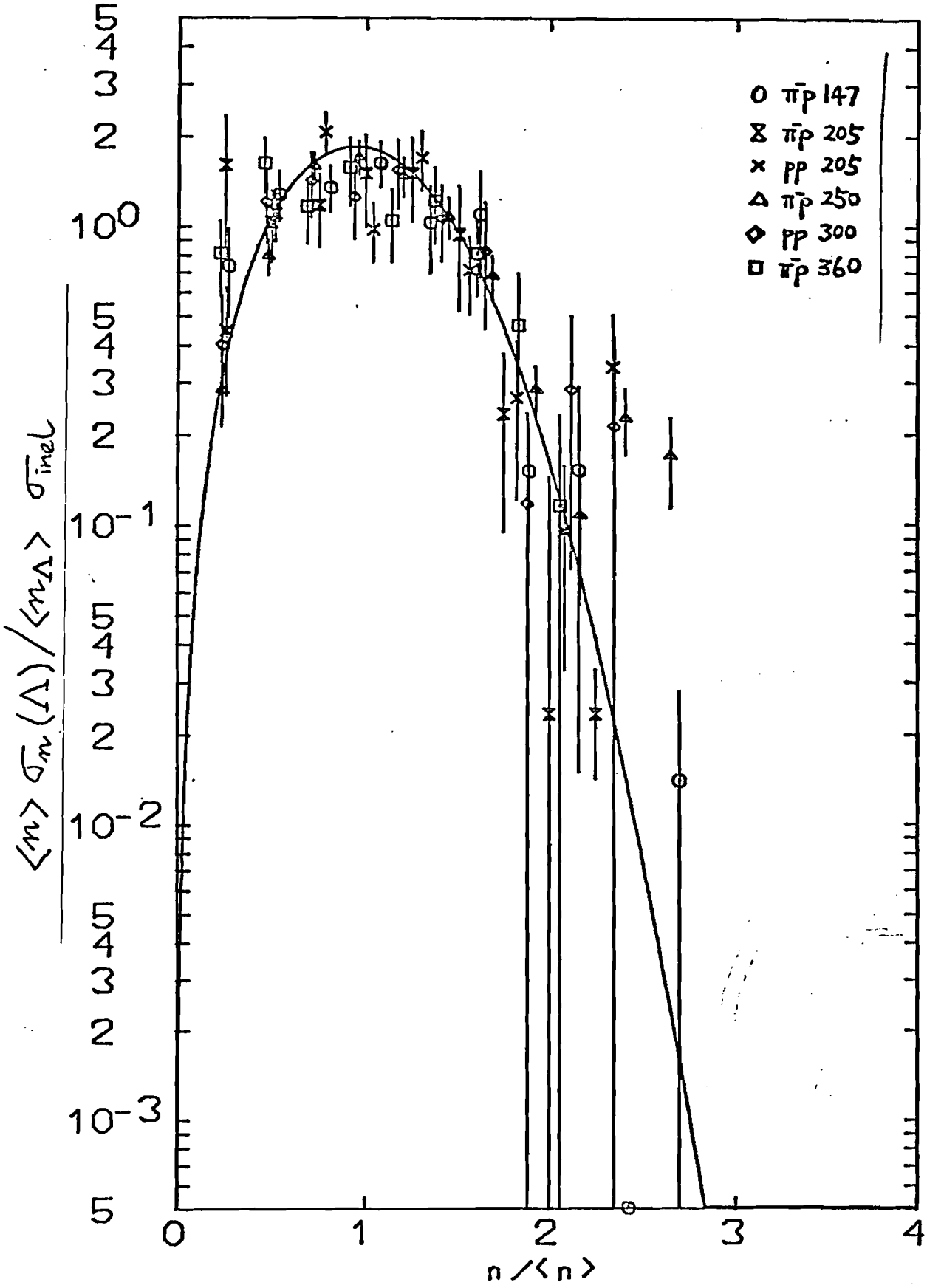

Fig 40. 3-parameter fit to Λ data

None of the neutral-charged correlations is as strong as the charged-charged correlation ($c_{1,1} < d_1$). The neutral/charged ratio is not independent of the charged multiplicity; it is larger than average in the low charged multiplicity events ($c_{1,-1} > 1$). The effect is most prominent for the Λ's.

3.4 Neutral-neutral Correlations

The inclusive two-particle neutral cross sections are listed in Table 11.

Table 11. Inclusive Two-particle Neutral Cross Sections

a,b	# of pairs	σ(a,b) [mb]	$C_{a,b}$
$\pi^o\pi^o$	83	221.±50	1.12±0.26
$\pi^o K^o_s$	71	14.9±3.3	1.32±0.31
$\pi^o\Lambda$	34	6.11±2.85	1.20±0.58
$\pi^o\bar{\Lambda}$	3	1.7 ±1.6	1.5 ±1.4
$K^o_s K^o_s$	28	1.51±0.45	2.36±0.75
$K^o_s\Lambda$	31	.603±.174	2.09±0.66
$K^o_s\bar{\Lambda}$	2	0.34±0.33	5.1 ±5.1
$\Lambda\bar{\Lambda}$	1	.034±.034	1.1 ±1.1

Cross sectons involving π^o's are obtained from those involving γ's by

$$\sigma(\pi^o,\pi^o) = \frac{1}{4}\sigma(\gamma,\gamma) - \frac{1}{4}\sigma(\gamma)$$

$$\sigma(\pi^o,X) = \frac{1}{2}\sigma(\gamma,X) \quad , X\neq\pi^o.$$

The neutral-neutral correlations $C_{a,b}$ are given by

$$C_{a,b} = \frac{\sigma(a,b)}{\sigma(a)\sigma(b)}\,\sigma_{inel}$$

$$= \frac{\langle n_a n_b \rangle}{\langle n_a \rangle \langle n_b \rangle} \qquad , a \neq b$$

$$= \frac{\langle n_a (n_a - 1) \rangle}{\langle n_a \rangle \langle n_a \rangle} \qquad , a = b$$

All quoted errors are statistical only. The $K_s^o K_s^o$, $K_s^o \Lambda$, and $K_s^o \overline{\Lambda}$ cross sections are slightly larger but consistent with being equal to the results from $\pi^- p$ 250 Gev/c but with better statistics [38].

The trend of the neutral-neutral correlations in Table 11 is that the correlations between pairs containing zero or one strange particle are comparable to the neutral-charged and charged-charged correlations in the last section. Correlations between two strange particles, with the possible exception of $\Lambda \overline{\Lambda}$, seem to be larger than the rest.

Λ's are produced primarily in the fragmentation region of the target proton; $\langle n_\Lambda \rangle$ in pp collisions is larger than $\langle n_\Lambda \rangle$ in $\pi^- p$ collisions; neither is changing with energy.

π^o, K_S^o, and $\bar{\Lambda}$'s are centrally produced like the bulk of the charged particles. $\langle n_{\pi^o} \rangle$, $\langle n_{K_S^o} \rangle$, and $\langle n_{\bar{\Lambda}} \rangle$ are the same for $\pi^- p$ and pp collisions and are rising logarithmically with energy. The central region K_S^o/charged ratio, measured by $d\sigma/dy$ at $y=0$, is $(4.06 \pm 0.71)\%$. The ratio of the inclusive cross sections is slightly smaller $(2.36 \pm 0.18)\%$.

The semi-inclusive neutral cross sections are consistent with KNO scaling. Neutral-charged correlations are weaker than charged-charged correlations.

$K_S^o K_S^o$ and $K_S^o \Lambda$ correlations are 1-2 standard deviations above the un-correlated value 1. The other neutral-neutral correlations are consistent with no correlation.

(III) Scanning for Events

Figure 41 shows how the fiducials and frame number appear in each of the 3 views. The dotted box in view 1 defines the fiducial volume. If the primary vertex of an event lies outside the fiducial volume, no information need be recorded.

If a primary vertex lies within the fiducial volume in view 1, record an event ID by setting the thumb wheel switches as follows:

switch #	name	contents
8-9	EXP	experiment # = 41
10-11	ET	event-type = 1(IPD) or 3(HM)
13-18	FR	frame # = 6-digit frame number
19	AD	additional event
20	RM	remeasurement # = 1 at present
21-22	SCAN	scan # = 1 at present
25-26	OP	operator #
27-28	ED	track count
34-36	ROLL	3-digit roll #
38-39	COM	comment=1 faint or crowded event =2 problem event =0 accepted event

All other switches should be set to 0.

If there are 2 or more events in a frame, measure them in the order in which the primary vertices appear as you follow the beam tracks from the bottom of the picture to the top. Set additional event =0 for first event, =1 for second event, =2 for third, etc.

Track-count is the number of charged secondaries originating from the primary vertex excluding identified Dalitz electrons. The track count will usually be even (0,2,4,6,..).

An event should be flagged as comment 1 (faint or crowded event) if any of the following is satisfied:

1. The tracks in the event are faint.
2. There are more than 10 beam tracks entering the fiducial volume.
3. There are more than 10 incoming secondary tracks entering the fiducial volume.

An event that is not faint or crowded should be flagged as comment 2 (problem event) if any of the following is satisfied:

1. There is a secondary interaction within 5mm of the primary vertex.
2. It is impossible to find the same number of tracks originating from the primary vertex in all 3 views. (The track-count in this case should contain the maximum of the track-counts obtained in 3 views.)

Note that for comment 1 and comment 2 events, the track-count should be recorded in switches 27-28, but no track points are needed. All other events should be flagged with comment 0 (accepted event), and the track points measured according to the rules in the next section.

Frame numbers of blank frames should be recorded in the log book.

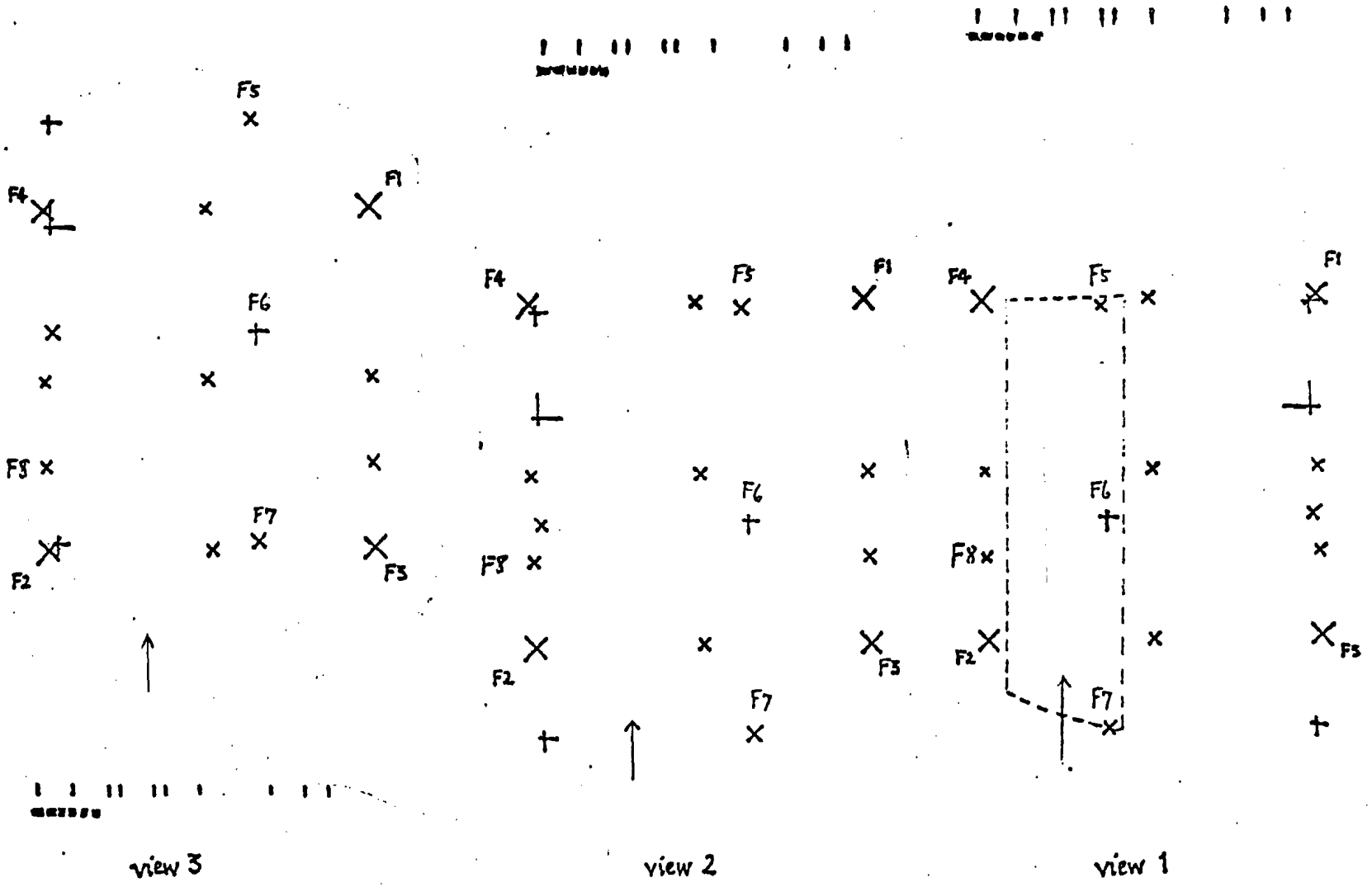

Fig 41. The fiducial volume

(IV) Measuring Tracks (IPD)

A point is measured by the measuring switch/foot pedal (denoted by b0), or one of eight buttons on the IPD table (denoted by b1, ..., b8).

A. Generation 1 Information

The first 7 points measured in each view shall be:

1. fiducial #1,labeled f1 in Figure 41,(b0)
2. fiducial #2 (b0)
3. primary vertex (b0)
4. CP on beam track (b0)
5. EP on beam track (b0)
6. 1st point on reference ionization track, near the downstream end of track (b0)
7. 2nd point on reference ionization track, slightly before primary vertex (b0)

If an interacting beam track or a secondary track is used as the reference ionization track, the first point should be farther away from the primary vertex than the second one. The beam track and the reference ionization track should each have exactly 2 points measured.

B. Generation 2 Tracks

Each secondary track shall consist of the following points:

1. UHP (b1) if vertex is obscured from the main body of the track
2. CP (b0) near the middle of the track
3. one or more ECP (b2) if there are small angle crossing tracks
4. EP (b0) near the point where track leaves the chamber (But do not measure a track through more than a third of a circle-120 degree turning angle)

   or

   SP (b3) at the point where the track stops

   or

   MUV (b5) at the point where π decays into μ

   or

   DV (b6) at the secondary vertex or decay vertex

Use UHP and ECP's whenever a track is obscured by flares or other small-angle crossing tracks. However, if 2 or more forward tracks are nearly on top of each other throughout the entire length of the chamber, simply measure 2 points (CP and EP/SP/MUV/DV) for each track even though they may not be useful to PEPR.

C. Generation 3 Tracks

Measure all generation 3 tracks except the μ in a π-μ-e and tracks originating from a secondary vertex. This class includes decays, vee's, gamma pairs, and Dalitz electrons. The order in which generation 3 tracks are measured is important. A track originating from a decay vertex should be measured immediately after the secondary track from which it decayed. Vee's, gamma pairs, and Dalitz electrons should be measured in that order, after all secondary tracks. Generation 3 tracks are measured like generation 2 tracks with the following points added:

1. vertex of vee (b3) immediately before the 2 tracks of the vee
2. vertex of the gamma-pair (b5) immediately before the 2 tracks of the gamma pair
3. primary vertex (b6) immediately before Dalitz electrons
4. decay vertex (b7) immediately before track originating from decay vertex

Ignore vee's, gamma pairs, and decays that are not visible in all 3 views. If a secondary vertex is not visible in all 3 views, IPD the track as if it did not undergo a secondary interaction.

If there are 2 events in the same frame and a vee (or gamma pair) may be associated with either event, measure the vee (or gamma pair) once for each event.

The tracks of a vee should be matched in 3 views. For example, if the positive track is measured before the negative track in view 1, then do the positive track first in view 2 and 3.

If there are 2 or more vee's in the same event, measure the vee's in the same order in all 3 views. The same goes for gamma pairs and Dalitz electrons.

The following table summarizes the button functions.

button	function
b0	fiducials,CP,EP
b1	UHP
b2	ECP
b3	SP ;vertex of vee
b5	MUV ;vertex of gamma pair
b6	DV ;vertex of Dalitz electron
b7	;decay vertex
b9	terminate view

D. Error Messages

If more than 99 points are measured in any view, ONLINE types "no more points". These events should be killed and re-entered as comment 3. After (b9) is pushed, the online program will check that the number of generation 2 tracks you have measured is equal to the track count in switches 27-28 and also that the total number of tracks measured is the same as in previous views ("view incomplete").

A 110 command will type out
"pts: nn/01. tkv:aa/cc. tks: bb/dd."
nn is the number of points measured this view.
cc = 1 + the total number of tracks required this view.
dd = 1 + the number of secondary tracks required this view.
aa,bb are the corresponding measured quantities this view.

E. Fiducial Measurement

At the beginning of the day, or at the beginning of a new roll, or when you change roll to a new table, pick a frame without an interaction and measure the 7 labelled fiducials in all 3 views (see Fig. 41). Set up the event ID as for an event but with track-count =0 and event-type =2. measure the points in the order f1, f2, f3, f4, f5, f6, f7, then (b9).

Do not use a frame that has any event in it. If, however, the first frame on a roll or at the beginning of the day has an event in it, measure that frame but set a frame number that is one less in the switches.

When fitting to experimental data, very often the measured values are Gaussianly distributed. The techniques for making linear fits in these cases are well known. We want to introduce a linear fitting technique that is applicable when the probability for obtaining an experimental result is uniformly distributed in some interval and zero outside. This situation occurs when attempting to reconstruct straight line trajectories of charged particles traversing a set of multi-wire proportional chambers.

Suppose we measure N quantities for which we obtain the experimental values x_i with errors σ_i. We also have "theoretical" expressions for these quantities

$$t_i(a_1,\ldots,a_M) = \sum_{\mu=1}^{M} C_{i\mu} a_\mu$$

which are linear homogeneous functions of M parameters a_μ. The parameters are to be adjusted to give a best fit to the data.

First consider the case where the probability distribution for the experimental results x_i are Gaussian. This will lead to the familiar linear least square fit. The likelihood function is

$$L(a) = k \exp(-\tfrac{1}{2}X^2)$$

where k is a normalization constant and

$$X^2 = \sum_{i=1}^{N} (x_i-t_i)^2/\sigma_i^2 .$$

Define a "data vector" X and a "measurement matrix" M with components as follows

$$X_\mu = \sum_{i=1}^{N} C_{i\mu} x_i / \sigma_i^2$$

$$M_{\mu\beta} = \sum_{i=1}^{N} C_{i\mu} C_{i\beta} / \sigma_i^2$$

Then the condition that L(a) is maximum at $a=a^*$ may be written as the matrix equation

$$X=Ma^*$$

with solution

$$a^* = M^{-1}X.$$

The errors in the fitted parameters are

$$\Delta a_\mu = (M^{-1}{}_{\mu\mu})^{1/2} .$$

We may also write

$$X^2(a) = \sum_{\mu,\beta=1}^{M} (a_\mu - a^*_\mu) M_{\mu\beta} (a_\beta - a^*_\beta)$$

and verify the following

$$a^*_\mu = \langle a_\mu \rangle = \int d^M a \; a_\mu L(a) \tag{13}$$

$$(M^{-1})_{\mu\beta} = \langle (a_\mu - a^*_\mu)(a_\beta - a^*_\beta) \rangle$$

$$= \int d^M a \; (a_\mu - a^*_\mu)(a_\beta - a^*_\beta) L(a) \tag{14}$$

i.e. if we think of the likelihood L as a probability density in M-dimensional parameter space, then the best fit for the parameters a_μ are just the first moments of L, the elements of the error matrix are just the second moments of L.

Now consider the case where the probability distribution for the experimental results is uniform in some finite region. The normalized likelihood is

$$L(a) = k \prod_{i=1}^{N} [\theta(t_i - x_i + \sigma_i) - \theta(t_i - x_i - \sigma_i)]$$

Since $t_i(a)$ is linear in a_μ,

$$t_i(a) - x_i + \sigma_i = 0$$

is the equation of a hyper-plane in M-dimensional parameter space. The step function $\theta(t_i - x_i + \sigma_i)$ corresponds to the inequality $t_i - x_i + \sigma_i \geq 0$ which constrains L to be zero on one side of the hyper-plane. Thus L is a constant and non-zero inside a "feasible region" V. The boundaries of the feasible region are hyper-planes. On a boundary hyper-plane, one of the 2N inequalities is satisfied as an equality. A vertex of the feasible region is the point at which M hyper-planes intersect. At a vertex, M of the 2N inequalities are satisfied as equalities.

Since L is constant, the usual technique of obtaining the maximum by setting the first derivative equal to zero is not applicable. However it still makes sense to calculate

moments of L. If we think of the feasible region as a M-dimensional solid object with unit mass and uniform density, i.e. L is a mass density, then equations 13 and 14 say the best fit for a_μ is just the center of gravity of the solid and the error matrix is just the moment of inertia tensor.

For an irregularly shaped object, one might think of resorting to numerical integration to calculate its volume (or mass), center of gravity, and moment of inertia. But that is not necessary. In fact, these calculations are quite trivial if we use the superposition principle which says that we can divide up the object into many pieces and treat each piece as if all its mass is concentrated at its center of gravity. We'll illustrate this with an example M=2, N=3.

Suppose the inequalities, which are just half planes bounded by straight lines, are as shown in Fig. 42a. The feasible region, which is the intersection of all the half planes, is shaded. Note that not every line contributes to the boundary. There are 6 lines but the feasible region has only 5 sides. It is intuitively obvious that the feasible region will always be a convex polygon with its center of gravity located inside the polygon. Choose any point in the interior of the feasible region, connect it to all the vertices dividing the polygon into 5 triangles as shown in Fig. 42b. For the j-th triangle with vertices at

$$\tilde{a}_1,\ \tilde{a}_2,\ \tilde{a}_3,$$

the center of gravity is at

$$\tilde{g}_j = \tfrac{1}{3}(\tilde{a}_1+\tilde{a}_2+\tilde{a}_3)$$

and its area is

$$m_j = \tfrac{1}{2}\det\begin{vmatrix} a_{1x} & a_{1y} & 1 \\ a_{2x} & a_{2y} & 1 \\ a_{3x} & a_{3y} & 1 \end{vmatrix}$$

For the whole polygon, the center of gravity is

$$\tilde{G} = \sum_{j=1}^{5} m_j\tilde{g}_j \Big/ \sum_{j=1}^{5} m_j$$

and the moment of inertia tensor is

$$I_{xy} = \sum_{j=1}^{5} m_j(g_{jx}-G_x)(g_{jy}-G_y)\ .$$

To reconstruct trajectories from hits in a set of multi-wire proportional chambers, 4 numbers are needed to

(a)

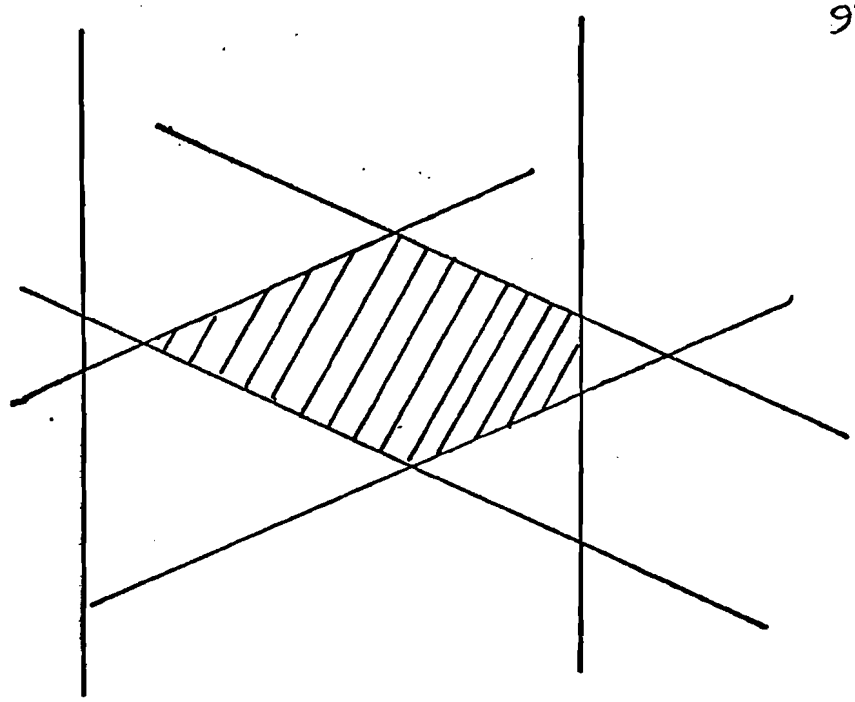

(b)

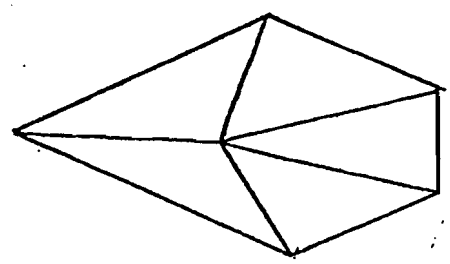

Fig 42. A feasible region in 2-dimensions

parametrize a straight line so M=4; let's say there are N=16 planes. The generalization to 4 dimensions is no problem. A vertex is the intersection of 2 lines in 2 dimensions, 3 planes in 3 dimensions, and 4 hyper-planes in 4 dimensions. Finding a vertex requires solving 4 simultaneous linear equations or inverting a 4x4 matrix. A triangle in 2 dimensions becomes a tetrahedron in 3 dimensions and a 4-simplex in 4 dimensions. Such an object has 5 vertices and 5 boundary hyper-planes formed by taking the vertices 4 at a time. Once the vertex coordinates of a 4-simplex are known, the center of gravity can be calculated by taking an average, and the volume calculated from a 5x5 determinant. For N=16, there are 32 inequalities. The feasible region will have a large number of vertices. This is not a difficulty in principle. In practice, a little care will save a lot of computer time. E.g. to find the vertices of the feasible region, it is not necessary to calculate all possible intersections of 32 hyper-planes taken 4 at a time. Suppose we have inverted a matrix A and found that it corresponds to a vertex of the feasible region. To find the coordinates of a neighboring vertex which shares 3 hyper-planes in common, it is not necessary to invert a matrix B from scratch. Since A and B differ in only one row, B^{-1} can be found from A^{-1} after one Gaussian elimination step.

To save programming effort, the reconstruction program PWGP does not use the simplex technique. Instead, uniform probability distributions corresponding to hits from wire planes are replaced by Gaussians with the same average and variance and tracks are obtained from a linear least squares fit. We have not implemented the simplex algorithm and compared with PWGP's results. Our guess is the differences are small for clean events in which adjacent wires do not fire simultaneously.

In a multi-track enviroment when several adjacent wires do fire simultaneously, the simplex technique will probably be superior. For a bunch of adjacent hits, using a single Gaussian whose mean is at the center of the bunch is a bad approximation if the distribution is very wide. Alternatively, setting up a narrow Gaussian for each wire in a bunch and using only one of them in the fit is a procedure that creates information where there is none and can only lead to spurious tracks. In the simplex technique, single wire hits and multiple-adjacent-wire hits are treated in exactly the same way. Each hit corresponds to 2 hyperplanes in 4-dimensional parameter space. A hyperplane constrains the trajectory iff it is a boundary of the feasible region. The reconstruction of a track will not be biased by the fact there are other tracks present.

In summary, we have outlined a linear fitting technique

that is applicable whenever the experimental results are uniformly distributed. The solution is computationally straightforward and can be easily implemented in a computer program.

[1] Experiment #154 by PHSC. The Proportional Hybrid Spectrometer Consortium is a collaboration of ~ 50 physicists from the following institutions.
Brown University
CERN
Fermilab
Illinois Institute of Technology
University of Illinois
Indiana University
Johns Hopkins University
Massachusetts Institute of Technology
Oak Ridge National Laboratory
Rutgers University
Stevens Institute of Technology
University of Tennessee
Yale University

[2] A.E.Snyder, thesis, The Reaction $\pi^- p \rightarrow \pi^- \pi^+ \pi^- p$ at 147 Gev/c, #COO-1195-349, University of Illinois, (1975).

[3] J.Lach and S.Pruss, Instrumentation of the hadron beams in the neutrino area, Fermilab report TM-298 (1971).

[4] P.F.Jacques et al., On-line display aids for the automated measuring of bubble chamber film at Fermilab energies, Rev. Sci. Instrum. 48 963 (1977).

[5] We used the Gaussian form for programming convenience. Actually, the probability is more like a sum of two step functions than a Gaussian, i.e. the probability density is uniform and non-zero inside a finite interval and zero everywhere else. For an alternative to using the Gaussian approximation, see Appendix 2.

[6] W.Bugg, PHS Consortium internal newsnote #30, August 1974.

[7] The minimum fit probability of 10^{-4} is small enough to include as fits some badly measured events but not too small to bring in garbage. In the final sample of neutrals, the effective minimum probability cut-off is actually higher because the really bad fits will not pass physicist inspection.

[8] Pull variables are defined as $(m-f)/((\Delta m)^2-(\Delta f)^2)^{1/2}$ where m is the measured value, f is the fitted value, Δm and Δf are the corresponding errors. Pull distributions should be Gaussians centered at zero with unit standard deviaton.

[9] The variables used by SQUAW are tan(d), k, and ϕ where the dip angle d is $\pi/2$ minus the polar angle, k=cos(d)/p, and ϕ is the azimuthal angle in a coordinate system with $\hat{z}$ along the camera axes.

[10] KTRACE program, W.Bugg and D.Petersen.

[11] T.M.Knasel, The Total Pair Production Cross-section in Hydrogen and Helium, DESY 70/2, 70/3 (1970).

[12] We used 1.030x1.392 μb/event for 2-prong events and 1.030x1.552 μb/event for greater-than-2-prong events. The factor 1.030, determined from beam count, accounts for the roll that was not used in this analysis but was used in
D.Fong et al., Cross Sections and Charged Particle Multiplicities for π^-p and K^-p Interactions at 147 Gev/c, Nuc.Phys. B102 386 (1976).

[13] Estimates of systematic errors are based on the following:

Contamination due to mis-classified ambiguous fits -- 10% for $\bar{\Lambda}$, $\frac{1}{2}$% for K^o_s.

If cross sections are calculated from the 10 roll sample alone without resorting to 2nd-scan-only weights and re-measurement weights, the results are $\sigma(K^o_s)$= 3.6719 ± 0.3305 mb, $\sigma(\Lambda)$= 1.7481 ± 0.2280 mb, $\sigma(\bar{\Lambda})$= 0.33721 ± 0.12460 mb, $\sigma(\gamma)$= 134.93 ± 8.46 mb. Comparing to Table 8, the non-uniform weighting schemes will contribute 5-6% uncertainty to the K^o_s, Λ, γ cross sections and 13% to the $\bar{\Lambda}$ cross section.

$\frac{1}{2}\sigma(\gamma)$ will over-estimate the π^o cross section by ~5% due to production of η^o, Σ^o, and other sources of γ's.

[14] The charged particle data come from the same batch of film but were previously analyzed. See Ref. [12].

[15] T.Ferbel and H.Taft, Inelastic Interactions of 11.4 Gev/c π^- Mesons in Hydrogen, Nuovo Cimento 28 1214 (1963).

[16] F.Barreiro et al., Inclusive neutral-strange-particle production in π^-p interactions at 15 Gev/c, Phys.Rev. D17 669 (1978).

[17] P.Bosetti et al., Inclusive Strange Particle Production in π^+p interactions at 16 Gev/c, Nuc.Phys. B94 21 (1975).

[18] J.Bartke et al., Hyperon and Kaon Production by 16 Gev/c Negative Pions on Protons, Nuovo Cimento 24 876 (1962).

[19] P.H.Stuntebeck et al., Inclusive production of K_1^o, Λ^o, and $\bar{\Lambda}^o$ in 18.5-Gev/c $\pi^{\pm}p$ interactions, Phys.Rev. D9 608 (1974).

J.T.Powers et al., Compilation of Data for $\pi^{\pm}p$ Inclusive Reactions at 8 and 18.5 Gev/c, Phys.Rev. D8 1947 (1973).

[20] O.Balea et al., Neutral Strange Particle Production in π^-p, π^-n, and π^-C Interactions at 40 Gev/c, Nuc.Phys. B79 57 (1974).

[21] H.Blumenfeld et al., Inclusive Neutral Kaon and Lambda Production in 69 Gev/c pp Interactions, Phys.Let. 45B 528 (1973).

H.Blumenfeld et al., Photon Production in 69 Gev/c pp Interactions, Phys.Let. 45B 525 (1973).

V.V.Ammosov et al., Average Charged Particle Multiplicity and Topological Cross Sections in 50 Gev/c and 69 Gev/c pp Interactions, Phys.Let. 42B 519 (1972).

[22] E.L.Berger et al., Production of K_S^o, Λ, and γ in 100 Gev/c π^-p Interactions, CERN/D.Ph.II/PHYS 74-27 (1974).

E.L.Berger et al., Multiplicity Cross Sections for 100 Gev/c π^-p Interactions, CERN/D.Ph.II/PHYS 74-9 (1974).

[23] J.W.Chapman et al., Production of γ, Λ^o, K_S^o, and $\bar{\Lambda}^o$ in pp Collisions at 102 Gev/c, Phys.Let. 47B 465 (1973).

C.Bromberg et al., Cross Sections and Charged-Particle Multiplicities at 102 and 405 Gev/c, Phys.Rev.Let. 31 1563 (1973).

[24] D.Ljung et al., π^-p interactions at 205 Gev/c: Multiplicities of charged and neutral particles; production of neutral particles, Phys.Rev. D15 3163 (1977).

[25] K.Jaeger et al., Characteristics of V^o and γ production in pp interactions at 205 Gev/c, Phys.Rev. D11 2405 (1975).

[26] D.Bogert et al., Inclusive production of neutral strange particles in 250 Gev/c $\pi^- p$ interactions, Phys.Rev. D16 2098 (1977).

J.Albright, private comm.

[27] A.Sheng et al., pp interactions at 300 Gev/c: γ and neutral-strange-particle production, Phys.Rev. D11 1733 (1975).

A.Firestone et al., pp interactions at 300 Gev/c: Measurement of the charged-particle multiplicity and the total and elastic cross sections, Phys.Rev. D10 2080 (1974).

[28] V.P.Kenney et al., Inclusive Production of π^o, K_s^o, Λ^o, and $\bar{\Lambda}^o$ in 360 Gev/c $\pi^- p$ Interactions, pre-print.

A.Firestone et al., $\pi^- p$ interactions at 360 Gev/c: Measurement of the total and elastic cross sections and the charged-particle multiplicity distribution, Phys.Rev. D14 2902 (1976).

[29] P.Stix and T.Ferbel, Charged-particle multiplicities in high-energy collisions, Phys.Rev. D15 358 (1977).

[30] $A = 0.859 \pm 0.011$
$B_2 = 0.0448 \pm 0.0028$
$X^2 = 47$ for 13 degrees of freedom.

[31] M.Antinucci et al., Mulcitplicities of Charged Particles up to ISR Energies, Nuovo Cimento Letters 6 121 (1973).

[32] Z.Koba, H.B.Nielsen, and P.Olesen, Scaling of Multiplicity Distributions in High Energy Hadron Collisions, Nuc.Phys. B40 317 (1972).

[33] F.T.Dao and J.Whitmore, Study of Neutral-Charged Particle Correlations in High Energy Collisions, Phys.Let. 46B 252 (1973).

[34] D.Cohen, Some Remarks Concerning K_s^o and Λ Production in High Energy Proton-Proton Collisions, Phys.Let. 47B 457 (1973).

[35] P.Slattery, Evidence for the Onset of Semi-inclusive Scaling in Proton-Proton Collisions in the 50-300 Gev/c Momentum Range, Phys.Rev.Let. 29 1624 (1972).

[36] Using $\frac{1}{2}\int dz\, z^q\, \Phi_2(z) = A\Gamma(\frac{q+3}{2}) / 4B^{q+3}$

$\frac{1}{2}\int dz\, z^q\, \Phi_3(z) = C\Gamma(\frac{q+3}{3}) / 6D^{q+3}$

and eq. 9, we get

$A=4B^3/\Gamma(\frac{3}{2})$, $B=\Gamma(\frac{3}{2})$

$C=6D^3$, $D=1/\Gamma(\frac{2}{3})$

[37] In several experiments, no value or error of the semi-inclusive neutral cross section was given for some high multiplicity channels presumably because no events was observed. These points have omitted from the fits. In addition, the 18-prong point in $\pi^- p$ 360 Gev/c has been omitted from the π^0 fit.

[38] Due to a different definition of inclusive two-particle cross sections, the $K_s^o K_s^o$ cross section quoted in ref. [26] (0.62±0.2 mb) should be multiplied by two before comparing with Table 11.

Vita

Tungching Ou

1965	graduated from Brent School, Baguio City, Philippines
1969	B.S. physics, MIT, Cambridge, Mass.
1971	started graduate work in physics, Rutgers University, New Brunswick, N.J.
1977	married to Annie Wang
1979	Ph.D. in physics